Constitutive Model of Aligned Carbon Nanotube/Nafion Nanocomposite Ionic Electroactive Polymer Actuators

by

Douglas S. Jacobs

B.S.E., Electrical Engineering
University of Michigan (2009)

Submitted to the Department of Mechanical Engineering
in partial fulfillment of the requirements for the degree of

Master of Science in Mechanical Engineering

at the

MASSACHUSETTS INSTITUTE OF TECHNOLOGY

February 2016

Author . . . .
Department of Mechanical Engineering
January 15, 2016

Certified by . . . .
Brian L. Wardle
Professor of Aeronautics and Astronautics
Thesis Supervisor

Certified by . . . .
Sang-Gook Kim
Professor of Mechanical Engineering
Thesis Reader

Accepted by . . . .
Rohan Abeyaratne
Quentin Berg Professor of Mechanics
Chairman, Department Graduate Committee

Constitutive Model of Aligned Carbon Nanotube/Nafion Nanocomposite Ionic Electroactive Polymer Actuators

by

Douglas S. Jacobs

Submitted to the Department of Mechanical Engineering
on January 15, 2016, in partial fulfillment of the
requirements for the degree of
Master of Science in Mechanical Engineering

Abstract

Research is progressing rapidly on composite nano-structured materials, including aligned carbon nanotube (A-CNT) polymer nanocomposites (PNC), and with device construction utilizing these novel materials. However, the material constitutive relations of the PNCs and tailoring of these is lagging. In this work, A-CNT and Nafion PNC electrodes are manufactured and investigated as the key active element in ionic-electroactive polymer (i-EAP) devices. i-EAP actuators are known to create relatively large strains with low input voltages, and could therefore be used for future high-strain actuation mechanisms such as synthetic muscles, microfluidic drug delivery, or low-frequency energy harvesting. Tailoring the PNC is accomplished by process control and moving to higher volume fraction (Vf) A-CNTs, in order to increase both the rate and magnitude of strain through increased non-isotropy and specific surface area for ionic transfer efficiency. This work shows methods to increase the A-CNT synthesis yield from below 50% to $\sim$90%, while keeping quality and morphology stable. Porous A-CNT based i-EAP electrodes are synthesized with CNT and Nafion volume fractions of 10-40% and 10-25%, respectively. Key elements of the non-isotropic mechanical, electrical and electroactive constitutive law are discussed and calculated for different morphologies of the electrodes. Tailored high Vf i-EAP devices at $\pm 3\ V$ show $\pm$4,130 *microstrain* in the transverse direction and an order of magnitude smaller strain ($\pm$420 *microstrain*) in the CNT axis direction, with A-CNT and Nafion Vfs of $\sim$20% and $\sim$15%, respectively. These large non-isotropic strains correspond to electroactive coupling coefficients of $7.1 \times 10^{-12}\ m/V$ in the transverse direction and $7.2 \times 10^{-13}\ m/V$ along the CNT axis. In addition, the i-EAP material's moduli are measured to be $\sim$85 *MPa* in the CNT axis direction and $\sim$50 *MPa* in the transverse direction, with a relative dielectric permittivity of 79, for this polymeric based i-EAP device. These coefficients constitute the first assembly of mechanical, electrical and electroactive properties into a constitutive relation for such an active nano-structured material. More extensive data sets for completing the full constitutive model and reducing measurement uncertainty are recommended for future work.

Thesis Supervisor: Brian L. Wardle
Title: Professor of Aeronautics and Astronautics

Acknowledgements

I would like to acknowledge the following people who have helped not only make this research a reality, but turned it into a successful work and a fun journey. First, I would like to thank my adviser Professor Brian Wardle, who has been patient with my odd circumstances while always providing insight and great advice in terms of how to tackle the many unforseen problems, and motivation for pushing the boundaries on CNT technologies. My first postdoctoral adviser at MIT, Dr. Noa Lachman, for working with me on how to successfully and effectively conduct research, as well as how to keep my tools and workspace clean. I would also like to thank Dr. Sunny Wicks for teaching me the finer details in creating PNCs, after I had many failures to cure bubble free PNC samples; Rich Li for assisting me with many processes in the lab and to collect the TGA data; Diana Lewis who has taught me a lot about the CVD process and A-CNT forest growth; Itai Stein for teaching me LaTeX which this thesis is written in; Dale Lidston for keeping the 1" furnace going when I am not around, reviewing this thesis, and for the biltong; Dr. Estelle Cohen for her expert TEM and SEM imaging used in this work; Mackenzie Devoe for her work on the Raman spectroscopy; Dr. Bharath Natarajan and the National Institute of Standards and Technology (NIST) team for attempting the first ever quantitative 3-D electron tomography of the Nafion PNC samples, as well as SEM and TEM imaging; the Pennsylvania State University Zhang Research Group including Dr. Mehdi Ghaffari and Professor Q. M. Zhang for sharing the processing and definition for the i-EAP manufacturing and collaborating; Luiz Acauan and Yue Zhou for their time spent reviewing this thesis; Amy Tatem-Bannister and Dr. Steven Kooi at the MIT Institute for Soldier Nanotechnologies (ISN) for the lab usage and hospitality, specifically for the use of the glove box, potentiostat and Zwick equipment; and the necstlab at MIT for providing a fun and challenging environment for completing advanced research. In addition, this work would not be possible without the Aero Astro and Mechanical Engineering departments at MIT, and the GE Aviation Edison and ACE programs who have supported this research. Last but most importantly, I would like to express my appreciation and love for my fiance Emily Altman, for providing moral support, love, and helping me to fix my many grammatical mistakes. Thank you to everyone on this list who has made this thesis possible!

Table of Contents

List of Figures

List of Tables

Abbreviations and Symbols

A-CNT	Aligned Carbon Nanotube
A-PNC	Aligned Polymer Nanocomposite
BMI-BF4	1-Butyl-3-Methylimidazolium Tetrafluoroborate
CNT	Carbon Nanotube
CV	Cyclic Voltammetry
CVD	Chemical Vapor Deposition
DIC	Digital Image Correlation
DMF	Dimethylformamide
DVB	Divinylbenzene
EAP	Electroactive Polymer
ECW	Electrochemical Window
FIB	Focused Ion Beam
i-EAP	ionic-Electroactive Polymer
iCVD	initiated Chemical Vapor Deposition
Ig/Id	Integrated Raman Intensities Ratio of G and D Peaks
IL	Ionic Liquid
IPMC	Ionic Polymer Metal Composite
MWCNT	Multi-walled Carbon Nanotubes
oCVD	oxidative Chemical Vapor Deposition
PC	Propylene Carbonate
PEM	Proton Exchange Membrane
PNC	Polymer Nanocomposites
PTFE	Polytetrafluoroethylene

RTIL	Room Temperature Ionic Liquid
SEM	Scanning Electron Microscopy
TEM	Transmission Electron Microscopy
TGA	Thermogravimetric Analysis
ToF-SIMS	Time-of-Flight Secondary Ion Mass Spectrometry
Vf	Volume Fraction
ΔV	Voltage Range, V
ε_o	Permittivity of Free Space, F/m
ε_r	Relative Dielectric Permittivity
ε_{ik}	Electric Displacement Tensor, F/m
$\frac{dV}{dt}$	Voltage Scan Rate, $V/second$
κ^{-1}	Debye Length, m
τ	Growth Time, $minutes$
A	Effective PNC Area, m^2
d_{ikl}	Electroactive Tensor, $m/V = C/N$
D_i	Electric Displacement, C/m^2
e	Elementary Charge, C
E_k	Electric Field, V/m
I_d	Discharge Current, A
I_M	Ionic Liquid Molarity, $mole/m^3$
k_B	Boltzmann's Constant, J/K
N_A	Avogadro's Number, M^{-1}
s_{ijkl}	Elastic Compliance Tensor, m^2/N
S_{ij}	Strain, m/m
T_K	Absolute Temperature, K
T_{kl}	Stress, N/m^2
x	Cartesian frame for the local PNC material axes along the CNT axis
y	Cartesian frame for the local PNC material axes normal to the CNT axis
z	Cartesian frame for the local PNC material axes normal to the CNT axis and y

Chapter 1

Introduction

Today's reliance on electrical automation is pushing the need for increased connections from the electrical to mechanical domains, utilizing transduction methods to complete tasks in a more powerful and efficient manner than ever previously imagined. Robotics, as well as biomimetic and prosthetic devices, require high energy density and low voltage sensors and actuators to effectively move and interact with the outside world[1–3]. In addition, scalability is key to forming devices such as synthetic muscles[4]. Similarly, energy harvesting materials are required for efficient distributed sensor concepts, which are envisioned everywhere from roads and bridges to jet engines.

Ionic electroactive polymer (i-EAP) materials have shown promise to deliver on this front, but have yet to be fully characterized and proven in a controllable and consistent manner. These materials are polymer based and include free ions or electrolyte solutions that, by transport such as migration and diffusion in response to an applied electric field, physically strain[2]. These devices are generally made up of two electrically isolated electrodes filled with an ionic, electrolytic solution[2]. The term "device" is used in the literature to usually describe an actuator or sensor configuration, but in this thesis the simplest i-EAP device is considered, which is comprised of the A-PNC soaked in an ionic liquid and connected to a counter electrode (usually another i-EAP "device").

The recent investigation into i-EAP materials is due to their relatively high strain capability, light weight, low voltage demands and damage tolerance[5]. Just a few volts of electricity have been shown to create large strains, showing the promise for safe, simple and efficient device materials. Earlier versions of i-EAPs have used neat polymers which are conductive to ions, sometimes including conductive metal nanoparticles to increase conduction efficiency. These early ionic polymer metal composites (IPMC) materials showed around 23-26 $microstrain$[6]. More recent studies have focused on alternate materials and tailored structural properties. For example, devices based on activated graphene oxide can generate strains as high as 560,000 $microstrain$ (56%) with energy densities of 1.5 J/cc using only 4 V of electricity[1]. These devices still have limitations, however, such as low efficiencies, slow response times, moisture sensitivity, electrolytic requirements and a lack of constitutive model based understanding of the device materials[3,7,8].

1.1 Aligned Carbon Nanotube Nafion Nanocomposite Ionic Electroactive Polymer Actuators

In order to advance the capabilities of i-EAP devices, research has focused on functionally integrating the polymeric devices with different conducting materials, such as metal electrodes or nanoparticles[2,6,9], graphene[1], and aligned carbon nanotubes (A-CNT)[3,10,11]. A-CNT materials have been utilized for their high conductivity, large surface areas, high non-isotropy, and low density, and have shown much promise to improving the energy density and speed of i-EAP devices[10,11].

Research in general is progressing rapidly on composite nano-structured materials, especially on aligned carbon nanotube (A-CNT) polymer nanocomposites (PNC), and device construction utilizing these novel materials[3,10,12–17]. These efforts are driven by the need to be able to tailor the multifunctional properties of materials to best optimize their weight and performance, for industries such as transportation and aerospace[17,18]. Leveraging these advances in morphological processing, many new types of PNCs have been demonstrated with nano-structured characteristics and interfaces. Of particular interest is the non-isotropic conductivity and stiffness, as well as the large surface areas of A-CNTs utilized in PNCs, which can lead to larger strains, capacitance, or customizable resistances for applications such as heaters, supercapacitors, or i-EAP actuators[19]. In addition, due to the multifunctional properties of A-CNT materials, these devices could one day provide a multitude of additional benefits such as heat shielding, structural support, and capacitive energy storage. For this thesis, the axes are defined based on the A-CNT orientation as shown in Figure 1.1.

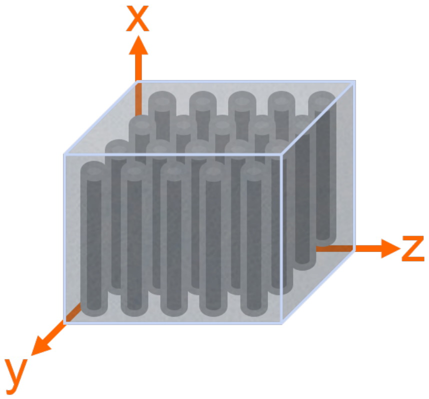

Figure 1.1: A-CNT and PNC local material axes, with x axis parallel to A-CNT aligned direction.

1.2 Thesis Outline

This thesis thoroughly discusses the background, processing, morphologies, characterization methods, and constitutive relations of the novel i-EAP actuator electrode materials based on nano-structured A-CNT and Nafion materials. Moving beyond prior isotropic investigations, the valued non-isotropy of the A-PNC materials will be considered, with multiple stages of device processing characterized. The second chapter discusses the need for these materials with proposed applications, prior EAP materials, and A-CNT composites, as well as research gaps and challenges of the current EAP materials. The third chapter provides the research goals and thesis objectives, and the approach for device manufacturing and characterization. Chapter 4 goes through the full device processing, from neat materials to final multi-material and nano-structured devices with dimensions that span many orders of magnitude. A large portion of this section is dedicated to the enhancement and control of processing, to maximize quality and repeatability. The 1 centimeter square A-CNT material synthesis, including growth and densification from 1% up to 40% volume fraction (Vf), has been improved to provide almost 100% yield from the prior lower yield synthesis (i.e. A-CNT growth and densification), and has been characterized for morphology, quality, and consistency. A-PNC and EAP creation is also discussed with Nafion and ionic liquid infusion, respectively. Chapter 5 delves into device operation through visual, mechanical, electrical and electroactive characterization, showing the structure, morphology, stiffness, capacitance, permittivity, and electroactive properties. The last chapter, 6, summarizes this work and discusses what conclusions can be drawn, as well as recommends future work in the areas of A-CNT and i-EAP actuator research.

Chapter 2

Background

The electroactive polymer (EAP) material's actuation and sensing capability is a phenomenon that has been studied in depth for over 20 years, due to its low density, mechanical flexibility, and high strain capability with low required voltages[5–7]. The materials have the additional benefit in that they are simple to process, however they still lack a fundamental understanding of their actuation mechanisms, limiting their design and usage[2,6,20]. The potential applications for this technology range from actuators and sensors to energy harvesting technology, and simple devices have already been manufactured. In parallel, A-CNT materials and PNCs are an active area of research, promising non-isotropic material properties with both high mechanical strength and electrical conductivity[16]. Given the benefits of A-CNTs in polymer nanocomposites and hierarchical nano-engineered composites, their introduction into EAP electrodes promises additional performance enhancement which has been demonstrated in initial work[10].

2.1 Electroactive Polymer Materials and Applications

Rapid progress has been made on EAP material and device designs in the past two decades, moving from only 23 $microstrain$[6] to over 500,000 $microstrain$[1], over a 4 order of magnitude increase. EAP materials were originally discovered in 1880 by Roentgen when investigating a rubber band subjected to an electric field[7]. Their large strain response with low applied voltages makes EAP devices similar to natural biological muscles[7,21]. This has created a wide field of biomimicry devices based on EAP materials, including potential for artificial muscles, prosthetics, implants and biological inspired robots[7,21]. Other potential EAP actuators include active clothing[7], control and positioning actuators for conformal structures[5], smart material systems, and microelectromechanical systems[22]. Demonstrated EAP products include micro-actuator catheters[23], audio speakers, focus control for cameras in cellular telephones, miniature manipulators and grippers, active diaphragms for pumps, dust wipers for space rovers, robotic fish and even blimp fins[7].

Many EAP materials can also be used as sensors or energy harvesting devices, generating voltage when strained. Initially, it was assumed an EAP device might not strain since there shouldn't be differential forcing of anions and cations, but testing has shown that a voltage is in fact produced across the device when bent[22]. It can be orders of magnitude less than the voltage required to create the same amount of strain in the material, since the method of generating the electric potential is due to a secondary effect of the geometrical displacement of internal ions creating effective dipoles[22].

Parker currently produces a full line of dielectric EAP sensors and actuators, using technology acquired from Artificial Muscles Incorporated in June of 2014 (example products shown in Figure 2.1). Another company, Environmental Robots Inc. produces i-EAP based sensors and actuators for research and instructional purposes, and has demonstrated jellyfish free swimming motion, morphing antennas, flapping wings and artificial muscle fibers[24].

EAP devices can be divided into two categories, field-activated EAPs and ionic EAPs, which both have their advantages and disadvantages[7]. Field-activated EAP materials are soft polymers that have high dielectric breakdown voltages, which actuate when under high voltages from induced deformation at a molecular scale[7]. The i-EAP devices have the benefit of only requiring a few volts for actuation due to ion displacement, but do require electrolyte solutions or solvents to allow for this ionic mobility[7]. Also, since they rely on the diffusion or drift of ions, they can be slower than other types of electroactive materials[2]. The maximum strain of these devices correlates to the device capacitance, which shows that the strain is caused by the ionic mobility[20]. This relationship has been shown to be between 10 to 15 $microstrain/C/m^2$, independent of material, across various

Figure 2.1: Parker's flexible electroactive polymer sensor and actuator products, derived from technology developed at Artificial Muscles, Inc.[25].

i-EAPs[20]. This also suggests that the deformation is due to the charge build up at the two electrode interfaces, and is the reason for increasing both the capacitance and electrode surface area of i-EAP devices in order to increase their maximum strain.

The i-EAP devices are generally made up of a polymer backbone, positive and negative electrodes, a solvent for hydrating the device, and mobile ions that can migrate through the solvent. Early devices used neat polymers, gold or platinum electrodes and water, and had issues with short lifetimes due to the solvent evaporation[20].

The i-EAP strain is accomplished by drift and diffusion of relatively large ions in the solvent towards the electrodes, causing those regions to swell from the excess ions. In larger devices (over 20 μm thick) the ion movement can be dominated by diffusion based on relative ion concentrations, not the drift due to voltages[26]. This also means that thicker devices with have much slower strain rates, as the diffusion time constant is proportional to the square of the ion transport distance. Liu et al. was able to measure ion concentrations in an i-EAP sample using the time-of-flight secondary ion mass spectrometry (ToF-SIMS) method, showing both electrodes strain with excess ions[26]. The cathode however has a higher concentration of excess ions than the anode, and this differential causes the device to strain[26]. This strain mechanism is shown in Figure 2.2. If allowed to diffuse after a voltage is no longer applied, depending on the ion sizes, the device strain can relax to a lower strain magnitude, and sometimes even moves beyond the initial dimensions to create a negative strain.

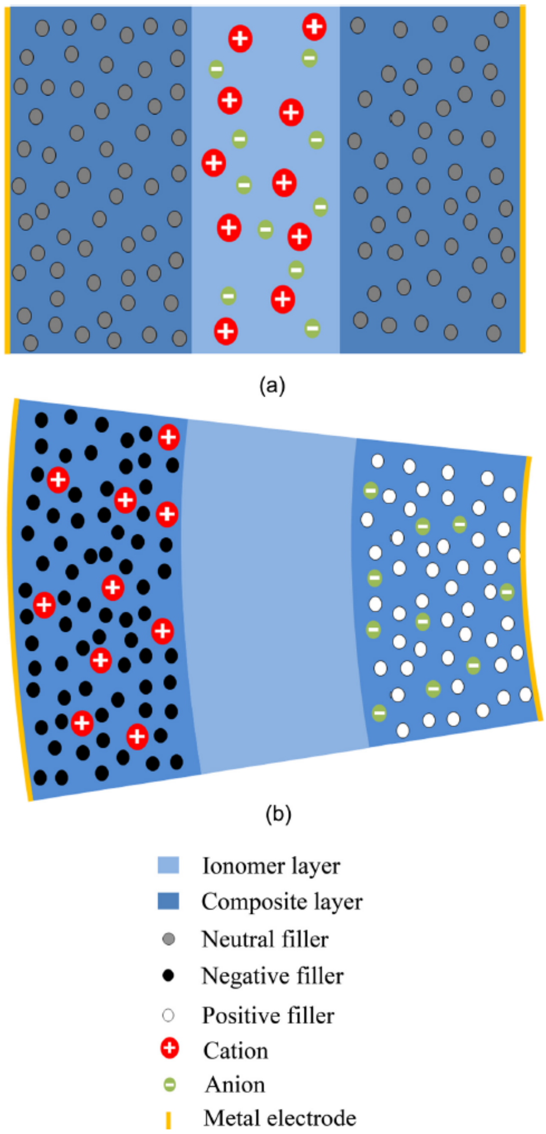

Figure 2.2: Electroactive polymer bending actuator, with (a) no voltage applied in the initial condition with no strain and (b) in a strained state with voltage applied. This shows the method of strain based on excess ion concentrations towards the positive cathode and negative anode electrodes, as well as towards the positively and negatively charged electronic fillers[27].

The strain achieved in specific i-EAP devices has steadily increased over the years. In 2001, Bar-Cohen et al. used gold-electroded Flemion with tetra-nbutylammonium ions in water to achieve only 23 *microstrain*[6]. Akle et al. in 2005 was able to generate strains as large as 24,380 *microstrain*, with consistent strain response for over 250,000 cycles by switching to ionic liquids (IL) and implanting ruthenium(IV) oxide (RuO_2) powder between the Nafion and the gold foil electrodes[5]. Even rechargeable lithium battery cells have been tested as i-EAP actuators due to their similarity in structure, and Chin et al. achieved 30,000 *microstrain* when unloaded[28]. Newer materials such as Poly[(vinylidene difluoride)-co-(chlorotrifluoroethylene)](P(VDFCTFE)) and P(VDFCTFE) / poly (methylmethacrylate) (PMMA) cross-linked blends have recently been tested, showing higher strains than Nafion with lower currents, and more efficient i-EAP materials[29]. Similarly, 265,000 *microstrain* can be generated using TFSI-doped polyprrole actuators[30].

2.2 Aligned Carbon Nanotube Composites

2.2.1 Carbon Nanotubes

Carbon nanotubes (CNT) are a recently discovered material, but are already being developed into real world applications. Even though the quality and process control of most CNTs are still improving, the commercial capacity is already estimated to be as large as 5,500 tons per year in 2011[31]. An individual CNT has a very high elastic modulus of 1 *TPa*, which ranks above steel and even silicon carbide[32].

Of interest to this research is one type of these known as aligned carbon nanotubes (A-CNT), with a specific collimated tube morphology that can be exploited to make highly non-isotropic structures and devices. The A-CNTs in this work are based on a standard rapid growth method developed in 2006 that creates 1 *mm* tall A-CNTs in about 15 minutes[33]. These grow on an electron beam deposited catalyst of 1/10 *nm* Fe/Al_2O_3 on (100) 150 *mm* silicon wafers (p-type, 1-10 Ohm/cm), and uses ethylene, hydrogen and argon at 750 $^\circ C$[33]. The growth consists of six stages: system evacuation, catalyst ripening, growth initiation, high yield growth, delamination and cooling down. These stages of A-CNT growth are shown in Figure 2.3. This A-CNT growth process has been determined to produce multi-walled carbon nanotubes (MWCNT) with outer diameters of around 8 *nm*, CNT to CNT spacing of 80 *nm*, and an average of 10^{10} CNT per cm^2 [34,35]. This works out to a volume fraction (Vf) of $\sim$1% of A-CNTs by volume[34]. In addition, there are on average between 3 to 7 walls, yielding a 5 *nm* inner diameter[33].

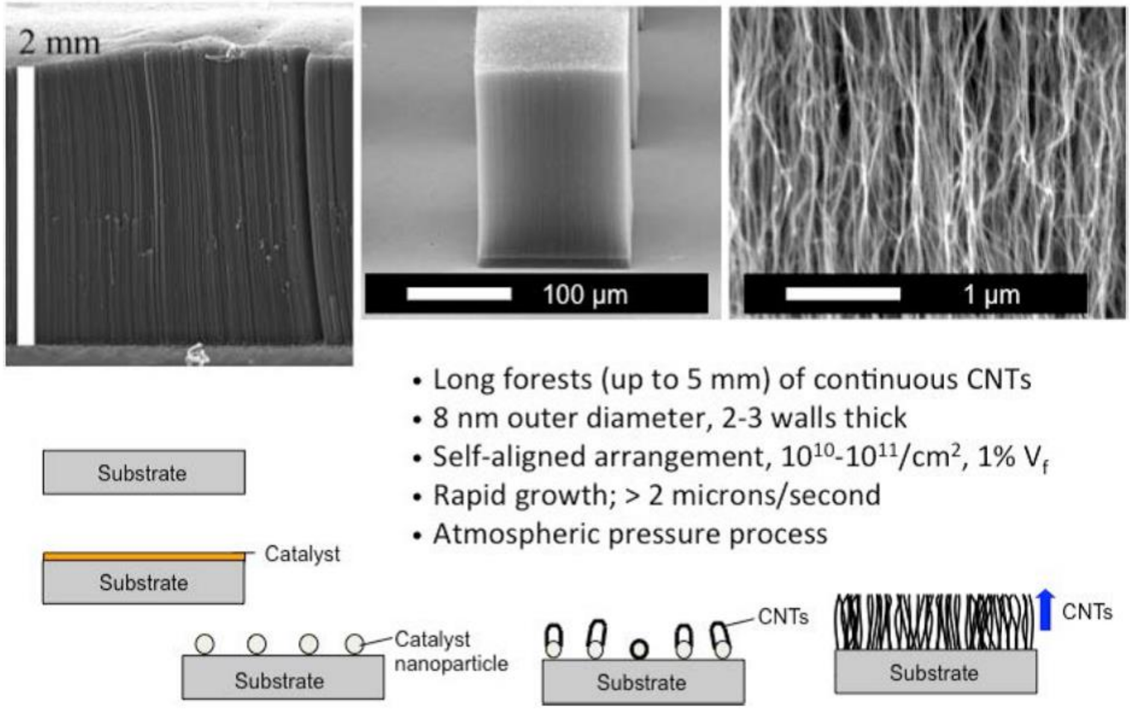

- Long forests (up to 5 mm) of continuous CNTs
- 8 nm outer diameter, 2-3 walls thick
- Self-aligned arrangement, 10^{10}-10^{11}/cm^2, 1% V_f
- Rapid growth; > 2 microns/second
- Atmospheric pressure process

Garcia, Hart, Wardle, Slocum, *AIAA SDM*, 2006. Hart & Slocum, *J. Phys Chem. B*, 2006.

Figure 2.3: A-CNT growth process, showing ripening, initiation and self aligned vertical growth stages[33]. Includes SEMs of growth morphology of up to 5 *mm* tall CNTs, 2-3 walls thick grown at atmospheric pressure.

Studies on this process have investigated gas flow rates and the flow field[33], thermal profiles[33,34,36], humidity or moisture levels[37,38], and working pressures[34]. Water is a key variable, as Hata et al. shows a small controlled amount of water during growth of single walled CNT can create easy to delaminate 2.5 *mm* tall dense forests[37]. The water acts as a weak oxidizer removing amorphous carbon from the catalyst and both increasing the activity and lifetimes. Nessim at al. has generated in situ water vapor by injecting oxygen into the CVD process, consistently growing over 5 *mm* tall A-CNT forests[38].

Multiple methods have been attempted to investigate the detailed multi-scale properties from single carbon nanotubes to *mm* size A-CNT samples at various Vfs, including transmission electron microscopy (TEM), scanning electron microscopy (SEM), Raman spectra and nano-indentation. Cebeci at al. has used the Oliver and Pharr nano-indentation method with a spherical indenter tip to characterize average micro scale A-CNT moduli of various

Vfs, showing 8.9 *MPa* (1% Vf), 71.5 *MPa* (10% Vf) and 816 *MPa* (20% Vf)[39]. Also, the CNT to CNT spacing is measured using SEMs of 78 *nm* (1% Vf), 18.5 *nm* (10% Vf) and 10.3 *nm* (20% Vf)[39]. This predicts a highly non-linear increase in modulus at higher Vf of up to 600 times, moving from the nominal 1% Vf to 20%[39]. Raman shift spectra can show the defect concentration, and thus quality, of the A-CNT samples. Samples from the original necstlab 1 inch furnace setup at MIT in building 37 have shown an integrated Raman intensities ratio of the G and D peaks (Ig/Id) of $\sim<1$[40], on 1 *mm* tall A-CNT forests similar to what is used in this work. In the temporary necstlab 2 inch furnace setup at MIT in building NW-14, similar Raman intensity ratios are measured as ~0.7, and shown to be similar across varying A-CNT heights up to 300 μm tall[41].

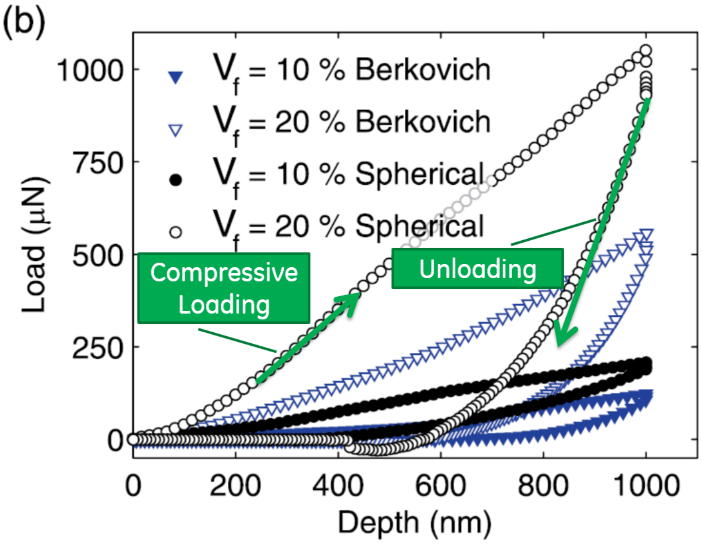

Figure 2.4: A-CNT nano-indentation curves showing loading and unloading curves of force and displacement, for both the spherical and Berkovich tips on 10% Vf and 20% Vf samples[39]. The modulus is calculated from the unloading curve, which is generally more consistent but also larger than the compressive loading modulus.

The Oliver and Pharr method utilizes the unloading curve of the compression test shown in Figure 2.4, unlike the linear loading curves used in larger scale compression testing. In Figure 2.4 the loading curve can be seen as a lower modulus than the unloading curve, which is a closer comparison to large scale compression tests. It has been theorized that this measurement might be influenced by the stored energy in inter-tube forces and waviness, as well as the generated strain. In addition, the measured samples have been prepared using a laser ablation method to create a flat surface for measurement, which on A-CNT materials could create a layer of amorphous carbon, which could then potentially stiffen the measured modulus. Bradford et al. shows that heat treating A-CNT foams does increase the modulus[42]. This shows that there could be a predicted difference versus full device scale compression testing completed in this work.

2.2.2 Aligned Carbon Nanotube Polymer Nanocomposites

The A-CNT material can be combined with epoxies and polymers to create similar structures to fiber-reinforced plastics such as carbon fiber composites, but at a much smaller scale. These aligned polymer nanocomposite (A-PNC) materials show the promise of highly non-isotropic material properties with both high mechanical strength and electrical conductivity[16]. Integrating A-CNTs into aerospace grade structural epoxies has created materials with an 8.8 *GPa* modulus for a 20% A-CNT Vf composite, as measured using nano-indentation[16]. Also, the A-CNT waviness has been measured based on 75 high-resolution SEM images as a wavelength ratio of 0.185 ±0.10. The conductivity of the A-PNC is also shown for a 1% Vf A-PNC to be 23 and 8.2 S/m for the axial and transverse directions, respectively[16].

A-CNT based PNC materials have been characterized in detail by both Sepulveda et al. and Handlin et al., to generate full three dimensional mechanical constitutive models[12,43]. A-CNT and PDMS materials have shown highly non-isotropic properties, with an assumed transverse isotropic stress strain relation. In the symmetry planes, a Young's modulus of 1.70 ±0.25 *MPa* was measured, with a Poisson ratio of 0.26 ±0.03, versus 8.1 ±1.2 *MPa*, 0.05 ±0.01, 0.24 ±0.04, and 0.24 ±0.07 *MPa* for the modulus, both Poisson ratios and shear modulus in the CNT direction, respectively[43]. The non-isotropic three dimensional constitutive tensor of Epoxy and A-CNT PNC materials of various Vfs was completed in 2013, with the derived constants shown in Figure 2.5. This testing used tensile specimens and digital image correlation (DIC) to measure the three dimensional parameters. There was a doubling of the modulus in the parallel direction to the CNT plane, x, when moving to 18% Vf, but not much change in modulus in the transverse (y) or shear direction[12].

Handlin's work uses the same reference axes as defined in Figure 1.1 as well as used in this work.

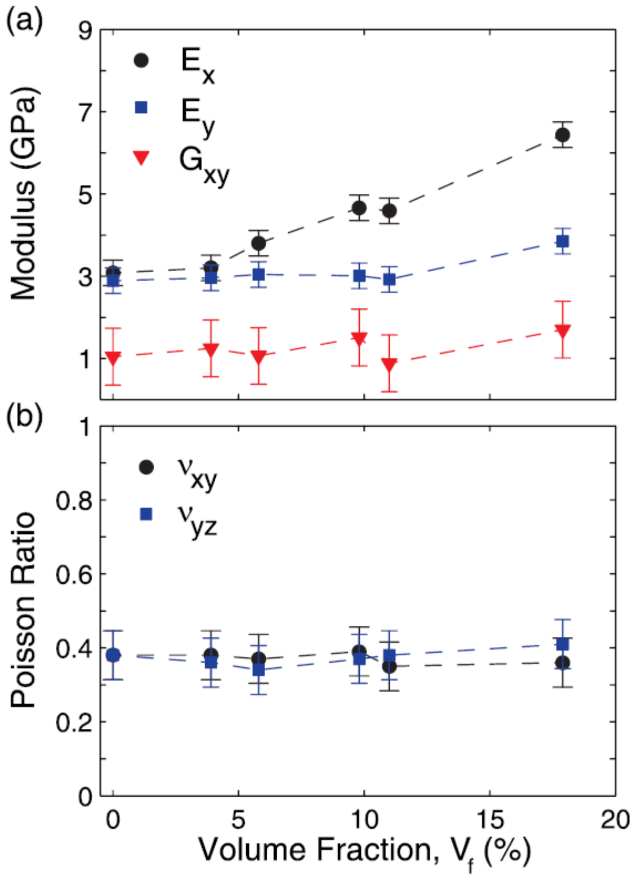

Figure 2.5: Plots of full non-isotropic constitutive model of A-CNT epoxy PNC samples across various A-CNT Vfs[12]. The transverse (y) modulus, shear modulus and Poisson ratios do not vary significantly with A-CNT Vf, but the modulus in the direction of the A-CNT varies linearly with Vf.

The tensile testing has shown a much lower modulus than predicted by the rule of mixtures, or as shown using nano-indentation, attributed to the waviness ratio of the CNTs[12]. The waviness does have a strong influence on the properties of the nano-composites, as well as the Vf of the A-CNTs has been shown to affect the waviness[39,44,45]. In particular, the effective elastic modulus can be reduced by as much as three orders of magnitude by accounting for waviness[45]. In addition, simulations have shown the polymer in the A-PNC can influence the waviness of the CNTs[45]. Other reasonings for the lower tensile modulus could be similar to the above discussions about the Oliver-Pharr method[16], as well as that the compressive modulus is shown to be higher in A-CNT PNCs than the tensile modulus, likely due to the higher load transfer in compression[46].

A fully detailed three dimensional characterization of morphology has also been completed on similar epoxy A-PNCs with various Vfs, using a focused ion beam (FIB) TEM method developed at the National Institute of Standards and Technology (NIST)[8]. Figure 2.6 shows the measured volume fraction and three dimensional alignment of four samples with varying amounts of mechanical densification and Vfs.

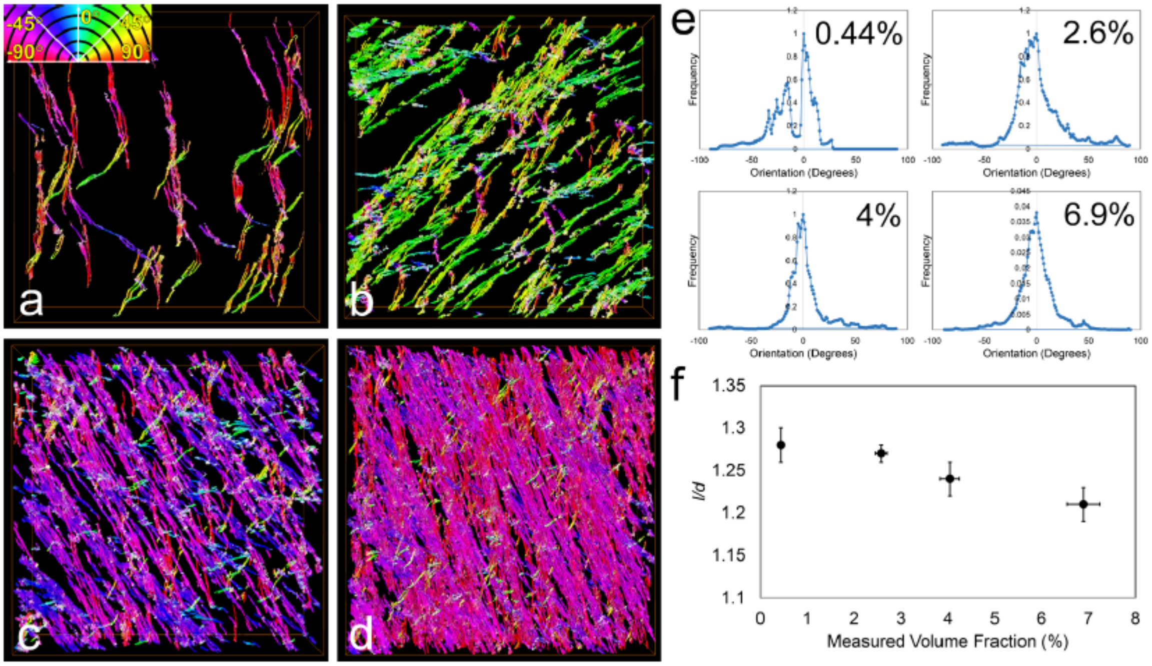

Figure 2.6: Four A-PNC samples characterized using 3D quantitative electron tomography from FIB-TEM imaging. Left series shows CNT direction by color for calculation of alignment, and the right series shows the measured Vf[8].

Additionally, coatings on A-CNTs have also been demonstrated, such as conformal coatings by oxidative chemical vapor deposition (oCVD) to create three phase A-PNCs[47]. Similarly to the structural A-PNC efforts, multi-phase device construction has been shown to create very high energy and power density supercapacitors using coated A-CNTs. Hybrid supercapacitors fabricated by Ghaffari et al. using PEDOT conformally coated A-CNTs densified to 5% Vf have shown a specific volumetric capacitance of 84.0 F/cm^3, compared to only 3.9 F/cm^3 for non-coated and undensified A-CNT samples, for specific energy and power densities of 11.8 Wh/L and 34.0 kW/L respectively[48]. Further optimizing these electrodes in an asymmetric manner has pushed the devices to specific energy and power densities of 82.8 Wh/L and 130.6 kW/L[19]. Other coatings such as manganese dioxide coated on CNT has generated a specific capacitance of 517 F/g at a scan rate of 5 $mV/second$ for an energy density of 3.88 Wh/kg at a power density of 7,000 W/kg[49].

The recent advances in A-CNT based PNCs and supercapacitors parallels with the i-EAP research, as higher specific capacitances generate larger strains, and faster capacitive charging equates to faster i-EAP actuation. These efforts will influence the planning and discussions of the A-CNT i-EAP materials in this work, as well as the known variables to the A-CNT growth will be investigated to allow specific tailoring of growth.

2.3 Nano-structured Ionic Electroactive Polymer Materials

Combining the recent advances in A-PNCs and supercapacitors with the i-EAP technology, nano-materials can be used to increase the strain and capacitance by having larger surface areas for constructing the i-EAP electrodes. The lower device capacitance than the supercapacitors shows the theoretical margin for advancement in i-EAP actuation of over 10 times[21]. Early attempts included placing randomly oriented CNTs into the electrodes of an i-EAP[50], or infusing nano-particles into the polymer layers. In 2010, Liu et al. infused RuO_2 nanoparticles into the bulk of the Nafion to make a more conductive nanocomposite, which when used with BMI-BF4 ionic liquid generated ~20,000 $microstrain$[10].

Recently, Liu et al. has incorporated A-CNTs into the i-EAP devices, not only increasing the capacitance and conductance but also providing a non-isotropic framework to preferentially strain in the desired direction[10]. This also allows for direct ion paths, increasing the actuation speed by removing the prior circuitous paths ions had to travel through[10]. These devices strained as high as 121,000 $microstrain$ perpendicular to the A-CNT axis, and 70,000 $microstrain$ in the thickness direction parallel to the A-CNT axis[10]. These devices were tested for over 300 cycles at 0.5 Hz, with no observed degradation. These high strains were achieved using A-CNT materials at higher volume fractions (Vf) of around

10%, which provides a larger specific electrode surface area for storing the excess ions[10].

This work has been continued by Michalenko et al. moving to higher Vf A-CNT based i-EAPs. In 2013, 40% Vf devices generated 132,000 *microstrain* in the perpendicular to A-CNT axis, using BMI-BF4 IL and a 3 V potential[11]. Figure 2.7 shows an overview of this i-EAP device architecture, and this is the basis for the devices that will be further discussed throughout this thesis.

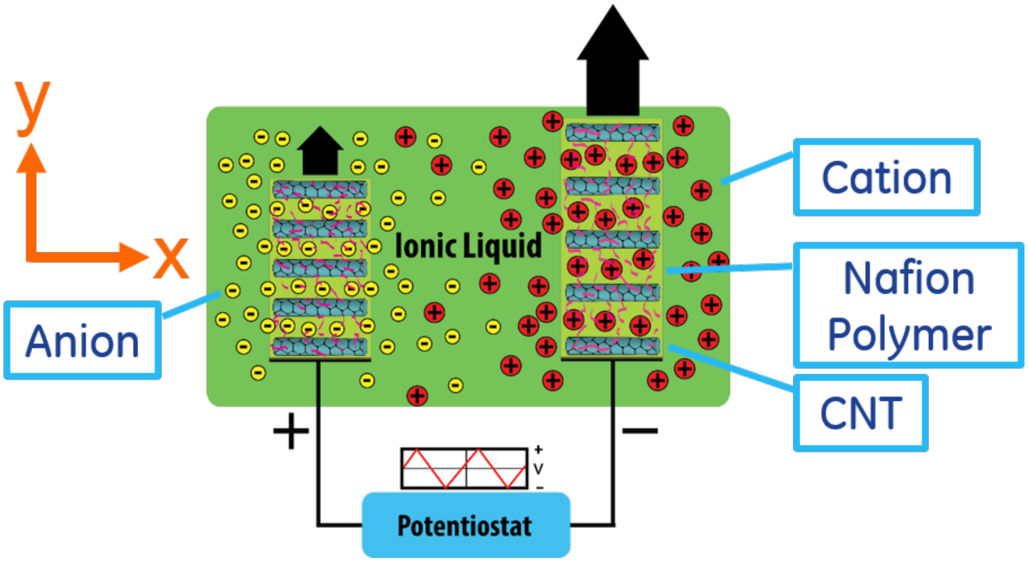

Figure 2.7: Thickness actuator setup, including positive and negative A-CNT and Nafion electrode based i-EAP devices in a pool of ionic liquid. Potentiostat setup provides actuation potential, and small yellow anions and large red cations are shown reacting to this voltage. The axes are defined such that the direction of the CNTs is the x direction with the y and z directions isotropic[11].

Graphene has also been used as a conductive additive to Nafion based i-EAP devices. Adding only 0.1% by weight of graphene to a Nafion based actuator has improved both the energy density and actuator displacement by over double[51]. Exfoliated graphite oxide based actuators have most recently been tested as one of the highest straining i-EAP materials. These graphitic i-EAP actuators have strained as much as 566,000 *microstrain* using BMI-BF4 and acetonitrile mixed solution under a 4 V potential and a 50 $mV/second$ scan rate[1]. The strains perpendicular to that direction were only 30,000 *microstrain* and in the negative direction, showing the high non-isotropy[1]. The devices were even tested up to 500 $mV/second$ rates. The IL has been mixed with the acetonitrile solvent in order to increase the ionic mobility by creating a lower viscosity. These devices also have a very high energy density of 1.5 J/cc using only 4 Volts of electricity, much higher energy density than alternate types of active materials[1]. Further optimization to these devices, such as adding ion transport channels, can increase the strain to as much as 775,000 $microstrain$[52].

This work carries on from these nano-structured i-EAP materials that have already been shown to generate very large strains, to generate a better understanding of the strain generating mechanism. Understanding the physics of the strain generation will assist in showing the real benefits and limitations of these materials. A-CNT based i-EAP materials are chosen as the basis of this thesis as they have already had much of the basic characterization completed, and their manufacturing is better understood than some of the most recently attempted materials.

2.4 Materials

This section focuses on the multitude of critical materials that are part of this work in creating A-PNC based i-EAP devices, including the Nafion polymer, ionic liquids, solvents and other associated equipment.

2.4.1 Nafion Polymer

Nafion is a sulfonated tetrafluoroethylene based fluoropolymer-copolymer created by DuPont in the 1960's, with the structural formula shown in Figure 2.8[53]. This is a popular selection for proton exchange membrane (PEM) fuel cells and i-EAP devices due to the thermally and mechanically stable teflon backbone, chemical resistance, and that it is highly conductive to cations. It is also a strong dielectric, and does not conduct anions or electrons.

Nafion is purchased from the Nafionstore in 0.3 x 1 m copolymer sheet form called NR211, by DuPont[53]. The elastic modulus of the Nafion film with 40 wt% ionic liquid was measured as 50 MPa[10], versus the specified modulus of 288 MPa[53] when dry. Since Nafion is insoluble and not possible to melt process, these films have to be carefully recast to take on new forms or coat structures, which is the method leveraged for this work[4].

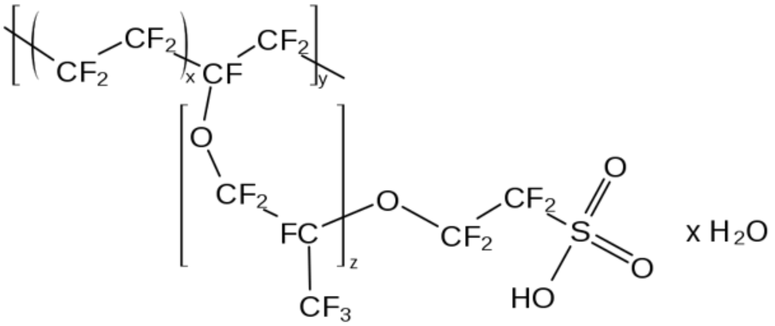

Figure 2.8: Structural formula for DuPont Nafion, showing teflon backbone and acidic sulfonic group side chains.

2.4.2 Ionic Liquids and Solvents

Ionic liquids (IL) have been used in recent i-EAP devices as the solvent for the polymer layer, both providing the ions for actuation and the method of transport. They have helped to improve both the stability of i-EAPs over time, as well as the electrochemical window (ECW). In addition, they are nonvolatile, nonflammable and have high ionic conductivity[54]. The toxicity of these ILs is not known, but is estimated to be low[55]. Sheng Liu studied multiple ILs for the impact to actuator speed and efficiency, based on the variations in ion sizes of four different imidazolium ionic liquids[54]. ILs have been used for organic synthesis, catalysis, electrochemical devices and solvent extraction of a variety of compounds[56]. Akle et al. has demonstrated highly stable i-EAP actuators based on these room temperature ionic liquid (RTIL)[20]. A RTIL is a salt that contains only ionic molecules that are liquid at room temperature, usually below 100 $^{\circ}C$, has a negligible vapor pressure and is stable up to 400 $^{\circ}C$[20]. The available i-EAP actuation voltage using IL is also larger than when using water, increasing the maximum energy density and actuation capacity[20]. There is vast supplemental information on ILs in the IL focus review by Barrosse-Antle et al.[57]. Some example ionic liquid cation and anion sizes are shown in Figure 5.1.

In this work, 1-Butyl-3-methylimidazolium tetrafluoroborate (BMI-BF4) is utilized as the IL, in a two molar mixture in propylene carbonate (PC). The BMI-BF4 is purchased in 99% high purity form from Iolitech (item number 174501-65-6, 100 *gm*). High purity PC purchased from VWR (item number AAA15552-0B, 99%, 1 *kg*), is an organic compound

Table 5.1: Ion dimensions in popular ionic liquids[27]. In this work, the BMI cation and BF4 anion are chosen since they have both very large and very small volumes respectively. This generates maximum strain with reduced strain relaxation after applied voltages are removed.

Ion	Molecular dimension (Å)	Molecular Volume (Å^3)
EMI$^+$	7.8 x 5.8 x 3.3	149
BMI$^+$	9.7 x 7.0 x 3.3	224
BF$_4^-$	3.1 x 3.1 x 3.1	30
Tf$^-$	4.4 x 4.4 x 3.3	64

and has the properties of being a polar, apriotic solvent. BMI-BF4 is chosen for these i-EAP devices as it has been shown to provide large strains compared to other ILs, with more limited strain relaxation[26]. The large strain device capability is due to the large electrochemical window of near 4 V and the large cation and anion size difference, which Ghaffari et al. used to create i-EAP devices with a max strain of 566,000 $microstrain$ (56.6%) at a 50 $mV/second$ scan rate[1]. The viscosities and densities of these IL solvent mixtures are shown to be linear functions of the fraction of the ionic liquid in the mixtures and the separate species properties[58]. Diluting the IL into the less viscous solvent allows for a faster actuator response. The relative dielectric permittivity of BMI-BF4 has also been measured at room temperature (25 $^\circ C$) as 13.9 ± 0.4, showing its non-conductance to electrons[59]. The relative dielectric permittivity of PC is also known to be 64.4 at 25 $^\circ C$, being even a stronger dielectric[60]. The disadvantage of using this IL, due to the large cation size, is that i-EAPs using BMI-BF4 have showed slower response times even with a diluted IL in solvent[27]. The atomic structure of BMI-BF4 is shown in Figure 2.9. Another limitation to these ILs is that they are very sensitive to moisture, as it can reduce the ECW[61]. Many studies of i-EAPs have focused on water content, as it can play a major role in device performance[62]. In addition, impurities in the IL can cause additional reactions at larger potentials, and generate dark residue that can limit DIC imaging and the operation of the i-EAP devices. Figure 2.10 shows the impact to BMI-BF4 of various moisture levels.

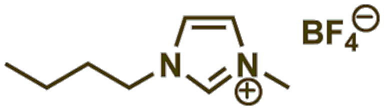

Figure 2.9: Structural formula of BMI-BF4 ionic liquid.

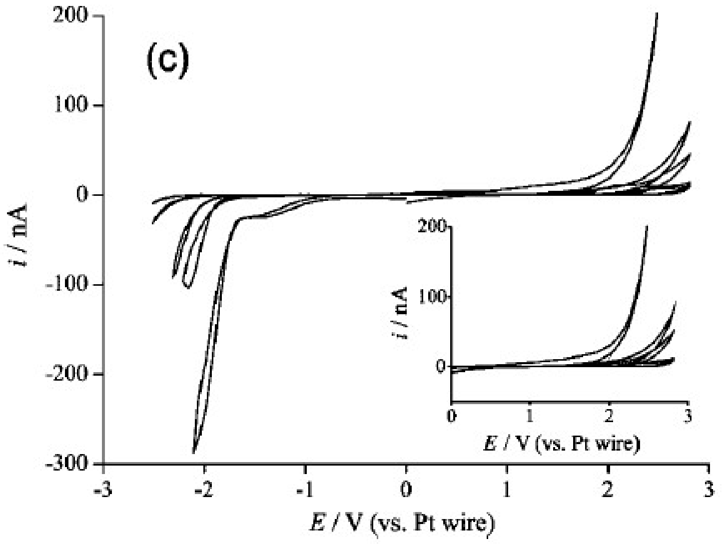

Figure 2.10: BMI-BF4 cyclic voltammogram across moisture levels showing impact to ECW[61]. Largest ECW is vacuum dried, followed by atmospheric, and then wet at 298 °*K*, 318 °*K* and 338 °*K*.

2.4.3 Dimethylformamide

The chemical used for infusing the Nafion into the A-CNT matrix is chosen to be dimethylformamide (DMF). It is used due to its boiling point of 153 °*C*, high enough to slowly evaporate over a long period of time[63]. The DMF is purchased from VWR in 99.9% minimum purity anhydrous form with no more than 50 *ppm* water content (item number BJAS076-1, 1 *L*).

2.5 Electroactive Polymer Challenges and Literature Gaps

EAP devices have been vastly improved since their invention, but much is still unknown about the actuation mechanisms and device properties. The core method of actuation has been speculated based on the characteristics of the devices, but the actual mechanism that causes strain is still largely unknown[2,6,20].

In order to effectively use these materials for actuator, sensor or energy harvesting devices, properties must be well understood. A properties database with scaling laws is needed to allow for accurately determining the response at various operation conditions[2], and this understanding of engineering foundations is needed to mature the technology[7]. Figure 2.11 shows the recommended properties of interest and the reason for knowing each for EAP devices, including mechanical, electrical, electroactive, environmental and microstructure analysis.

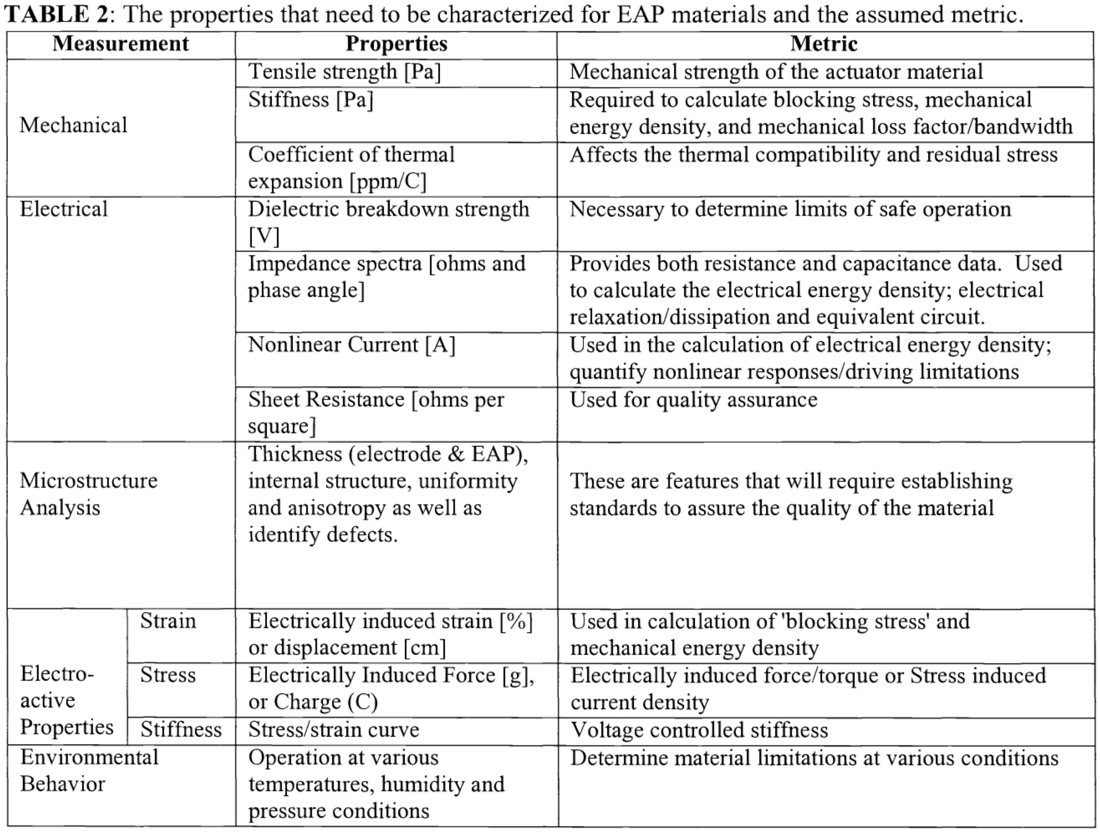

TABLE 2: The properties that need to be characterized for EAP materials and the assumed metric.

Measurement		**Properties**	**Metric**
Mechanical		Tensile strength [Pa]	Mechanical strength of the actuator material
		Stiffness [Pa]	Required to calculate blocking stress, mechanical energy density, and mechanical loss factor/bandwidth
		Coefficient of thermal expansion [ppm/C]	Affects the thermal compatibility and residual stress
Electrical		Dielectric breakdown strength [V]	Necessary to determine limits of safe operation
		Impedance spectra [ohms and phase angle]	Provides both resistance and capacitance data. Used to calculate the electrical energy density; electrical relaxation/dissipation and equivalent circuit.
		Nonlinear Current [A]	Used in the calculation of electrical energy density; quantify nonlinear responses/driving limitations
		Sheet Resistance [ohms per square]	Used for quality assurance
Microstructure Analysis		Thickness (electrode & EAP), internal structure, uniformity and anisotropy as well as identify defects.	These are features that will require establishing standards to assure the quality of the material
Electro-active Properties	Strain	Electrically induced strain [%] or displacement [cm]	Used in calculation of 'blocking stress' and mechanical energy density
	Stress	Electrically Induced Force [g], or Charge (C)	Electrically induced force/torque or Stress induced current density
	Stiffness	Stress/strain curve	Voltage controlled stiffness
Environmental Behavior		Operation at various temperatures, humidity and pressure conditions	Determine material limitations at various conditions

Figure 2.11: Suggested characterization properties of significance for EAP materials from Bar-Cohen et al. 2001[6]. Some of these have been investigated, but many assume full isotropy or remain unknown.

In addition to the multitude of required characterizations to complete, there are many complicating factors of i-EAP devices making this a greater challenge. Since these devices have such large strains, there are generally mismatches with the metal electrodes, nonlinear properties, and hysteresis. Also, difficult processing has created nonhomogeneity issues in the devices, making accurate characterization nearly impossible. Many studies treat the i-

EAP devices as isotropic due to these complications, which is not accurate for these highly non-isotropic materials. Liu et al. has assumed full isotropy for calculating the material modulus[10], which has been shown as an incorrect assumption based on the strain of these devices being very different in the different axes.

Advances on the i-EAP materials themselves are also ongoing, to meet the demanding requirements of small, lightweight, low power and high strain devices needed for artificial muscles and similar actuators. Early devices using water as solvents had short lifetimes and required constant hydration, where as newer devices with ILs require a dry environment free from impurities. The usage of IL met the demands forecast by Bar-Cohen et al. in 2008, looking for new materials that can be operated in dry environments but not requiring any protective coating layers, by working with solvents of low vapor pressure to increase both the response rate and lifetimes[7]. This research continues on this path of both creating tailored i-EAP devices with higher processing consistency, as well as further characterizing many of the parameters from Figure 2.11.

Chapter 3

Objectives and Approach

Ionic-Electroactive Polymer devices and materials have been widely studied for their high strain capabilities, but key morphological, mechanical and processing qualities remain unknown. The A-CNT based i-EAP materials have never had a defined constitutive relation, and even a method of connecting the mechanical to electroactive relationships are not discussed, where as they are well known in piezoelectric devices. In order to utilize these devices, further insight into the detailed processing requirements and constitutive relations are required.

In this work, A-CNT and Nafion PNC electrodes, the key active portion in ionic-electroactive polymer (i-EAP) actuators, are manufactured and investigated. i-EAP actuators create large strains with low input voltages, and could therefore be used for future high strain sensing and actuation mechanisms such as synthetic muscles, microfluidic drug delivery, or low frequency energy harvesting. Experimental data is acquired and reduced to form structure-property relations for these materials, with some process-structure investigation, the latter focused on quality and repeatability. Stiffness measurements, strain under applied electric field, and morphological information (via SEM, TEM, optical microscopy, and other techniques) is captured.

A-CNT based i-EAP devices are a current focus based on their recently shown and useful non-isotropic strains, high speed actuation, and potential for commercialization. Nafion is selected due to its stability and high ionic conductivity, along with flexible side chains that allow for ionic mobility. The A-PNC improvement is accomplished by process control and moving to higher volume fraction A-CNTs in the PNCs, in order to increase both the rate of strain and the magnitude of strain consistently through increased non-isotropy and ionic transfer efficiency. These process variabilities seen in prior work result from a lack of tight control over the thermal profile, environmental variations and user process variations, which will all be discussed in this work. For high yield device processing, the current low yield CNT growth will not suffice, so a new process is required. The goal of this new A-CNT growth process will be to keep similar dimensional and morphological properties, without degrading the quality, and while dramatically increasing the processing yield. Lastly, the non-isotropic linear mechanical, electrical and electroactive constitutive law is discussed and measured for different morphologies of the electrode devices, and compared to prior work.

Chapter 4

Experimental

4.1 Aligned Carbon Nanotube Synthesis

The novel portion of ionic electroactive polymer (i-EAP) actuators being studied herein is the electrode material, an aligned carbon nanotube (A-CNT) polymer nanocomposite (PNC) device. The PNC device is manufactured in three main subsections, the A-CNT (with or without densification), the Nafion infusion for creating the A-PNC, and the ionic liquid infusion to create the active i-EAP electrode. Each stage has associated design considerations which have been studied, and will be discussed in the following sections.

4.1.1 Chemical Vapor Deposition Processing

The first process is to grow the A-CNT using a modified chemical vapor deposition (CVD) recipe of hydrogen, helium, ethylene[33] and water. This CVD process to grow the A-CNT forests is run at atmospheric pressure, and normally yields multiple 1 *cm* square samples of self aligned 1,000 micrometer tall A-CNTs. This is a rapid growth process that regularly yields around 2.4 micrometers of height per second, using the same stages of growth as defined in Chapter 2. Water is added in this work as a process control for stabilizing humidity during growth independent of the ambient humidity around the furnace. This also assists with delamination[38], and increases forest heights[37], as discussed later in this section. In addition, the thermal ramp during catalyst ripening is now controlled to limit thermal overshoot and catalyst ripening differences, for a uniform and consistent distribution of A-CNT "forest" height, and high quality A-CNT forests. The A-CNTs have been characterized with Raman spectroscopy, to show their structural quality, as well as with TEM and SEM for wall thickness and diameters, which will be detailed in Section 5.1.

The 1" furnace used for tall CVD growth in the necstlab at MIT uses a Thermo Scientific Lindberg/Blue M 1200 $^{\circ}C$ split-hinge tube furnace for the main growth section, with the entire CVD system contained inside a fume hood for safety and to provide consistent ambient flow conditions. This setup is shown in Figure 4.1. The growth occurs inside a 1" diameter seasoned quartz tube sitting inside the furnace. The seasoning process for a new clean quartz tube requires multiple growths with inconsistent results, but once completed will yield years of consistent growths. In addition to the main furnace, there is a Thermo Scientific Lindberg Blue M Mini Mite 1,100 $^{\circ}C$ tube furnace used for preheating the gas to assist with growth. This furnace was setup in MIT's building NW-14 for the majority of this work, and then moved to a new lab in building 35 for the final few growths. The gases utilized during CVD are helium (99.999% Airgas HE UHP300), hydrogen (99.999% Airgas HY UHP300) and ethylene (99.5% Airgas EY CP200). The water content is controlled by bubbling various amounts of a separately controlled helium gas flow through deionized water at a relatively controlled ambient temperature. Lastly, the furnace setup is now stabilized from user to user variation by creating location marks for the furnaces and tube during growth, as well as by using ceramic insulating caps on the ends of the main furnace around the quartz tube.

The growth process starts by preparing a 150 millimeter standard silicon wafer with the iron catalyst, requiring an RCA clean, thermal oxidation, and electron beam deposition of the iron. The goal is to achieve a 1 *nm* thick iron layer, as well as a 10 *nm* alumina layer on top of the silicon substrate[33]. The wafers are then cleaved into one centimeter square substrates, which are "cleaned" with clear tape twice. The second tape cleaning is very critical to generating low defect A-CNT forests, to clean any areas that were unable to be cleaned during the first cleaning due to presence of silicon fragments on top. The cleaning method involves pressing the tape onto the surface of the wafer chips until the entire area is adhered to the tape, and then removing the tape along with any dirt and debris from the

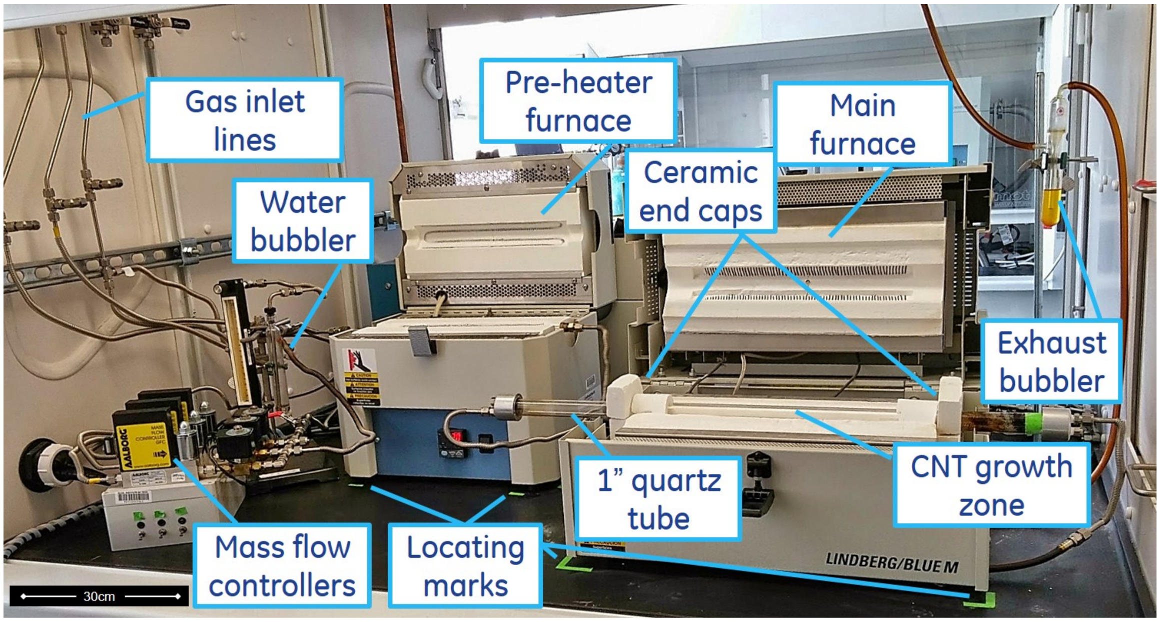

Figure 4.1: CVD furnace with 1" diameter tube for growing tall A-CNT forests, located in fume hood on MIT building 35. Includes helium, hydrogen and ethylene inlet lines, mass flow controllers, 1" quartz tube, water bubbler, exhaust bubbler, pre-heater furnace, main furnace, and locating marks for placement consistency.

wafer. The silicon wafer chips are then transferred, still on the second piece of cleaning tape, to the furnace for growth. This makes sure no additional debris is reintroduced to the wafer chips while in transport. Four samples are loaded directly into the quartz tube without a wafer boat, and are located at positions -2, 0, 2, and 4 *cm* from the center of the tube. The 4 *cm* location is optional, and is generally ~50-80 μm shorter. The wafers loaded inside the quartz tube are shown in Figure 4.2.

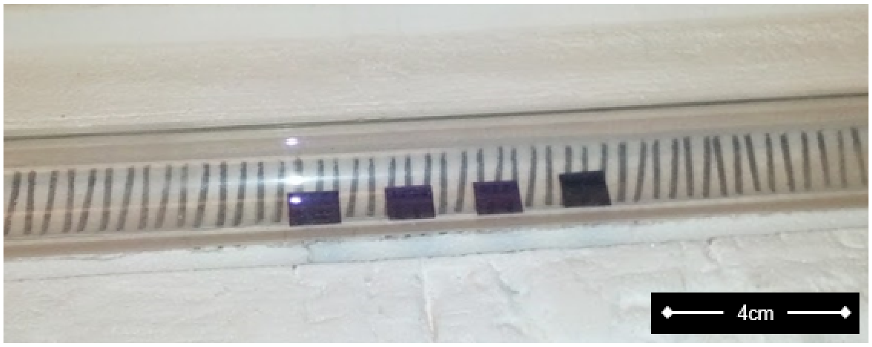

Figure 4.2: Quartz tube loaded with four 1 *cm* growth wafer chips at -2, 0, 2 and 4 *cm* positions.

The growth process consists of six stages: system evacuation, catalyst ripening, growth initiation, high yield growth, delamination and cooling down, similar to the growth described in Chapter 2. The first stage is evacuating the ambient atmosphere from the system, in order to supply the CVD furnace with gasses such as hydrogen and ethylene safely. All of the gasses are flowed for 20 seconds, followed by a full 4 minute flush of the system with the inert gas, helium. In order for the iron catalyst to be prepared for growing CNTs, a ripening stage is required. The furnace is controllably ramped up in a consistent manner over about 20 minutes to the growth temperature set point of 740 $^{\circ}C$ on the furnace with 200 *sccm* of hydrogen and 37 *sccm* of helium, and then left to sit for 5 minutes at the growth temperature. This ripening stage allows the iron to evenly disperse into nanoparticles on the surface and provides a consistent growth and forest morphology. The hydrogen is chosen as the gas during this phase to increase the reactivity in the catalyst[33]. In this research, a 200 $^{\circ}C$ hold was added to the process during the thermal ramp, in order to reduce thermal overshoot and thus growth variations. In addition, 0.5 *sccm* of helium bubbled through $\sim$21 $^{\circ}C$ DI water ($\sim$0.7 bubbles per second) is flowed once the furnace's main zone reaches 600 $^{\circ}C$, to assist with delamination and to control humidity for consistent forest heights.

The growth stage then begins when 150 *sccm* of ethylene is introduced in addition to the helium and hydrogen. After a seven and a half minute growth, the ethylene and water are turned off and the hydrogen is changed to 250 *sccm* for 2 minutes for the delamination process. The hydrogen is left on during the delamination phase as it etches the polyclclic hydrocarbons off the metal catalyst surfaces, which allows for an easier separation of the A-CNT from the substrate[33]. After the delamination, the rapid cooling phase begins by opening both of the heaters' lids under only 1,000 *sccm* of helium. Once the furnace reaches 180 $^{\circ}C$, the process is considered completed, and the samples and quartz tube are now cool enough for removal. At the end of the day, or after three growths, a process known as baking the tube is completed to make sure the quartz tube is free from debris and carbon deposits. This process is simply heating the quartz tube in the furnace under atmospheric conditions to allow the debris accumulated from growth to oxidize off the tube wall.

The CVD growth process results in, on average, four samples of 1 centimeter by 1 centimeter by 1,050 micrometer A-CNT forests loosely attached to the silicon substrates. The A-CNTs produced in this process have been studied in detail previously as described in

Chapter 2, but are confirmed in this thesis for continuity and consistency. The modifications in this process are discussed in the next section in more detail, and the growth results are shown in Section 5.1. The final fully detailed growth recipe is shown in Appendix A.

4.1.2 Delamination

The A-CNT forests are then delaminated from the silicon wafer substrate after optical height characterization using a microscope with a 20x objective. The sample is held using tweezers on an anti-static mat, and while also wearing an anti-static wrist strap. A sharp razor blade is used to gently separate the A-CNT forest from the substrate. If the delamination process has been successful, the forest will immediately and dynamically release from the silicon substrate, and can be lifted away. The anti-static mat and wrist straps are used in order to release any static buildup on the forest or tweezers, and allows for an easier separation from the razor blade and other metallic tools.

4.1.3 Biaxial Densification

These forests can then be biaxially densified mechanically to volume fractions up to 40%, resulting in stable forests ready for A-PNC creation. This process can be completed manually or using an automated motor control system. For this work, a fixture for manual densification is employed. Said fixture keeps all tooling in proper alignment, and reduces variation while increasing yield on the process. The fixture, seen in Figure 4.3 as part of the densification setup, uses two metallic pushers in orthogonal directions, to squeeze the A-CNT forest without buckling the forest in any direction. This process is sensitive to the height of the forest, thus growth height control is essential. By changing the size of the second pusher and the distance the pushers squeeze, variable densification can be achieved in ranges from 5% to 40% Vf.

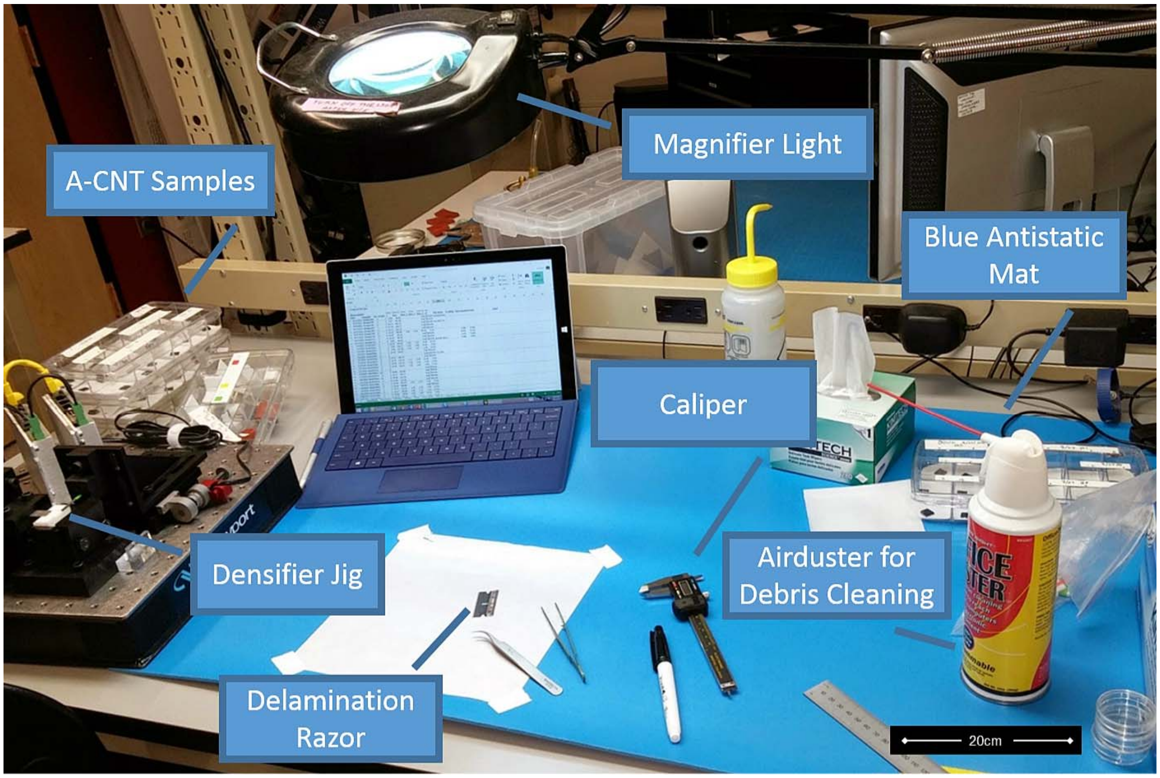

Figure 4.3: CNT densification station, including densifier jig fixture, tools and anti-static mat. The anti-static mat and wrist strap remove the issue of the A-CNT samples statically clinging to the metallic tools.

4.2 Growth Enhancements for High Yield 1 mm Tall Aligned Carbon Nanotube Samples

In order to manufacture high quality A-PNC devices in a high yield manner, creating consistent and reproducible A-CNT samples is paramount. The primary parameters are the height of the forest and the ease of delamination of the forest from the wafer, while the secondary metrics are the amount of amorphous carbon found on the surfaces of the A-CNTs and the quality. CNT tube quality, namely defect content, can effect the final devices by modifying the surface areas and ionic channel sizes of the final devices. This work started with a semi-consistent growth recipe that could create between 500 μm and 1,500 μm forests, but was not able to delaminate without using high forces with a razor, which changes the alignment of the CNTs and damage the forests. In addition, these more difficult delaminations generally lose sections of the CNTs during the process.

The parameters known to affect the growth are the gas flow rates and flow field[33], thermal profiles[33,34,36], humidity or moisture levels[37,38], CNT quality, and working pressures[34]. Initially, humidity was only controlled by deciding to grow forests on rainy or snowy days, as well as with the process known as baking the tube. Baking the tube has the side effect of also removing residual moisture from the tube, and can be used to affect the growth conditions. The gas flow rates have been previously optimized to maintain the maximum growth rate and quality of the CNTs, so that is not a variable investigated in this thesis. In addition, the ethylene source is estimated to be much larger than the growth requires, to provide a uniform gaseous carbon source at the growth location. Assuming a 1% conversion of the ethylene gas flow, 5 walled CNTs and a 1% Vf, for this growth at 2.4 $\mu m/second$ the growth would be converting only 38.4 *sccm* of ethylene on average[33] out of the 150 *sccm* available. The remaining process control variables focused on will be moisture content and thermal profiles.

4.2.1 Catalyst Ripening and Furnace Overshoot

In the first stage of the growth process discussed in section 4.1.1, catalyst ripening, the thermally-driven profile is critical to create the correct growth initiation conditions of the catalyst[36]. The standard CVD process sets the furnace temperature to 740 $^{\circ}C$, and once the thermocouple reads 740 $^{\circ}C$, it continues onto the next stage in the process. The controller sets the heaters based on a thermocouple inside the furnace, which is located above the quartz tube in plane with the heating elements. Due to the simplistic PID control system built in to the furnace, and the reality that the furnace thermocouple does not measure the inner tube temperature where growth occurs, the temperature control is not perfect. Figure 4.4 shows both the thermal ramp rate of the furnace's thermocouple readout outside the tube, compared to a temporary thermocouple placed in the center inside the tube, used to estimate the actual growth conditions. Not only is the temperature inside the tube higher than the set point, there is also considerable overshoot. Since the PID control is not well tuned or adaptive, this overshoot is expected to vary based on initial starting temperature.

In addition, the furnace thermal ramp rate and length of time varies based on the start-

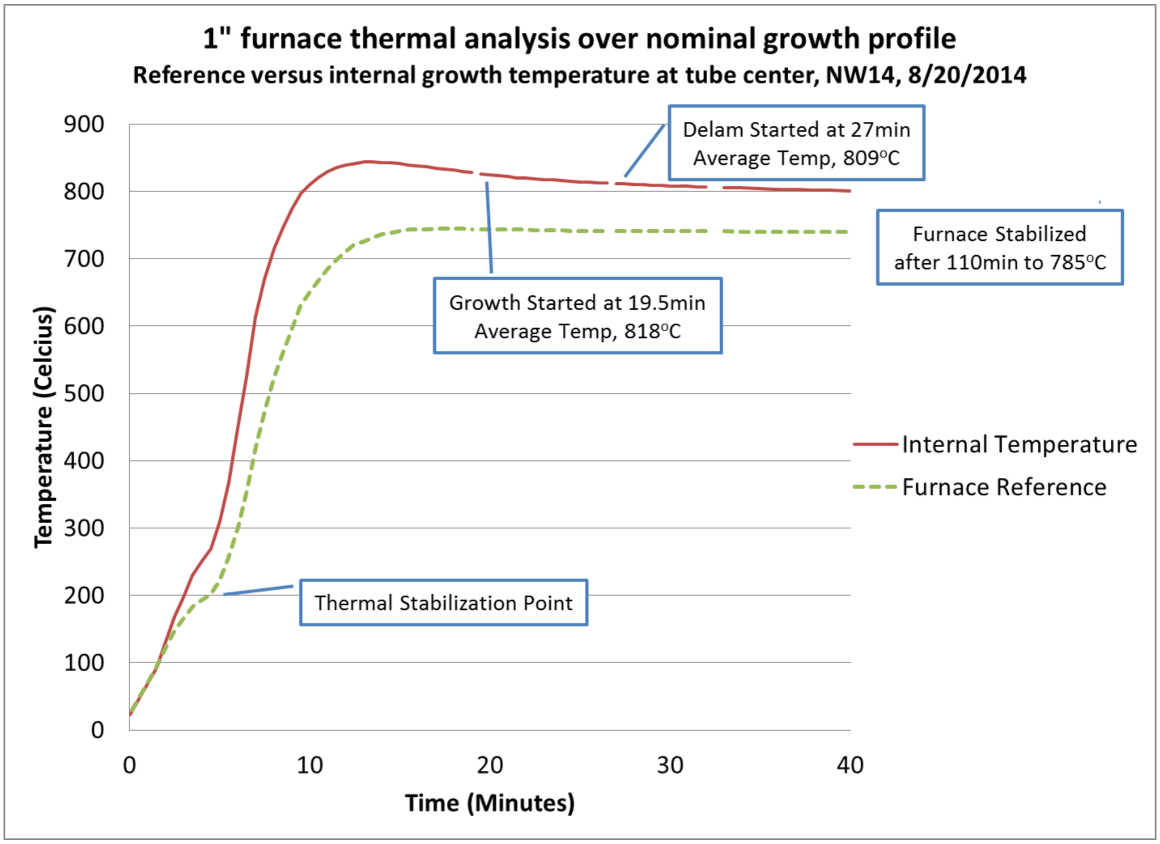

Figure 4.4: Temperature variation from the actual growth zone inside the quartz tube to the reference furnace thermocouple over a standard growth thermal profile. There is a large internal temperature overshoot, as well as the temperature takes a very long time to fully stabilize. The actual growth temperature is near 800 °C versus the set point of 740 °C.

ing temperature, seen in Figure 4.5. The original process can vary by around 3 minutes when comparing back to back growths. In order to limit the variation in both the thermal overshoot and the length of ripening time, a thermal stabilization point is added at 200 °C, below any active phase of the catalyst. The dotted lines in Figure 4.5 show the resulting thermal ramp profiles with this included stabilization time, with the ramp time variation reduced to only 30 seconds, and following a more consistent profile. This is also expected to limit the PID controller variation in overshoot, further reducing variation in the growth environment.

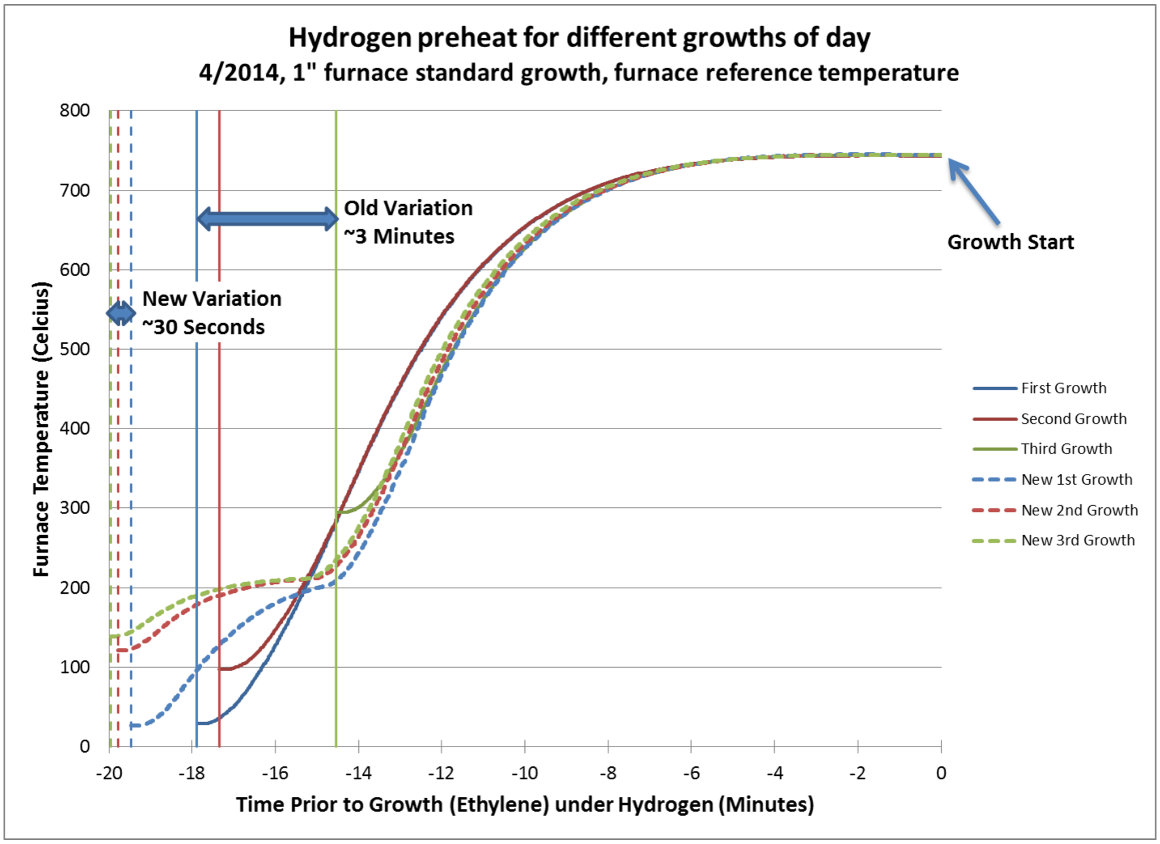

Figure 4.5: Furnace thermal ramp rate variation of old and new growth control methods, showing reduced variation in catalyst pretreatment for consecutive growths.

4.2.2 Humidity and Water Usage

Oxygen and moisture have become a focus of many recent studies on A-CNT growth[37,38]. This suggests the level of ambient humidity at the beginning of growth could impact the growth height and A-CNT forest characteristics. In addition, it has been shown that the catalyst lifetimes can be dramatically increased using moisture to remove amorphous carbon deposits on the catalyst surface, increasing the potential CNT growth heights[37]. Various amounts of moisture, added through bubbling helium through a bubbler filled with deionized water, were added to the same standard growth conditions. It was immediately evident the forest heights increased, but there were questions on quality. In order to quantify any negative impact, Raman spectroscopy is used to investigate the differences between the nominal “dry” growth, and the updated “wet” growths with added moisture. This Raman is completed using a HORIBA Jobin Yvon’s LabRAM 800HR micro Raman system, with a wavelength of 532 *nm*, 13 *mW* of power, and a 50x objective for a spot size of around 10 μm and 1.75 *mW* at the sample[40,41]. Each sample is imaged from above (beam is parallel to CNT alignment direction, x, and images the top of the forest which includes the entangled crust) at five locations (the center and corners) for two accumulations of 30 seconds, and the area ratio of the integrated G and D peak intensities provides an accurate measure of CNT defect concentration and quality[41].

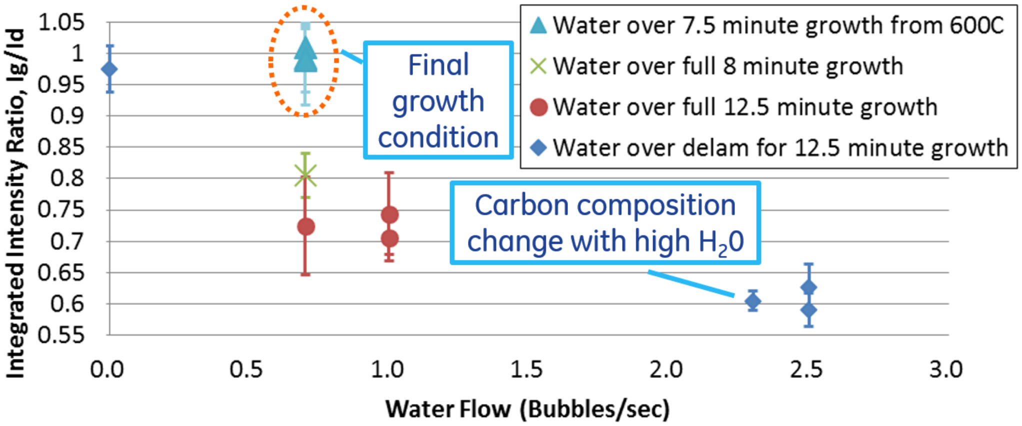

Figure 4.6: Effects of moisture on CNT growth quality, showing the ~500 *ppm* (0.7 b/s) H2O used in the final growth recipe creates a similar CNT quality to the prior dry growth methods, as measured by Raman spectroscopy. Also, this shows that high water content, even for short durations, can negatively impact the growth quality and carbon composition.

There is a very strong trend in reduced Ig/Id ratio with increased water content. The optimal moisture level of ~500 *ppm* (0.7 bubbles per second flow) was determined based on balancing A-CNT quality, height and reduced ambient moisture impact. The parts per million water content is calculated assuming a 2.6% saturation of water into the helium gas flow, and the total flow rate into the furnace of ethylene, hydrogen, and helium of 387 *sccm*. The addition of water was chosen since it effectively reduces variation and produces A-CNT samples with very flat surfaces (of a consistent height across the wafer chip sample) yet doesn't impact the Raman quality. It is estimated this is just enough water to negate the ambient humidity impact to the growth. In addition, the timing of the water is varied to further reduce the impact to A-CNT quality and forest flatness, with the final Raman measurements within experimental error of a growth without additional water. This is likely due to the reduction in growth time, as well as the controllable water content. This final process includes turning the water on during the furnace ramp once 600 °*C* is reached, and turning it off at the start of the delamination period. When the same flow of water is introduced during the entire growth, the forest suffers in quality and flatness. In addition, this water addition assisted with the delamination process, further reducing the connection of the A-CNT from the substrate and allowing for shortened hydrogen delamination times from upwards of five minutes to only two minutes.

4.2.3 Forest Height Control

After the addition of water content and the stabilized thermal ramp length of the CVD process, the A-CNT grew taller than with the originally designed process. The simplest variable to control forest height is the length of the growth stage. Figure 4.7 shows the growth heights versus growth stage time, showing a mostly linear process, that is not seen to stagnate in these growth times. From the original growth time of 12.5 minutes, it was determined using 7.5 minutes would grow to the correct height to achieve consistent 1 *mm* tall forests. The resulting forest height versus growth time in minutes, τ, for these determined conditions is shown in Equation 4.1. Using this equation, 7.5 minutes yields 1,081 μm on average, which allows for about two standard deviations of height above the 1 *mm* goal in large sample sizes.

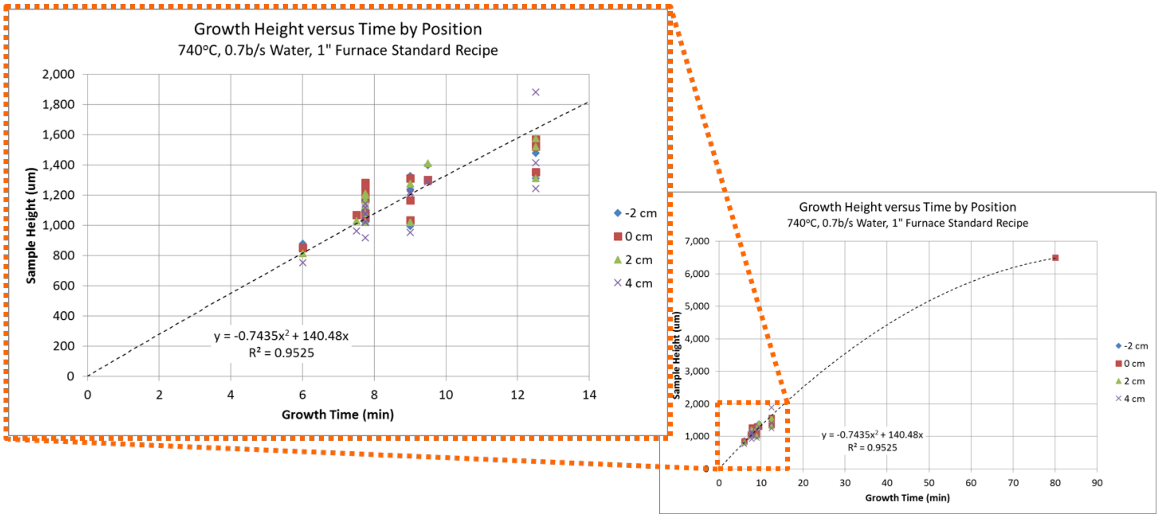

Figure 4.7: Height control of CNT forest, showing almost linear dependency and no stagnation up to over 6 *mm* heights.

$$\text{Height}_{CNT}(\tau) = -5.1854 * \tau^2 + 183.05 * \tau \tag{4.1}$$

4.2.4 Wafer Positioning

One more level of control of both forest height and quality is the position of the wafer chips in the furnace. If the wafers are placed too close to each other, they can reduce gas concentrations on downstream wafers, and thus additional height variation and usually less flatness. This can be seen as sometimes causing concave top surfaces, and sometimes convex, depending on the conditions. In addition, the temperature profile varies across the furnace due to leakage at the ends of the tube. This thermal variation as measured from the center line of the furnace using a standard thermocouple is shown in Figure 4.8. These measurements are completed without any gas flowing, the forward end cap removed, and with the ceramic end caps installed.

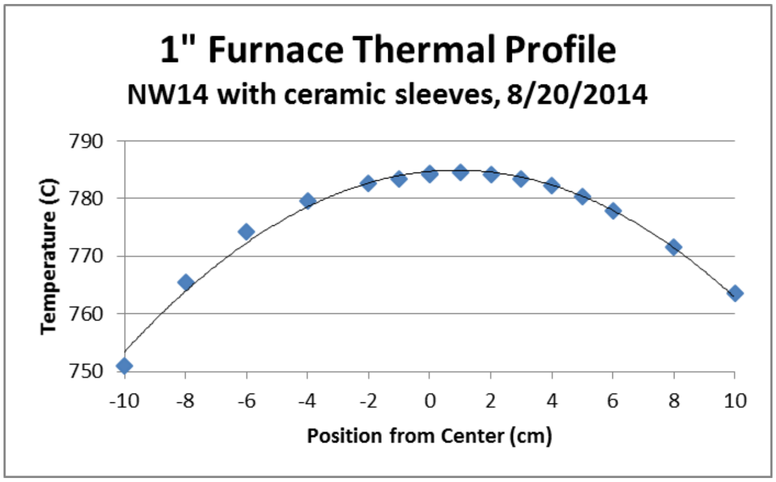

Figure 4.8: Thermal profile of 1” furnace with ceramic insulator caps installed, no gas flow, and forward end cap removed, using internal tube thermocouple. This shows a parabolic variation in temperature versus axial position from the center of the furnace.

4.2.5 Summary of Growth Conditions

The tailoring and process control completed on the A-CNT CVD growth provides an estimate of ideal growth conditions for the CNTs. These conditions inside the furnace’s quartz tube at the location of the samples are estimated from the various sources of data in this section. During the seven and a half minute growth, the furnace's gas flow consists of 150 *sccm* of ethylene, 200 *sccm* of hydrogen, 37 *sccm* of helium, and 0.5 *sccm* helium bubbled through DI water ($\sim$500 *ppm* water content). The pressure is near atmospheric with only a small pressure drop created through the exhaust bubbler and tubing, and the internal temperature averages around 800 $^{\circ}C$ during the growth phase. The growth consistency is increased due to consistent tube locations, furnace positions, and the ceramic end caps to retain more consistent heat across the length of the furnace. Also, the wafer positions are kept at -2, 0, 2 and 4 *cm* from the furnace mid point, which has been found to provide both consistency in forest height and a high yield of forests inside the desired heights. Together, wafer position, thermal profiles, water content and growth time are seen to be key process control parameters for tailoring growth. Varying these, as well as adding consistency to the process controls, yields a new stabilized wet growth easier to tailor, and much more independent to all environmental variations.

4.3 Polymer Nanocomposite Fabrication

The second stage of manufacturing an i-EAP device is infusing the Nafion into the A-CNT network, creating a A-PNC. The Nafion infusion uses a wet process, requiring pure solutions made up of NR211 Nafion polymer and DMF. The DMF solvent is utilized for creating the solution to infuse the A-CNTs due to its relatively high boiling point (153 $^{\circ}C$[63]). This high boiling point makes it possible to slowly evaporate the solvent when processed near room temperature[10], which is critical in order to not cause capillary densification of the A-CNTs. This collapse of the CNTs can also create polymer rich regions, and uneven actuation of the devices[10]. A low moisture requirement for the DMF exists due to the hydrophilic nature of Nafion's ion channels, in order to not trap moisture that can later be absorbed by the hygroscopic ionic liquids.

4.3.1 Nafion Solution Preparation

The NR211 25 micrometer thick Nafion sheets are cut into small pieces, and immersed in DMF under 80 $^{\circ}C$ of heat and stirred for 24 hours to create a 0.35% by mass Nafion in DMF solution. This solution is then diluted as needed to the required concentrations for infusion, and then sonicated for 5 minutes at room temperature in a VWR model 150D ultrasonic cleaner to remove bubbles and create an even mixture. The concentration used in most of this work was 0.055% by mass Nafion in DMF, to be able to just fully immerse the A-CNT in the solution with the correct amount of Nafion for the infusion inside a 20 *mL* vial. In that size vial, around 2,000 *mg* of solution is generally required to immerse a 1 *mm* tall forest, so the concentration required was chosen as 0.055% by mass Nafion in DMF. This is based on an average A-CNT weighing 2.3 *mg*, which requires 1.15 *mg* of Nafion ((40% + 10%) of 2.3 *mg*) in 2,090 *mg*, for a 0.55% by mass solution. The additional 10% by weight of Nafion is to account for the Nafion that coats the cage or vial instead of the A-CNT.

4.3.2 Nafion Infusion

In order to keep the sample from expanding during the Nafion infusion (i.e. keeping the same volume fraction of the as grown A-CNT forest), the A-CNT sample needs to be held rigidly on all sides during the infusion process.

To do this in a controlled environment while still allowing the Nafion solution to permeate the A-CNTs, a cage is created by gluing aluminum mesh to both sides of a metal plate with a hole for the A-CNT, shown in Figure 4.9. The cutout is sized to the correct dimensions for various volume fractions, plus margin to allow for placing the A-CNT inside. This process keeps the A-CNT PNC from expanding outside the desired volume. The glue selected is a silver two part conducting adhesive purchased from Alpha Aesar, in order to resist dissolving or loosing adhesion when left in the DMF solvent for over a week.

First, the cage has the aluminum mesh glued to the bottom using a large drop of the silver epoxy at each corner, and is left to dry overnight with pressure applied using a small cylinder of steel, or a weight. Next, the densified A-CNT samples are placed into the cages,

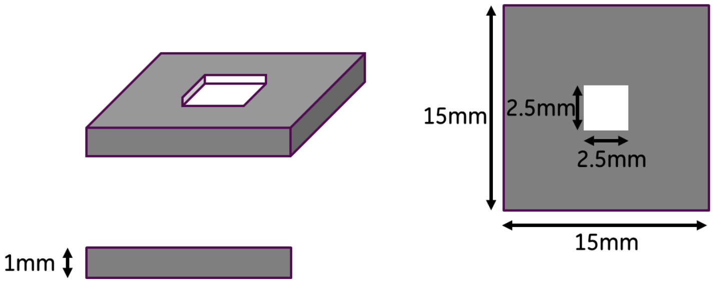

Figure 4.9: Aluminum A-PNC infusion cage drawing, sized for 20% Vf and to fit inside 20 *mL* vials.

and the top aluminum mesh layer is glued at the corners in a similar fashion as the bottom. Figure 4.10 shows this prior to the second aluminum mesh being placed on the glue. This is left to dry in a vacuum oven overnight, under -0.2 *bar* gauge pressure and 25 °*C* with airflow, by leaving the vacuum oven's inlet port open. This reduces the moisture content allowed to adhere to the A-CNT prior to the Nafion infusion.

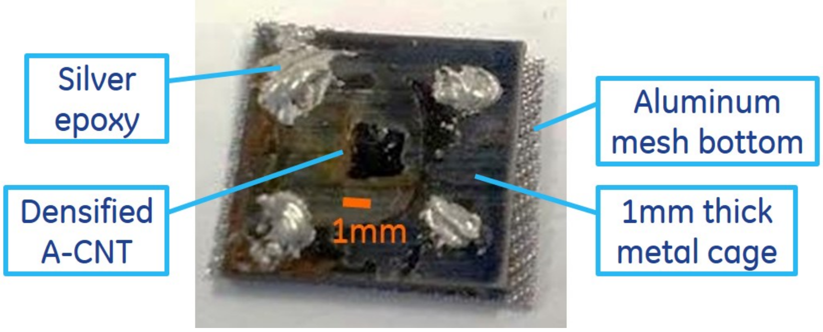

Figure 4.10: A-PNC infusion cage with A-CNT and silver epoxy, ready for second mesh layer.

The now fully caged A-CNT is placed inside a 20 *mL* vial with a corresponding amount of Nafion DMF solution to provide 40% the weight of the A-CNT of Nafion, plus the additional 10% discussed earlier to account for the cage coverage. Leaving porous regions inside the A-PNC will assist with actuation, by allowing easier diffusion of the ionic liquid, and also creating a lower stiffness of the composite material. This is also found to be near the limit of a single infusion, as shown in Figure 4.16. The scale used for accurately measuring the mass of the A-CNTs, the mass of Nafion to determine the correct DMF solution concentrations, and for measuring the dispensed solution for infusion is shown in Figure 4.11.

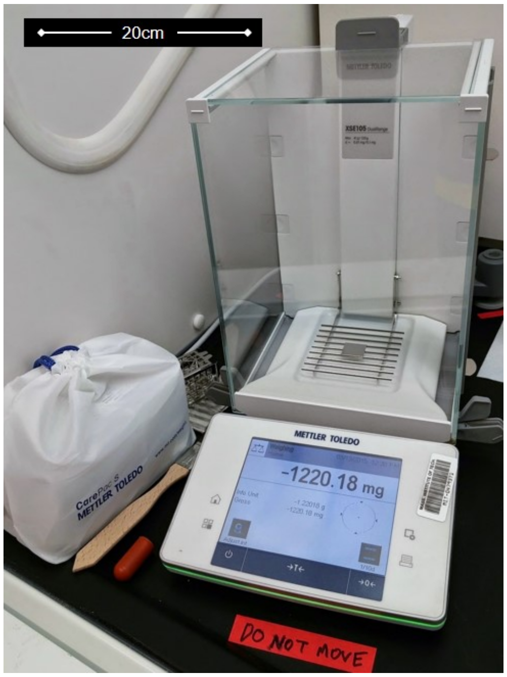

Figure 4.11: High accuracy Mettler Toledo scale used for A-CNT and Nafion mass measurements, accurate to ∼0.02 *mg*.

The DMF solution and caged CNTs are placed under a high vacuum at 45 °*C* for at least an hour to remove any trapped air bubbles (The oven used is shown in Figure 4.12). This process allows for a more homogenous infusion without trapping air inside, and thus higher quality actuators[1,10]. The DMF viscosity is low enough to fully infiltrate the CNT forest, with a viscosity of 0.47 *cP* at 80 °*C*[64]. Previous work has shown successful infusion and full CNT wetting using liquids with viscosities in the range of 833 *cP* in 1% volume fraction A-CNT forests with heights exceeding 1 *mm*[17], showing margin to the current process. Even 1.5 *mm* CNTs have shown to be fully wetted using SU-8 photopolymer at 8 *cP*[65]. The vacuum infusion pressure chosen is 50 *millibar*, in order to not boil off the DMF near its vapor pressure of 17 *millibar* at this temperature[63]. The DMF is then allowed to evaporate in slight vacuum (-0.2 *bar* gauge) and 45 °*C* for around 7 days[10]. This controlled evaporation keeps the A-CNT from collapsing and causing Nafion rich regions[10], similar to the capillary densification mechanism. This is done as a batch process usually including 16 samples arranged in the oven, and tracked by sample ID numbers, shown in Figure 4.13.

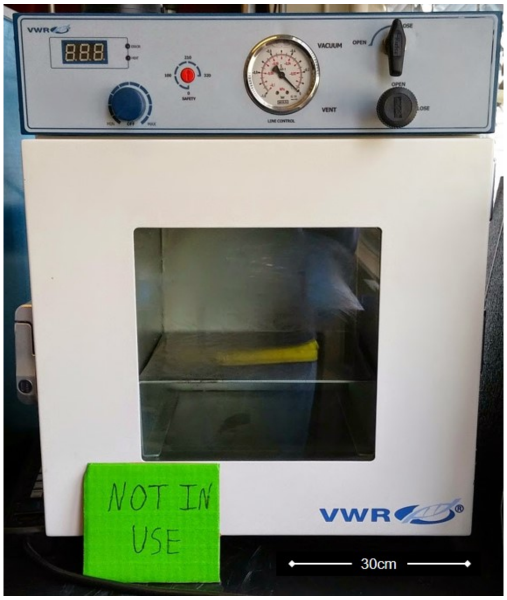

Figure 4.12: VWR vacuum oven used in DMF evaporation.

Figure 4.13: Nafion batch infusion into A-CNT process, showing 16 caged CNT systems in 20 *mL* glass vials inside vacuum oven. Vials are filled with Nafion in DMF solution, with the high vapor pressure of DMF allowing for a slow and high quality infusion.

4.3.3 Annealing Process

After allowing all the DMF to evaporate, the A-PNC is annealed at 150 $^{\circ}C$ for two hours and allowed to cool down slowly at one degree Celsius per minute. This anneal is designed to increase the crystallinity of the Nafion in the A-PNC, to increase the actuation authority of the device[10]. A lower anneal temperature would create less crystallinity, and thus a less stiff material with more strain per force, if desired. The slow cool down mitigates the chance of the structure cracking due to any thermal expansion mismatches between the multiple A-PNC materials. The A-PNC is then mechanically removed from the cage, and excess Nafion can be trimmed at this point if required. In this study it was not required, but could be completed using a standard razor blade. The completed A-PNC is then kept in a controlled environment to keep moisture ingress to a minimum. For this research, devices are always stored either in a Secador desiccator dry box (shown in Figure 4.15) or a glove box.

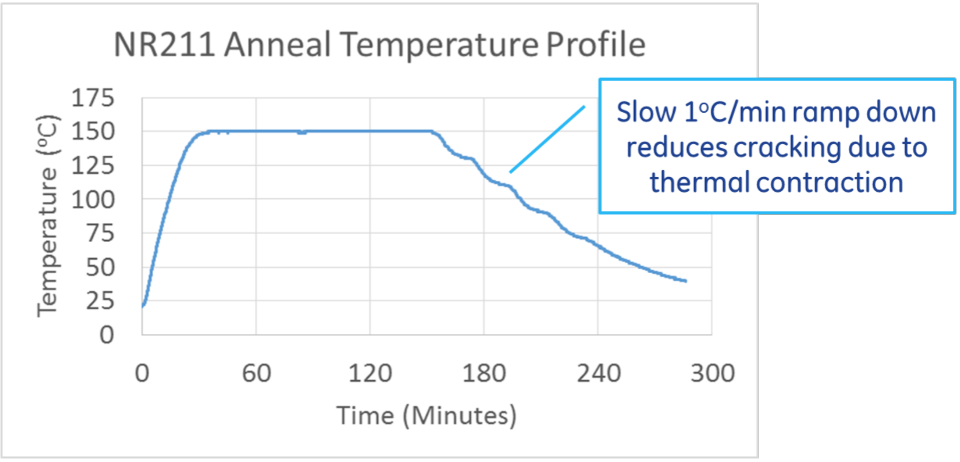

Figure 4.14: A-PNC anneal thermal profile at 150 $°C$ for higher force to strain devices, with slow 1 $°C/minute$ ramp down for reduced cracking.

Figure 4.15: Secador vertical drybox cabinet used for storage of moisture sensitive materials, including A-PNCs, Nafion, IL and silica gel (51.8 H x 34.1 W x 41.4 D cm).

Once the A-CNT PNC has been removed from the cage and trimmed, its dimensions and mass can be measured to estimate the final volume fraction and Nafion composition respectively. The Nafion uptake, or difference in A-PNC mass from A-CNT mass, is shown in Figure 4.16. The average Nafion composition from the last three batches in this study is 1.39 *mg*, or 58% of the A-CNT mass, versus the goal of 40%. This shows there is enough Nafion to allow for large strain i-EAP devices. Additional Nafion was attempted for infusion, at both 100% and up to the theoretical limit based on the available volume of the A-PNC. The average from that batch from the 40% goal samples to the >100% samples actually reduced to 50%, with a similar standard deviation. This shows that irrespective of the additional Nafion content infused above the 40% limit, there is no noticeable change in final Nafion uptake. In addition, it can be seen from the large standard deviations that some samples do exhibit larger Nafion uptake than the amount infused, which is usually an indication that the cage's epoxy or external debris has infiltrated the A-PNC. These samples are usually visibly discolored, and are generally removed from the study and not tested. Samples with lower Nafion percentage than infused usually had larger coatings on the cage and vial surfaces.

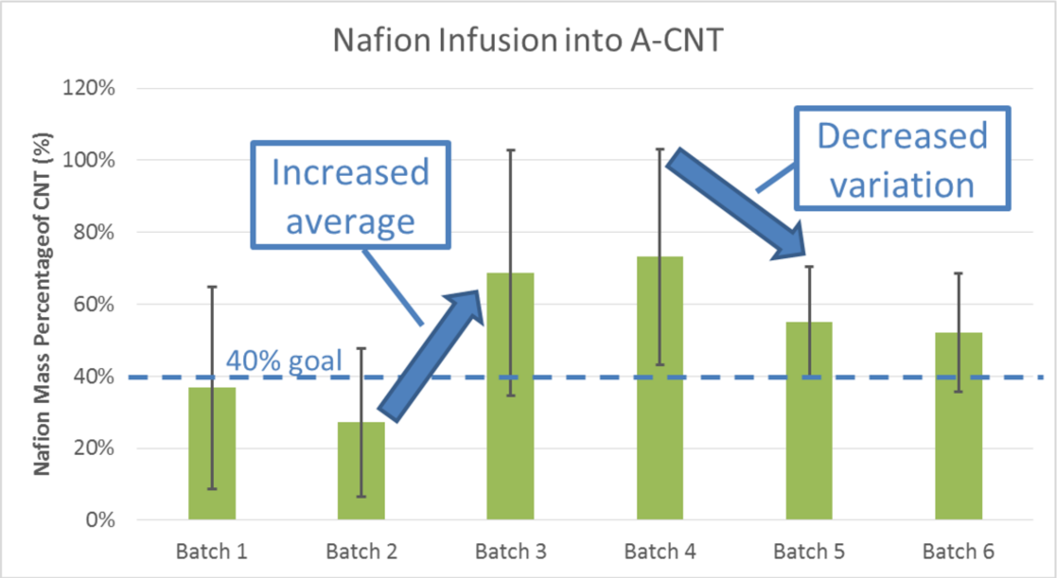

Figure 4.16: Measured Nafion uptake into the A-CNT versus the goal of 40% across various batches, showing the achieved batch average 40% uptake in the A-PNCs and increase in batch quality through reduced variation over time. In addition, studies have shown the current infusion level is near the single infusion limit.

The change in volume fraction normal to the A-CNT axis from the as densified samples to after the A-PNC creation is defined as the expansion, shown in Figure 4.17. Low volume fractions tend to contract rather than expand, likely due to the capillary densification forces. On the other hand higher volume fractions tend to expand, likely filling in any extra space inside the cages. Due to this fact, samples below about 10% Vf are not analyzed in this work, as they usually self densified to above 10% anyways, and then had large void areas created from this capillary densification.

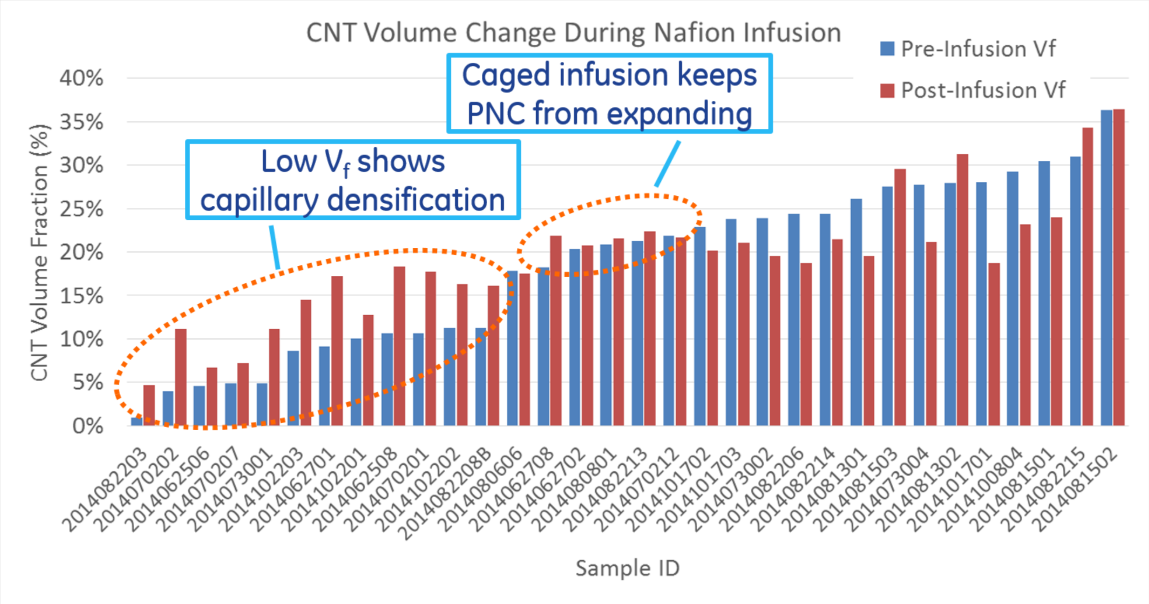

Figure 4.17: A-CNT volume change during Nafion infusion, in Vf%, from original pre-infusion A-CNT size. Low Vf samples show increase in Vf, suggesting capillary densification. Large Vfs show small variation from original pre-infusion Vf, showing cage successfully keeps A-PNC at similar sizes during infusion.

4.3.4 Airbrush Speckling

At this point, if the sample might be used for DIC, an airbrushing technique is completed to provide small speckles on the surface of the A-PNC samples[66]. The A-PNC samples are placed on the sticky portion of an upside down Post-It note, which is taped down in the fume hood, shown in Figure 4.18. Using a Badger 200G airbrush with a fine tip and 50 *psig* of compressed air, a fine mist of white paint is sprayed at the dark black samples with quick side to side motions from about half a meter away. The paint used is a mixture of Spectra intense white water based airbrush paint diluted with about 20% IPA, which is diluted to keep the airbrush from clogging. The samples are placed upside down to coat the bottom of the CNT and all sides, but not the top, due to effects of the top crust discussed in Section 5.2.

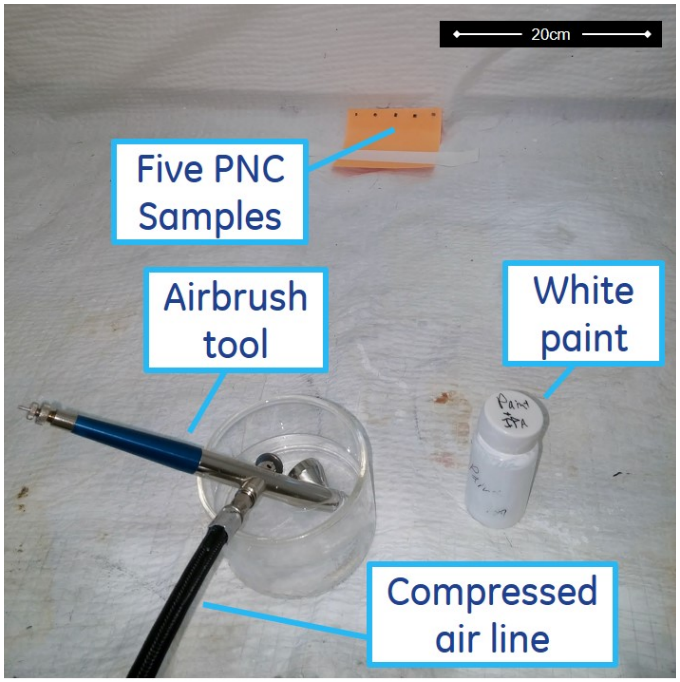

Figure 4.18: Airbrush setup used for speckling A-PNC devices inside fume hood for use with DIC. Five dry A-PNC samples are shown at top of figure on an orange Post-It in order to not fly away during airbrushing. The airbrush tool is connected to a lab compressed air line through a regulator to set the correct pressure, and acetone is used to clean the airbrush to keep it from clogging.

This method provides a very consistent speckle for use in the DIC setup for accurate strain characterization. There are about 250 dots per square m, which provides the required information for high resolution strain mapping down to a resolution of $\sim$250 μm. This assumes a minimum required information of 15 dots to create a high resolution correlation, which based on this is on average in a 0.06 mm^2 area. The 15 dots in practice seems to be a safe limit for the software's correlation detection.

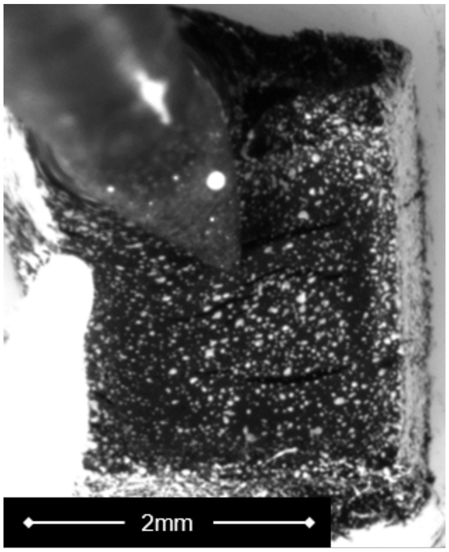

Figure 4.19: Speckled A-PNC sample showing small high density speckling for high resolution optical DIC. Image is taken facing down parallel with the CNT axis, x.

4.4 Electroactive Polymer Nanocomposite

The final step separating the A-PNC from being an i-EAP device is infusing it in the ionic liquid (IL), which provides the ions required for producing the strain within the Nafion and A-CNT composite. Based on prior work, 1-Butyl-3-methylimidazolium tetrafluoroborate (BMI-BF4) is chosen for its large difference in anion and cation sizes, mixed with propylene carbonate (PC) to optimize the viscosity for fast actuation. Since the ionic liquid's electrochemical window (ECW) is sensitive to moisture, the as purchased solution requires purification prior to infusion into the A-PNC.

4.4.1 Ionic Liquid Preparation

In order to measure the electrochemical window (ECW) of the solution to check the purity, a two probe potentiostat setup is used as shown in Figure 4.20. The purity is mostly related to moisture ingress, but could include any other chemical that effects electrochemical reactions. Two tungsten tipped electrodes are set a known distance apart, and the current versus voltage curves are measured for at least three cycles. Impurities will show up as bumps in the curve seen in Figure 4.22, and after a successful purification, a larger and smooth electrochemical window will be measured.

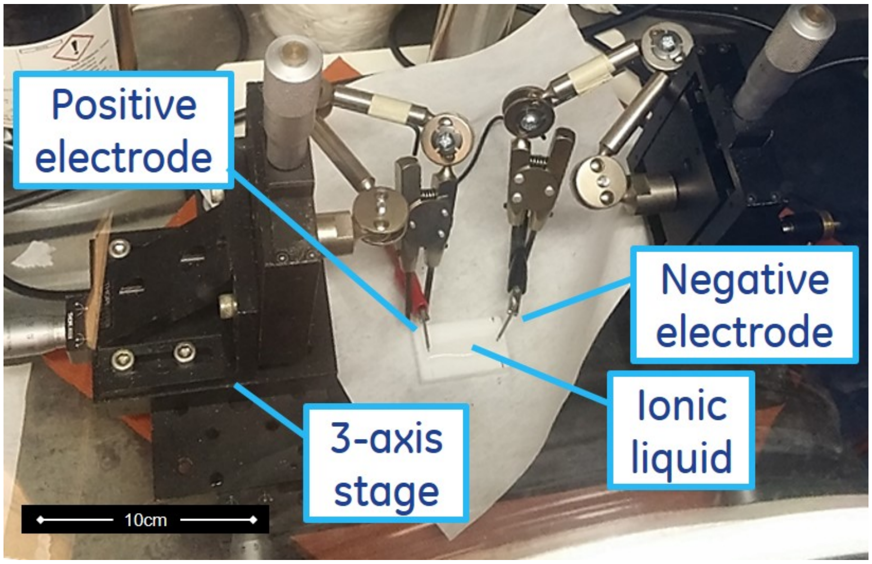

Figure 4.20: Ionic liquid two probe potentiostat testing setup, with positive (red) electrode and negative (black) electrode 3 *cm* apart in IL. Three axis microstages are used to accurately position the electrodes.

In order to purify the ionic liquid from the received 99% purity to increase the electrochemical window, the water content requires removal, accomplished using a strong vacuum for a long period of time. Increased temperature is also used to assist with this process by optimizing the vapor pressures of the mixture. The ionic liquid can undergo purification alone, or combined with the solvent that will be discussed later in this section. The as received 99% IL solution is placed under a 10 *millibar* vacuum at 50 $^{\circ}C$ for at least 2 days, or preferably over a week. These conditions were selected in order to be well below the vapor pressure of water, but still above the solvent's vapor pressure, to not change the molarity of the solution by evaporating the solvent. Water's vapor pressure at 50 $^{\circ}C$ is 123 *millibar* (92.5 *mmHg*[67]), where as PC's vapor pressure is 0.52 *millibar*[60]. The ionic liquids have negligible vapor pressure of about $10^{-10}Pa$ (much less than 1 *millibar*), keeping this from evaporating under these conditions. The improvement in the cyclic voltammogram of the purified ionic liquid is shown in Figure 4.21. In addition, the cyclic voltammogram is dependant on the scan rate of the potentiostat, with a slower voltage scan rate producing lower currents, seen in Figure 4.23.

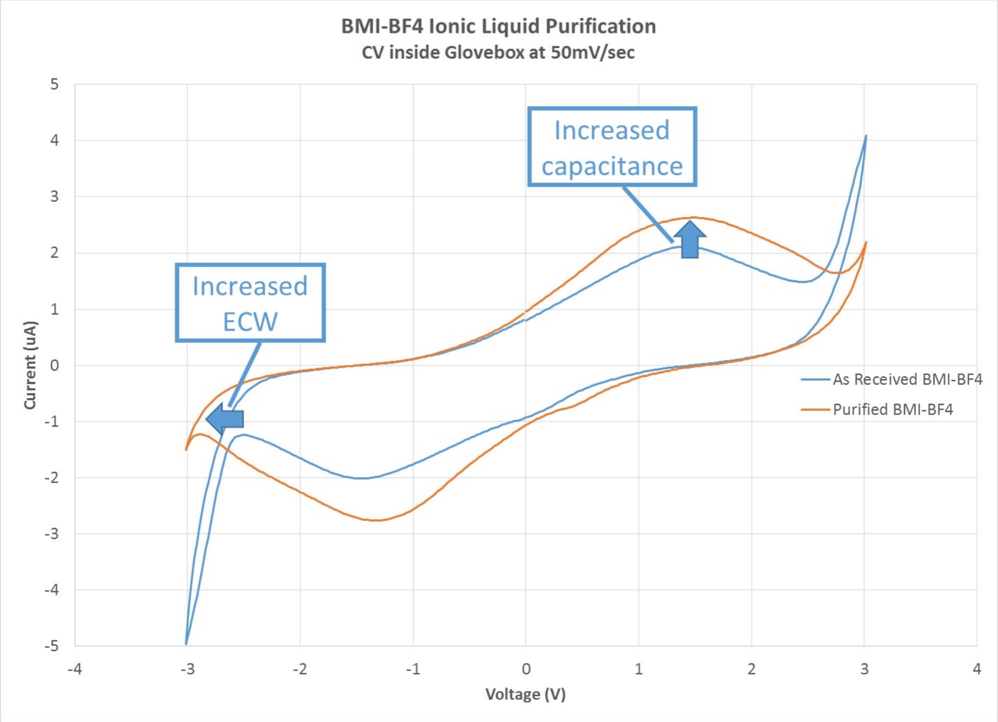

Figure 4.21: BMI-BF4 cyclic voltammogram, as received inside glove box versus after one week of purification under strong vacuum. There is both an increase in the ECW and the capacitance after purification.

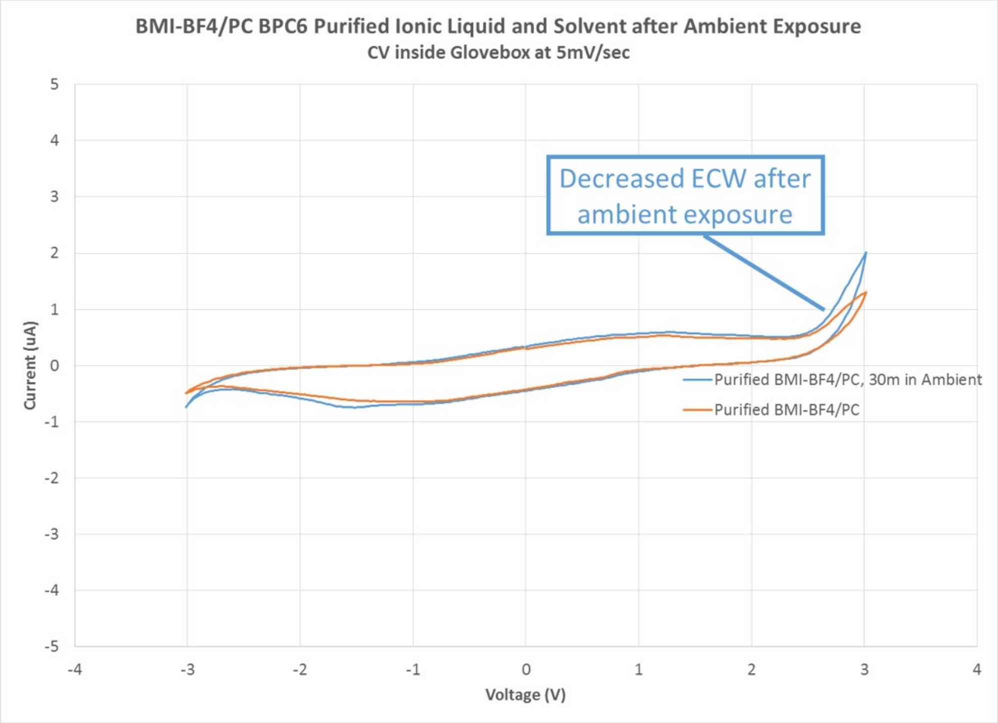

Figure 4.22: BMI-BF4/PC after purification and then 30 minutes in ambient, showing a small amount of exposure to moisture can modify the properties and reduce the ECW.

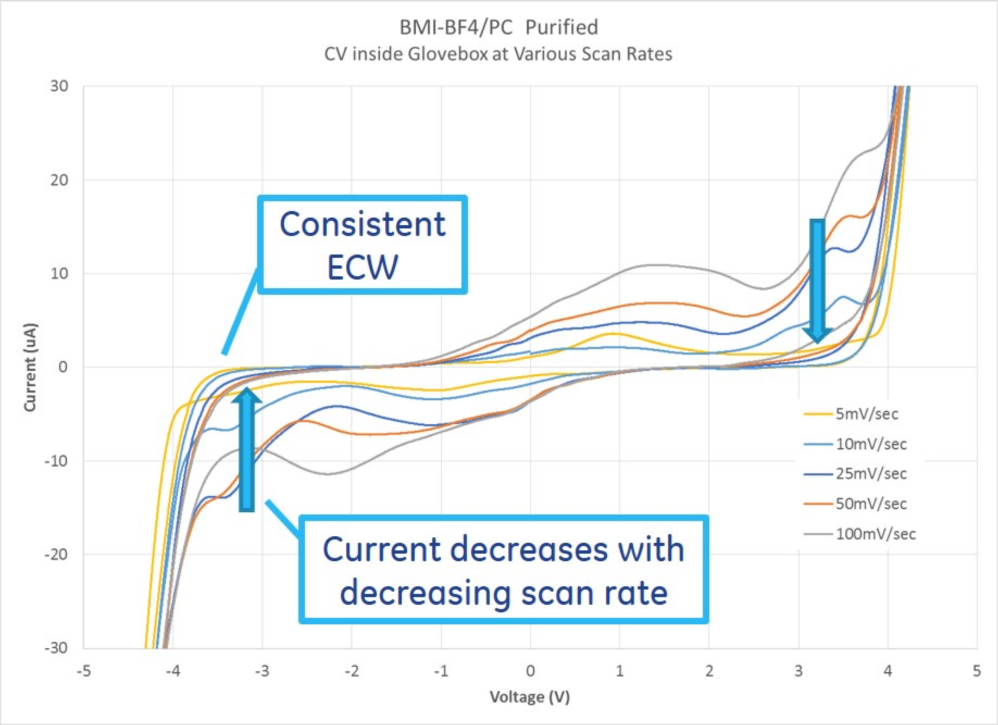

Figure 4.23: Cyclic voltammetry scan rate comparison, in BMI-BF4/PC after purification. Current varies with scan rate at constant capacitance, and ECW stays constant versus scan rate.

The ionic liquid also requires mixing with a solvent to create the correct viscosity, to allow for fast diffusion of the ions, and thus a faster actuation of the final i-EAP actuator devices. Diffusion of ions follows the Stokes-Einstein equation, shown in Equation 4.2[57]. For this reason, the BMI-BF4 IL with the large ion size difference with a viscosity of 112 cP[57] is diluted into a 2 molar solution with a low viscosity solvent Proplyne Carbonate (2.5 cP[57]). The new liquid's viscosity is assumed to be 44.5 cP using the rule of mixtures, with an estimated 250% faster diffusion rate. This also shows the importance of temperature to the system's actuation rate, as the diffusion rate is proportional to the temperature. For this thesis, all testing is completed at indoor ambient temperatures of $\sim$21 $^{\circ}C$.

$$\text{Diffusion}(T,\eta) = \frac{\mathrm{k}_b T}{6\pi\eta a} \tag{4.2}$$

The solution is prepared inside the dry glove box environment by mixing the IL with the solvent to create a 2 molar solution. Using the molar mass of the ionic liquid, this assumes a ratio of 2 moles per 1 liter of solution, and includes the assumption of the purity of the ionic liquids. The molecular weights and densities used are 226.02 g/mol and 1,200 mg/ml for BMI-BF4 and 102.09 g/mol and 1,200 mg/ml for PC[68]. Once the chemicals are mixed, they are placed in an ultrasonic bath for 5 minutes. Batches of around 20 *mL* are created at a time, enough to last many infusions. These liquids are required to be kept in a dry environment, such as a drybox, due to their hygroscopic nature. In addition, it is best to place the solution under vacuum one day prior to usage, to further purify the solutions. Interestingly, under these vacuum conditions, PC can actually slowly evaporate, causing different mixture ratios of IL to solvent, causing a non-optimal and increased viscosity. This will be further discussed in Chapter 6.

The BMI-BF4/PC solution used in the i-EAP devices in this work has a large ECW, shown in Figure 4.24. This distance from the positive and negative breakdown potentials of about 8 V is one of the largest ECWs seen in these ionic liquid solutions, showing the theoretical basis for large strain i-EAP devices.

4.4.2 Ionic Liquid Infusion

Once the ionic liquid has been purified and checked to confirm a large enough electrochemical window for actuation, the solution can be infused into the dry Nafion and CNT A-PNC samples. The A-PNC samples are placed inside 5 *mm* x 5 *mm* x 1.25 *mm* teflon trays (1.5 *cm* square outside) shown in Figure 4.25, which is placed inside a glass petri dish with silica gel (Alpha Aesar silica gel desiccant, -6+12 mesh granules) surrounding the teflon tray. A pipette is then used to submerge the A-PNC samples inside of the IL, and a flat tipped instrument can be used to lightly press on the A-PNC if required, in order to keep it fully submerged in the IL. This system is then placed into a vacuum oven and set at a high vacuum (around 10 $millibar$) at 100 $^{\circ}C$ to remove trapped air bubbles, shown in Figure 4.26. Once this low pressure is reached, it is then left at 50 $millibar$ an 100 $^{\circ}C$ for 2-4 hours. If other solvents such as Acetonitrile are used, temperatures should be lowered to around 80 $^{\circ}C$. This process yields $\sim$50% by weight of IL in the A-PNC, creating the final i-EAP device. A detailed description of the i-EAP actuator composition (IL, solvent,

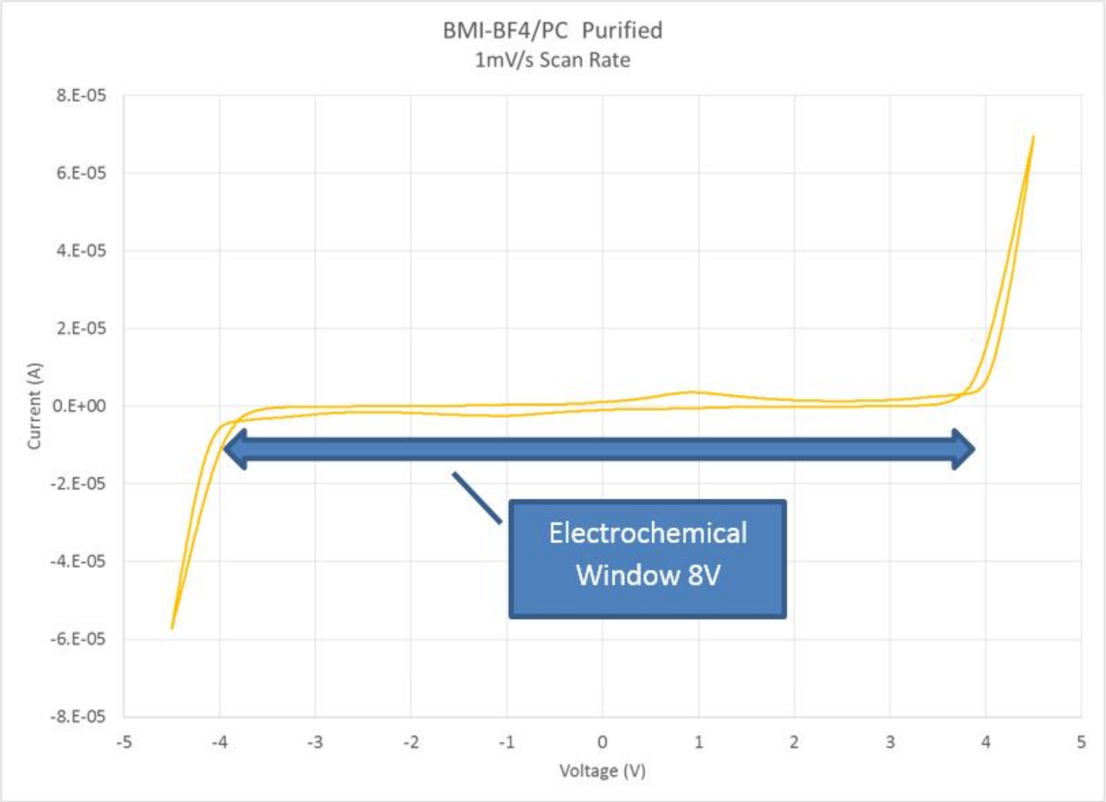

Figure 4.24: BMI-BF4/PC ionic liquid solution after purification measured at slowest scan rate of 1 $mV/second$. A large 8 V ECW is shown.

A-CNT an Nafion) is presented in Section 5.3.

Again, the amount of IL absorbed into the A-PNC can be measured by the weight change from before to after the infusion, but is more difficult to estimate due to the wet nature of the device. This is only to confirm the devices are filled with IL and is not a critical measurement, as they will be submerged in IL throughout testing. It is possible to remove excess IL using filler paper, but this method is not utilized owing to the possibility of wicking the solution out of the i-EAP device. At this point, the final i-EAP device is completed and stored in the dry glove box environment, and is ready for electrical, mechanical, morphological and electroactive testing.

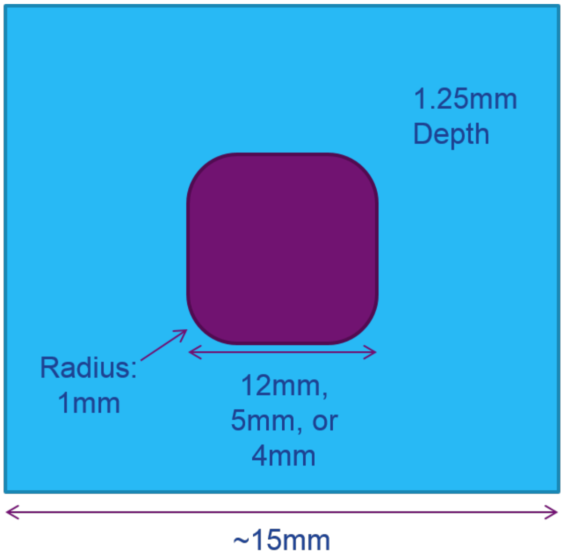

Figure 4.25: Ionic liquid infusion mold drawing, for 12 *mm*, 5 *mm* and 4 *mm* wide trays (purple area is recessed area for holing IL at A-PNC).

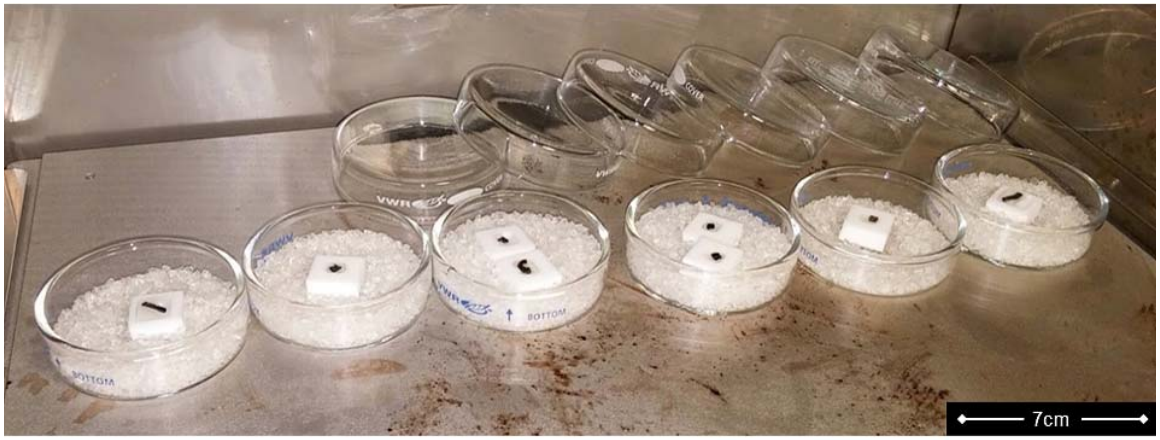

Figure 4.26: Ionic liquid batch infusion inside vacuum oven at 100 °C and 10 *millibar*. A-PNC samples situated in IL on teflon trays, placed inside glass petri dishes filled with silica gel.

Chapter 5

Results

This chapter continues on from the methods and materials created in Chapter 4, to relate the device properties to the material characteristics. The advances in the tailoring of A-CNT growth allows for characterization of the spatial and morphological properties, features of the A-PNC electrodes, and mechanical, electrical, and electroactive properties evaluation. The contributions of these findings, along with recommended follow on work, are discussed in Chapter 6. For this analysis, the axes are defined based on the CNT orientation as shown in Figure 5.1.

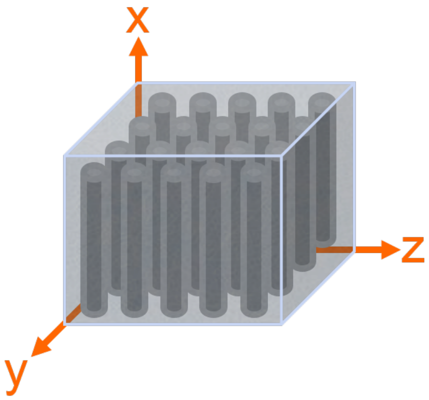

Figure 5.1: A-CNT and A-PNC local material axes, with x axis parallel to A-CNT aligned direction. This is repeated from and identical to Figure 1.1.

5.1 Growth Enhancements and Aligned Carbon Nanotube Characterization

With the updated stable and robust A-CNT growth processing (see discussion in Section 4.2), a full new characterization was completed on the A-CNT samples to verify the comparative properties to the prior growth methods. When including the updated wafer positioning, thermal profiles, water control and reduced growth times, it is estimated that the new A-CNT samples will have similar or better quality (defined later in this chapter), with very close dimensional properties to the prior materials. In order to quantify these properties, the A-CNTs have been preliminarily characterized with Raman spectroscopy, SEM, TEM and optical microscopy, looking for carbon composition, size, CNT walls and diameters, forest heights and alignment. More extensive data sets to reduce uncertainty in measured values are planned and recommended for future work.

5.1.1 Process Enhancement

The enhanced wet A-CNT growth process, defined in Chapter 4, involved a thermal CVD process of a 7.5 minute hold at 800 ± 20 $^{\circ}C$ (corresponding to a furnace set point of 740 $^{\circ}C$) and atmospheric pressure, with 500 ± 200 ppm water vapor (0.7 $bubbles/second$ or $\sim$5 $sccm$ helium bubbled through deionized water at $\sim$22 $^{\circ}C$ and controlled using a mass flow controller). The physical setup has been controlled by creating consistency in the tube location and furnace positions, and the furnace heating is made more consistent across the length by using ceramic end caps to retain more heat. Also, the wafer positions for concurrent growth are kept at -2, 0, 2 and 4 cm from the furnace mid point, which has been found to provide both consistency in forest height and a high yield of forests inside the desired heights.

With an inconsistent starting temperature, the ramp time, rate, and overshoot temperatures fluctuate, producing varying results. Figure 5.2a shows the measured variation in height with different thermal ramp and hydrogen ripening times, and Figure 5.2b shows the reduction in both height and ripening time variation from the addition of this 200 $^{\circ}C$

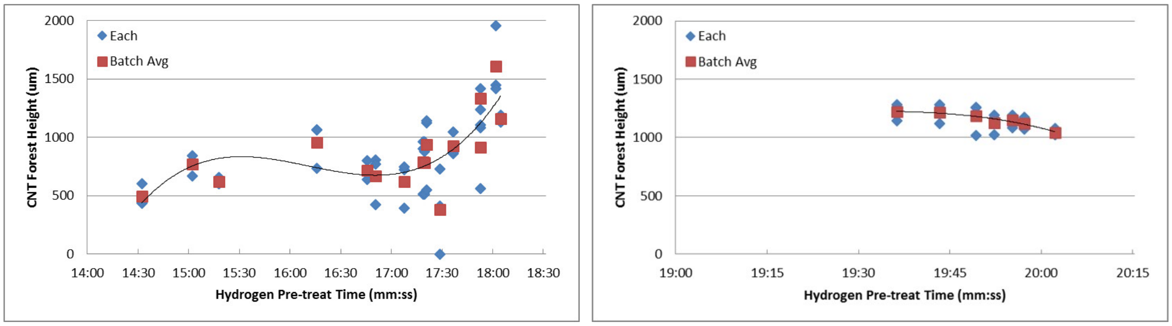

(a) Original process, without 200 °C hold.

(b) Final controlled process, with 200 °C hold.

Figure 5.2: A-CNT growth height variation versus ripening time difference from original dry process to thermal profile controlled wet process, showing stabilized process in both time and height (note different time axes). Red squares are averages of each four sample growth batch, with blue diamonds showing the single samples.

hold as discussed in Chapter 4.

The A-CNT forests are characterized between each process modification, in order to allow for each change in growth conditions to be assessed. As shown in Figure 4.6, the average Raman Ig/Id ratio (see section 4.2) of the final wet process is statistically equivalent compared to the original dry process of around 1.0. Looking further at the final A-CNT quality, Figure 5.3 shows the Raman information for a single growth across the wafer positions. This shows that all samples have similar qualities across the growth positions, ensuring stable processing independent of position within the range defined. All of this Raman data is from samples grown in building NW-14.

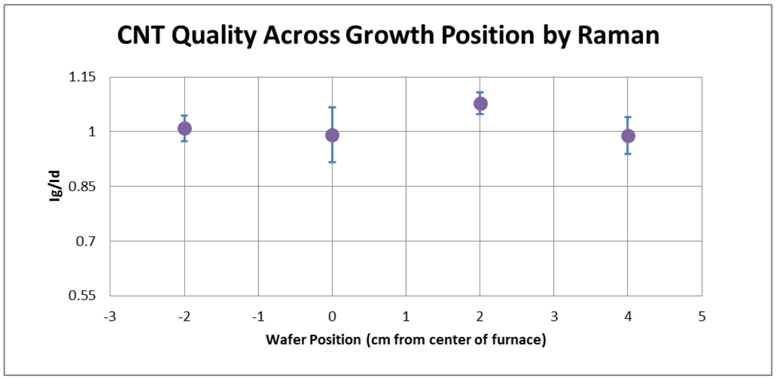

Figure 5.3: Raman integrated intensity ratios of A-CNT samples positioned across the inside of the furnace tube during a single growth, showing no significant difference in carbon composition and quality, with all ratios ∼1.0. Standard deviations shown are based on the five measurements across each sample.

In the new wet growth process, the nominal growth time is set to 7.5 minutes to achieve average heights of $\sim$1,090 μm, which is two standard deviations ($1\sigma \sim 50\ \mu m$) above 1 *mm* in order to ensure a very high yield of forests over 1 *mm*. In addition, there is a slight but consistent trend versus furnace position, shown in Figure 5.4. The 4 *cm* position is known to have on average 50 μm to 80 μm shorter average height for these 1 *mm* growths, and can be removed from the process if tighter control is needed, which has the negative impact of reducing throughput. Also, this trend in height versus position does seem to follow very closely with the predicted internal growth temperature versus position from Figure 4.8. This is expected since temperature is a key factor in the growth environment[33,34,36], and highlights the importance of the ceramic insulating end caps on the furnace. Without them, the resulting larger thermal variation across the length of the furnace would increase variation in A-CNT heights.

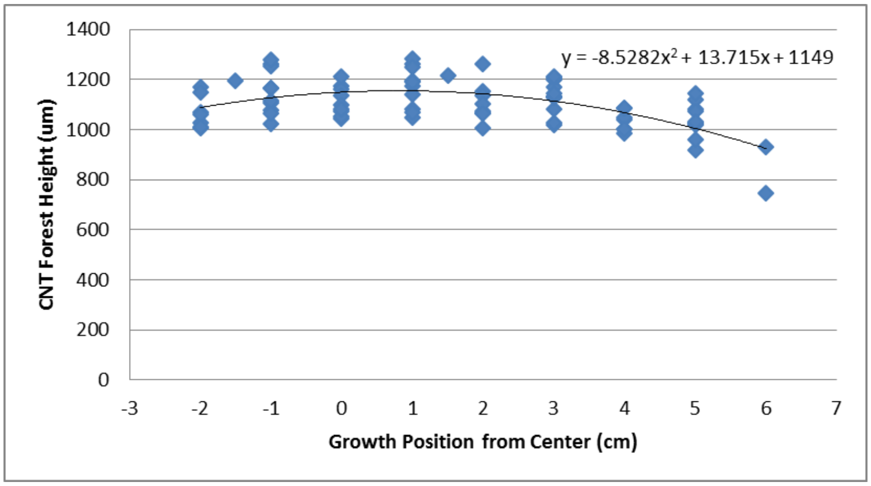

Figure 5.4: Height variation of A-CNT samples positioned across the inside of the furnace tube, showing parabolic dependance on furnace positioning. This data is based on growth batches of four to five samples at a time at various positions.

Additionally, earlier stagnation in height and termination of growth[69] is no longer seen with this processing; in prolonged growths up to over 80 minutes heights of over 5 *mm* are achieved. The heights are relatively linearly dependant on growth time, as seen in Figure 4.7. This is likely because the addition of water keeps the catalyst from being overcoated with amorphous carbon (“clean”) and able to work much longer[37], and because water adds consistency in process control and assists in a faster and more efficient forest growth.[38]

5.1.2 Scanning Electron Microscopy

Various samples of neat A-CNT forests from both the NW-14 and 35 lab locations were analyzed, primarily by SEM, to compare relative characteristics of the CNTs. From these SEMs, height, inter CNT spacing, alignment, waviness and volume fraction can be determined. In the first wide view SEM, Figure 5.5, the side of an as-grown 1% Vf forest using the new wet process in MIT building NW-14 shows the overall height of the growth at 1.18 *mm*. In addition, the vertical alignment of the nanotubes and their inherent waviness is seen. Figure 5.5b shows a closer view of the same forest, showing the alignment and spacing of the individual MWCNTs.

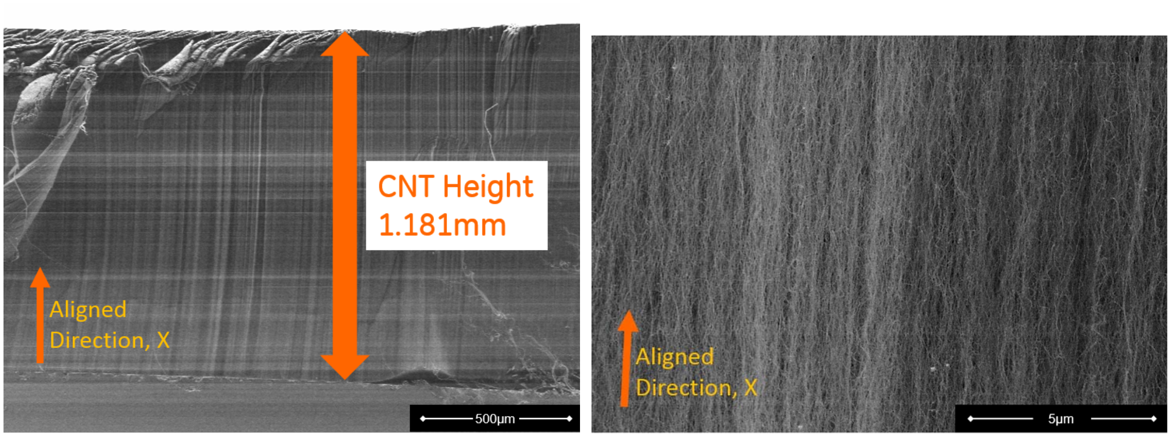

(a) 100 times zoom view of A-CNT forest. (b) 20,000 times zoom view of A-CNT forest.

Figure 5.5: SEM images of as-grown A-CNT sample's side wall showing vertical alignment and 1.18 *mm* height, acquired using 2 *keV* and courtesy of Dr. Noa Lachman (MIT). A-CNT waviness is also visible in the right image. Sample 2014062711 grown in NW-14 using new wet growth procedure.

Prior work has shown an 80 *nm* center to center spacing of the CNTs, with ~1% Vf[33]. Further characterization will be discussed in future work, confirming the initial visual characterization that these forests have the same waviness, Vf and spacing as prior work.

5.1.3 Transmission Electron Microscopy

The next microscopy method of TEM is used to further characterize the A-CNTs. The samples are prepared by sonicating the neat A-CNT in isopropyl alcohol for five minutes at room temperature in a VWR (Aquasonic) model 150D, to disperse the CNTs in the solution. A single drop of the solution is then dropped on a TEM grid for imaging. Figure 5.6 shows an example average CNT, with the inner and outer diameter measurements shown in Table 5.1. Prior forests have shown CNTs with 3 to 7 walls, with an inner diameter of 5 *nm* and an outer diameter of 8 *nm*[33,41]. The inner and outer diameter measurements shown in Table 5.1 for a single CNT largely agree with prior work, showing a similar growth process and CNT morphology with statistically . The single CNT shown has between three and four walls, with a 7.4 *nm* outer diameter. To confirm this holds for a larger sample size, more TEM images should be acquired and measured to confirm if this CNT is representative.

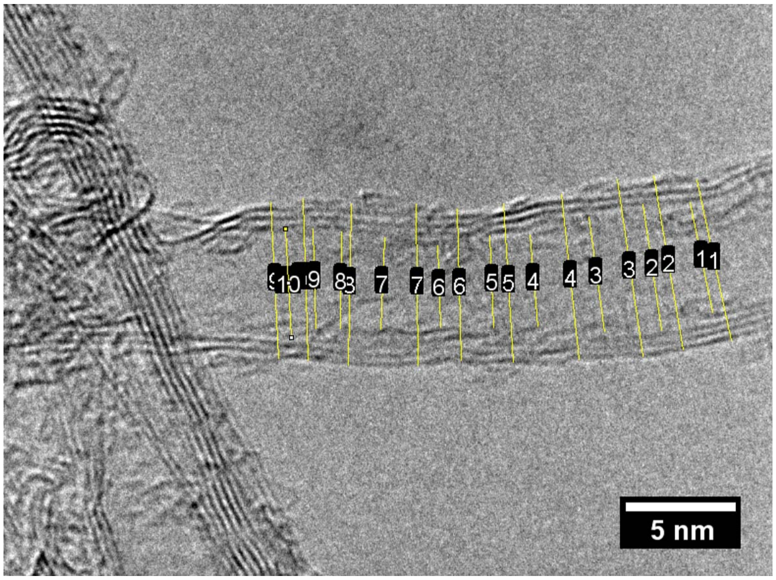

Figure 5.6: TEM of single CNT showing 4.5 *nm* inner diameter, 7.4 *nm* outer diameter and 3 walls, acquired using JEOL 2100 at 200 *keV*, courtesy of Dr. Noa Lachman.

All A-CNT characterization methods thus far have shown the new stabilized wet growth process creates similar high quality A-CNT forests to prior dry methods and CVD systems, with high Raman Ig/Id ratios, multiple CNT walls and similar diameters with strong vertical alignment. The yield on these samples once the final growth process was defined is 142/160, or 89%. Samples have failed due to excessive height above 1,200 μm (3 samples),

Table 5.1: As grown A-CNT diameters.

Measurement	**Inner Diameter** (*nm*)	**Outer Diameter** (*nm*)
1	5.063	7.405
2	5.71	7.919
3	5.215	8.039
4	4.13	7.494
5	4.121	7.158
6	3.642	6.84
7	4.12	7.246
8	4.354	7.247
9	4.493	7.051
10	4.906	7.301
Mean	**4.58**	**7.37**
Standard Deviation	**0.63**	**0.37**

low height below 800 μm (1 sample), failing to fully delaminate (13 samples), and holes attributed to debris (1 sample). This process is much better than the original process, which had a yield rate of near 48% by height alone in the first nine growths.

5.2 Polymer Nanocomposite Characterization

A consistent high quality A-PNC is necessary to accurately measure the full i-EAP constitutive parameters. To verify the similarity of these devices to ones created in earlier work on similar devices, the Nafion content and morphology are important parameters to compare. The next three sections will discuss the thermogravimetric analysis (TGA), SEM and TEM analyses of the A-PNC materials synthesized in this work based on A-CNTs grown using the new stabilized wet growth process.

5.2.1 Thermogravimetric Analysis

To accurately verify the constituents of the A-PNC, the Nafion content is measured using a TGA method, and the results are compared to the comparative weight estimates from before and after the Nafion infusion as calculated in Chapter 4. TGA is completed on a cast sample of pure Nafion, a neat A-CNT and two A-PNC samples, and is shown in Figure 5.7. The Nafion sample has been created using the same wet casting methods as the A-PNCs in separate mold, to verify the similarity in TGA response. Since the Nafion has fully degraded by 550 °*C* and the only material remaining is the CNT, the mass at that temperature is the CNT mass. It can be seen that the actual Nafion percentage of the two A-PNCs are both within 10% of the prediction using weights (about the measurement uncertainty of the scale used), which suggests the validity of the weight estimation method used for process control in this work. One known source of error is the moisture on the surface of the CNTs, which has been shown to be as large as 7 *nm* in ambient conditions, and is dependant on A-CNT Vf[40]. This can be compared to the full list of samples' Nafion uptake from Figure 4.16.

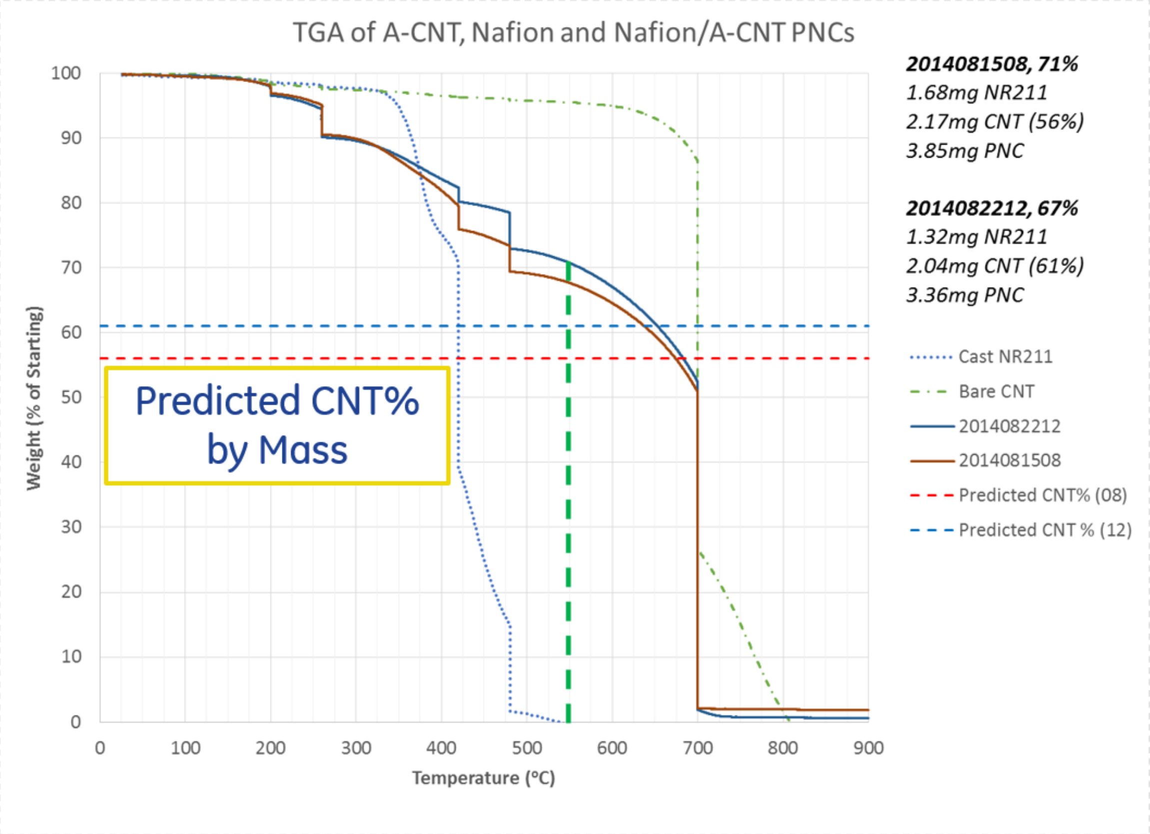

Figure 5.7: TGA of Nafion/A-CNT A-PNC and baseline samples of neat A-CNT and pure NR211 Nafion. Sample 2014082212 shows around a 70% Nafion composition, compared to the estimation by weight of 61% (1.68 *mg* NR211, 2.17 *mg* A-CNT, 3.85 *mg* A-PNC).

The TGA is completed using a TA Instruments Discovery TGA with a nitrogen environment, raised to 900 °*C* at 5 °*C* per minute with isothermal pauses before and after key inflection points in the curves. The isothermal holds are used to show variations in dynamic response, to better understand if the degradation effects are caused by time or temperature. During this testing, however, the environmental control system wasn't functioning properly, and all samples were heated under standard atmospheric air. This method works as well, since both constituents degrade fully at distinctly different temperatures.

5.2.2 Scanning Electron Microscopy

SEM is heavily utilized to compare the Nafion morphology of the A-PNC devices, as well as to compare sample variation and quality to earlier studies. Using SEM, the Nafion coated CNT diameters, excess Nafion content, debris and Vf variability can be viewed and measured.

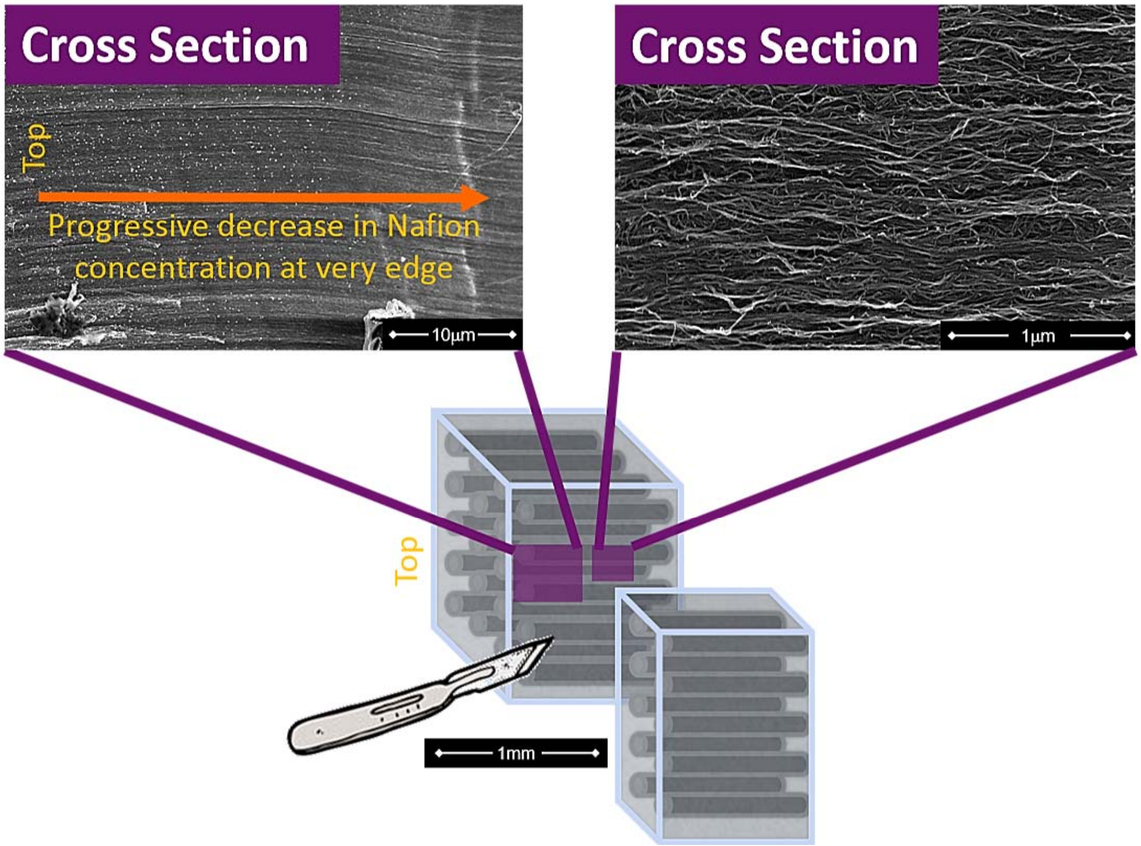

Figure 5.8: Cross sections of 20% Vf A-PNC (sample ID2014070209) from the second A-PNC batch, showing fairly uniform coating of Nafion on the A-CNT surface in the majority of the forest (~96%). Areas closer to the edges and top, as shown on the left side of the top left figure, show higher excess Nafion in particle form. Also, since there is only a conformal coating around the densified CNTs, this agrees with the large void percentage predicted for the A-PNC. SEM images courtesy of Dr. Bharath Natarajan (NIST).

Multiple samples of the A-CNT and Nafion A-PNCs have been cross sectioned for SEM, which allows for visibility of the Nafion morphology inside the bulk of the forest and to validate the uniformity. The A-PNC sectioning is completed by first creating a small incision at the side of the forest using a standard razor blade, and then cracking the sample to create a clean fracture surface. The cross section SEM images in Figure 5.8 show CNTs with fairly uniform Nafion coatings, along with additional Nafion in the form of particles. This sample is from a batch (batch two, see Appendix B) created in the middle of the work, with a fairly uniform Nafion coating, but not as uniform as final samples from batches three through six. From early samples through to the end, manufacturing improved, and coating conformality and uniformity has improved.

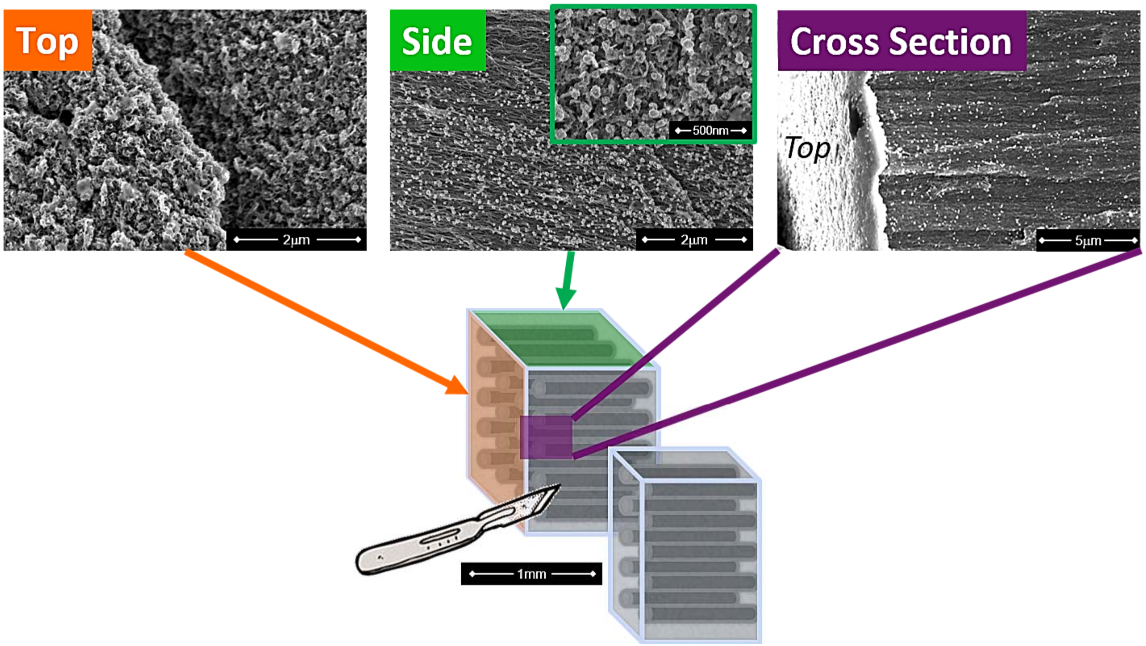

Figure 5.9: Edges of 20% Vf A-PNC (sample ID2014070209), showing Nafion crust on the top surface of the A-CNT but with fairly uniform coating of Nafion in the majority of forest (∼96%). Images courtesy of Dr. Bharath Natarajan (NIST).

Some samples have a visible crust that has formed on the top surface during Nafion infusion. Looking closer at the top and sides of the A-PNC in Figure 5.9, many of the Nafion particles are seen on the edges, in higher concentrations than in the interior of the A-PNC. There is also a higher density of these particles on the sides of the samples. The top Nafion crust is determined to be at most a couple micrometers thick using SEM images, which,

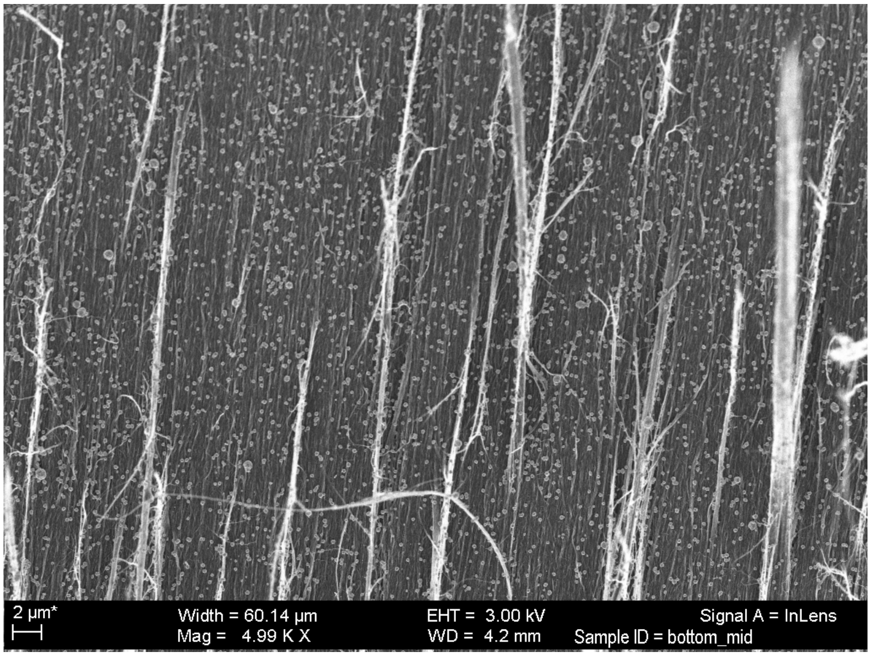

Figure 5.10: 3 kV 5,000 times zoom SEM image of the center of a 19% Vf A-PNC (sample ID2014101701), by cross section, courtesy of Dr. Estelle Cohen (MIT). The image shows the uniformity of the conformal Nafion coating, with excess Nafion particulate throughout the entire thickness of the forest. This agrees with the Nafion uptake measurements of batch 5 shown in Figure 4.16, showing the increased and more consistent Nafion infiltration of these later batches.

based on the density of the Nafion of 1.97 mg/mm^3 (50 g/m^2 and 25.4 μm thickness[53]), is less than 4% of the total Nafion infused into the A-CNT sample. This shows that in fact much of the Nafion must be infused in the interior of the forest, into what seems to be a uniform coating around the CNTs. More recent batches (batches five and six) have shown even higher infusion uniformity due to their more consistent Nafion solution processing, including additional uniformly distributed Nafion particulate throughout the entire forest thickness, shown in Figure 5.10. This has been accomplished by reducing processing variation in the Nafion solution preparation, infusion process and anneal process. The large sample uniformity can also be seen due to the controlled biaxial densification process. Due to both the presence of this Nafion crust, and the higher density growth initiation region of the A-CNTs, all sample property testing occurs with the top crust surface down, away from the DIC and electrodes.

In order to confirm the Nafion coating, the CNT diameters are measured from the SEM

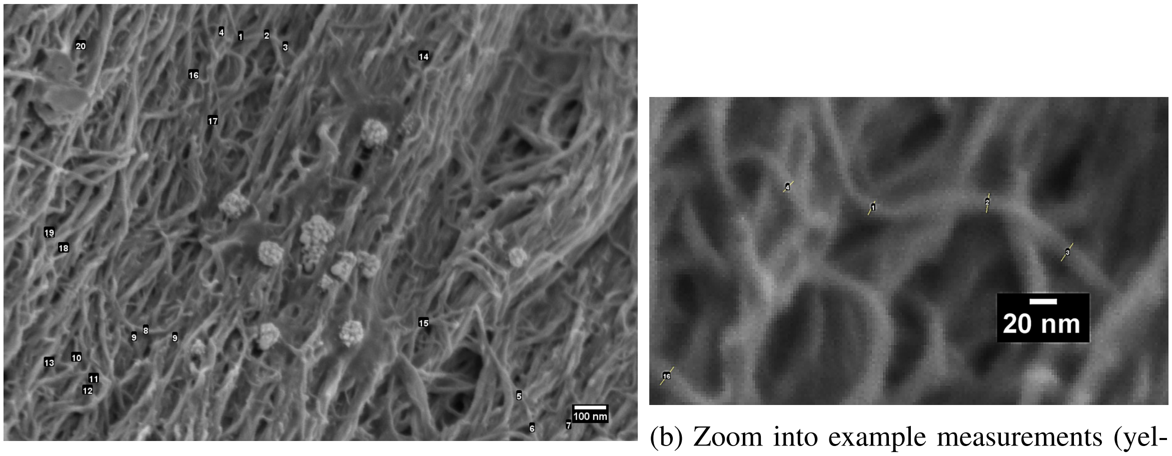

(a) Cross section, showing fairly uniform coating of Nafion and locations used in thickness measurements.

(b) Zoom into example measurements (yellow lines) used to define Nafion coated CNT diameters with ImageJ software.

Figure 5.11: SEM images of 19% A-PNC sample's (sample ID2014101701) cross section with vertical alignment, with measured thicknesses shown in Table 5.2. Images courtesy of Dr. Estelle Cohen (MIT).

images using ImageJ software. Figure 5.11 shows a sample of the interior of the forest in a cross section, and measured locations to determine average CNT diameter. Selecting 20 locations that look like single CNTs, an average thickness of 12.2 *nm* is measured. Comparing this to the as grown CNT diameters, a conformal coating along the entire interior of the forest of about 2.5 *nm* is calculated.

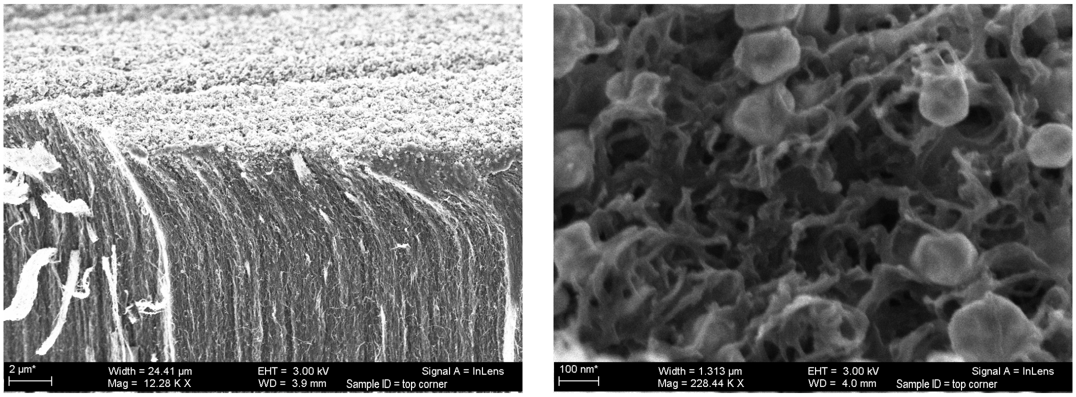

(a) Cross section showing uniform coating on interior of A-PNC with thin crust on top.

(b) Zoomed image showing top crust morphology as sporadic particles.

Figure 5.12: SEM images of 19% A-PNC sample's (sample ID2014101701) cross section with vertical alignment, showing uniform coating in interior of the A-PNC and crust of Nafion on the top, less aligned, growth initiation region. Images courtesy of Dr. Estelle Cohen (MIT).

Table 5.2: Measured Nafion coated CNT diameters.

Measurement	Diameter (*nm*)
1	10.9
2	13.8
3	14.8
4	10.4
5	12.5
6	12.2
7	10.5
8	13.4
9	11.5
10	10.8
11	11.3
12	10.0
13	9.4
14	12.9
15	12.0
16	16.0
17	11.5
18	11.8
19	11.9
20	17.1
Mean	12.2
Standard Deviation	2.0
Min	9.4
Max	17.1
Mean Nafion Thickness	2.5

These more recent samples showing increased uniformity also include reduced outside crust thicknesses, with only sporadic particles instead of a continuous layer. Figure 5.12 shows the thin crust of a more uniformly infused sample, as well as the increased interior uniformity as compared to Figure 5.9. In addition, the high density of particles on the sides is no longer seen in these samples. These recently manufactured A-PNC samples (batches three through six) can be compared to prior A-PNCs created at Pennsylvania State University (PSU)[54]. Figure 5.13 shows a defective, or flawed, A-PNC created at PSU that was not used for i-EAP devices. It shows not only a similar Nafion crust layer on the top of the A-PNC, but also similarly uniform Nafion coatings around the CNTs. This sample was never used based on the meso-scopic void structure throughout the sample as shown in Figure 5.14, further explaining the requirement for slow and controlled Nafion infusions.

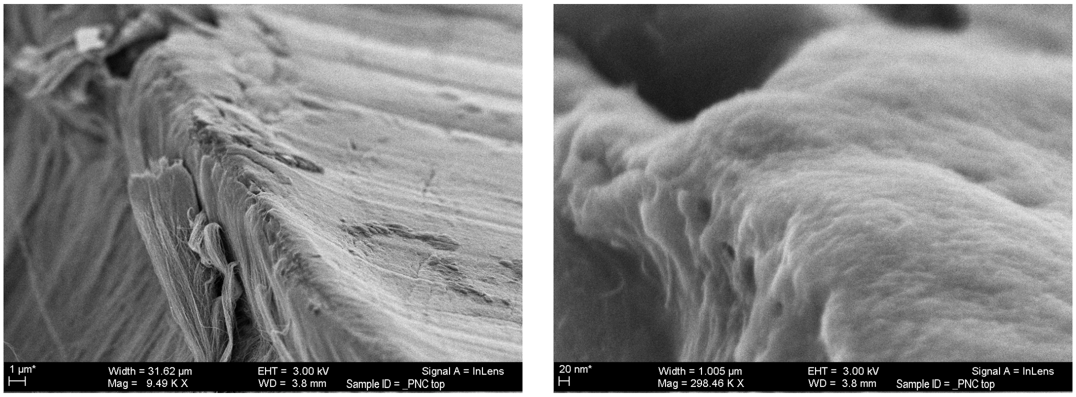

(a) Cross section showing uniform coating on interior of A-PNC with crust on top.

(b) Zoomed image showing top crust morphology as continuous coating.

Figure 5.13: SEM images of Penn State University A-PNC sample's cross section with vertical alignment, showing uniform coating in interior of the A-PNC and similar but thicker crust of Nafion on the top surface than seen with MIT samples above. Images courtesy of Dr. Estelle Cohen (MIT).

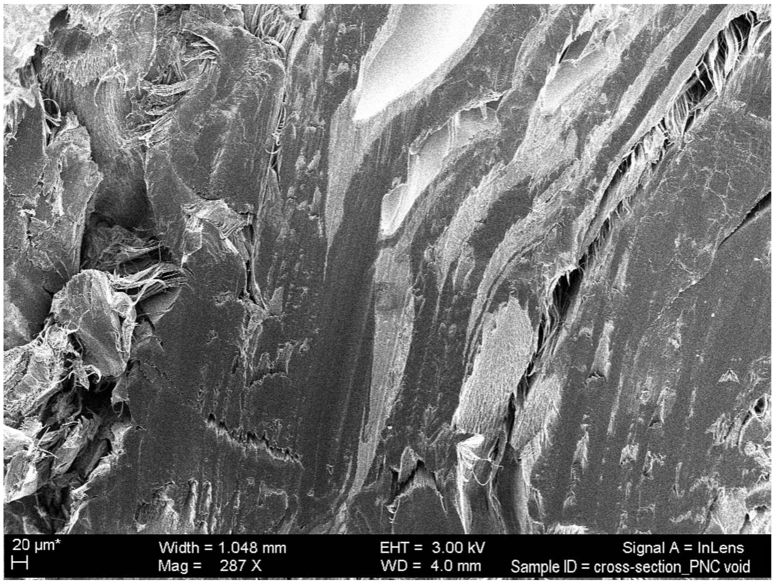

Figure 5.14: SEM of flawed A-PNC cross section courtesy of PSU showing non uniform morphology and voids, courtesy of Dr. Estelle Cohen (MIT).

In order to confirm similarity in A-PNC morphology and structure from recent devices to earlier devices, a high quality PSU A-PNC sample published in 2010 can be compared to the 19% Vf A-PNC sample in this work. When comparing Figures 5.12a and 5.15, the images show similar Vf, Nafion content and overall morphology.

One interesting discovery in recent higher quality A-PNCs is formations of what seem

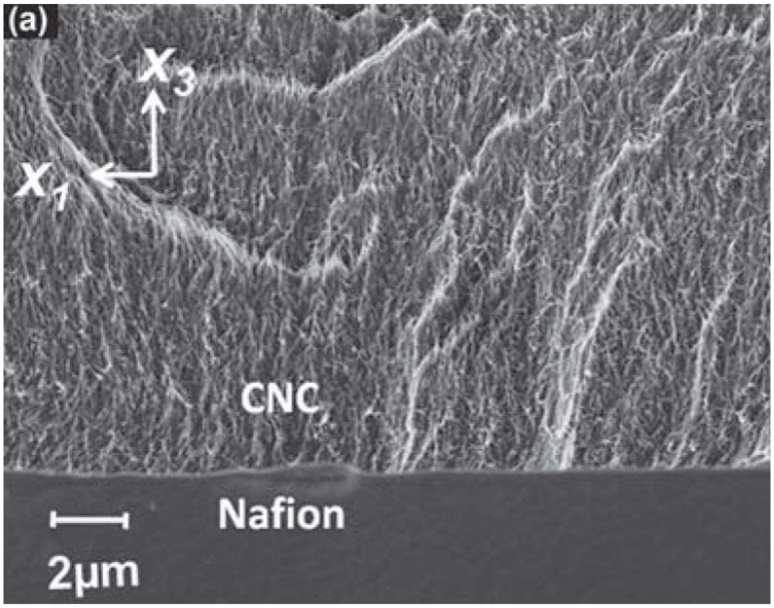

Figure 5.15: SEM of original high quality PSU A-PNC device cross section, with uniform Nafion coating and aligned CNTs[54].

to be semi-crystalline Nafion structure surrounding single CNT pillars. Similar structures have been found around nanotubes, such as the electrochemically formed lithium peroxide toroids[70]. Figure 5.16 shows a hexagonal Nafion structure found around a CNT in a Nafion and A-CNT PNC sample. Nafion normally exhibits low degrees of crystallinity[71], unlike polytetrafluoroethylene (PTFE) which exists in at least 4 known phases depending on pressure and temperature and includes both strong hexagonal and pseudohexagonal crystalized forms[72]. PTFE's crystallization phases have been widely investigated[73], where as Nafion's are more difficult to examine using standard diffraction scattering techniques[71]. The Nafion structure in general does seem to exhibit a similar hexagonal lattice similar to PTFE[71], which might explain this phenomena on the CNTs.

5.2.3 Transmission Electron Microscopy

In order to see finer details of the CNT and Nafion thicknesses and morphologies, TEM is required. A novel three dimensional focused ion beam (FIB) TEM method based on the work from Natarajan et al.[8] is attempted on the A-PNC samples. A thin section of the A-PNC from the side is milled using FIB, and can then be imaged using TEM at many

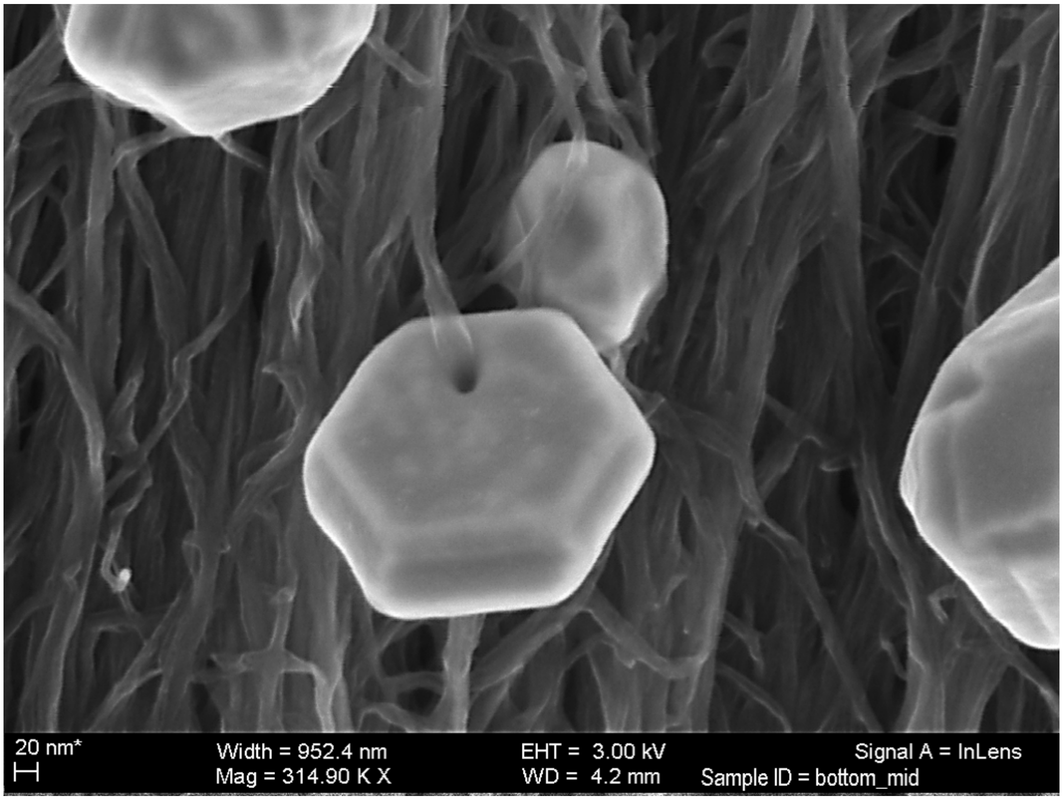

Figure 5.16: SEM of new hexagonal crystalline Nafion structure seen around a single CNT in the middle of the sample ID2014101701. These type of structures seem prevalent throughout the interior of the A-PNC, and likely formed during the Nafion infusion and annealing process. Image courtesy of Dr. Estelle Cohen (MIT).

angles for a clear three dimensional image. Unfortunately due to the high packing density of these high Vfs A-PNCs which also include Nafion polymer, when a section is milled off the specimen becomes a relatively solid piece and is difficult to image. Figure 5.17 shows a TEM prepared by the FIB technique, and the low contrast recovered.

Efforts are ongoing to try to generate better TEM images of the A-PNC to be used for three dimensional imaging. The A-PNC samples are too dense and rigid to be dissolved using sonication under IPA, even after a very long duration. New preparation methods being investigated include removing A-PNC fiber bundles after a cross section is completed using the method described for SEM sample preparation above, or to microtome thin samples embedded in epoxy. The first method, in which fiber bundles are placed directly on the TEM grid, might not be able to see single CNTs since most will be bundled. The microtome method's risk is that the epoxy will not be noticeably different than the Nafion

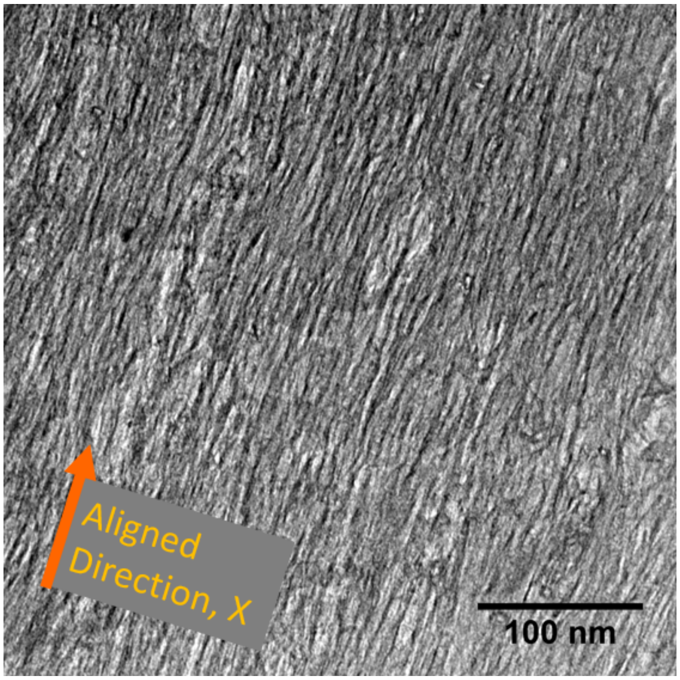

Figure 5.17: TEM prepared by FIB method from 20% Vf PNC sample (ID2014070209) showing high packing density of high volume fraction A-PNC and low contrast, courtesy of Dr. Bharath Natarajan (NIST).

polymer in the TEM. One TEM has been successful in imaging a single CNT via the microtome method, shown in Figure 5.18. This largely confirms the measurements in Tables 5.1 and 5.2, again showing a conformal $\sim 2.5\ nm$ thick coating on the CNTs. However, as this is only a single CNT sample, this may not be representative.

This section has shown the consistent morphology of the Nafion and A-CNT PNC samples across recent batches (batches three through six), which provides the basis for the i-EAP active devices. The fully Nafion coated CNTs create microscopically consistent void free materials for testing as i-EAP devices in Section 5.3, with an annealed, seemingly semi-crystalline Nafion structure. In addition, in some samples there is excess Nafion on the top crust, so the top crust is placed on the bottom for all property testing to limit the potential impact of this morphological edge effect. A summary of two example A-PNCs are shown in Tables 5.3 and 5.4, with densities less than 1 mg/mm^3 and combined Nafion and CNT Vfs of 35% to 55%. The full list of A-PNC samples is shown in Appendix B.

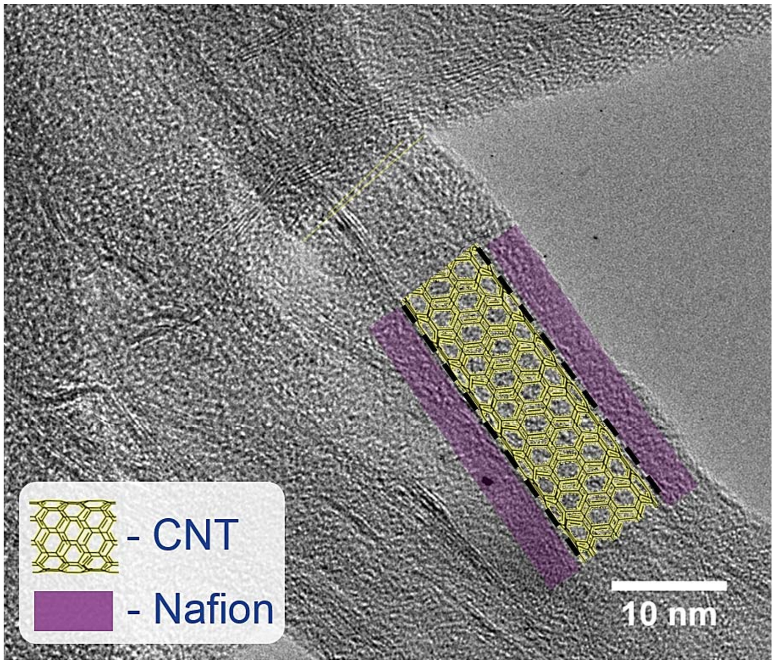

Figure 5.18: TEM of 20% Vf A-PNC sample showing single CNT walls with conformal Nafion coating, courtesy of Dr. Estelle Cohen (MIT). The CNT outer diameter is measured to be 9 *nm*, and the Nafion outer diameter is measured as 14 *nm*, very similar to the SEM Nafion measurements and CNT TEM measurements.

5.3 Electroactive Polymer Device Characterization

In order to derive the material's full constitutive model, electrical, mechanical and electroactive testing is required. Once good quality i-EAP devices are ready for testing, they are stored in the glove box environment to maintain a moisture free environment to limit device degradation. The four subsections that follow will go through equipment, testing methods, and results from multiple volume fraction devices with and without ionic liquids, with all samples taken from recent higher yield and controlled morphology devices (batches three through six, see Appendix B).

The final composition of select i-EAP samples are shown in Tables 5.3 and 5.4, with calculated A-PNC and i-EAP densities and Vfs. The device volume is assessed by measuring the A-PNC x, y and z device dimensions, and the Vf of the A-CNT is defined assuming the as grown forest before densification is 1% with an intrinsic CNT density of 1.6 mg/mm^3 [41,74]. The density shown is for single CNT. Numbers with an asterisk have been calculated based on the other known data. One item to note is that the mass of the

IL solution in the i-EAP samples is calculated from the void fraction and volume of the A-PNC and the density of the IL solution. The actual measured weights after infusion of the IL are generally larger than this estimate, due to excess IL on the surfaces. This difference also could be due to the mass change from releasing moisture somewhere during the processing, reducing the mass originally measured on the CNTs by the mass of the moisture, which can be as large or larger than the A-CNT mass itself[40]. These values of density and Vf also show the very high porosity of the A-PNC materials when completed, and the high IL content required to fill these voids.

Table 5.3: i-EAP device composition for 40%Vf sample, ID 2015021302, with a total volume of 4.49 mm^3.
**Calculated based on the other known data*

Material	Density (mg/mm^3)	Mass (mg)	Vf (%)
CNT	1.6	3.13	41.0
Nafion	1.97	1.16	13.1*
PNC	0.96*	4.29	54.1*
BMI-BF4/PC	1.2	2.47*	45.9*
I-EAP	1.51*	6.76*	100.0

Table 5.4: i-EAP device composition for 20%Vf sample, ID 2014101704, with a total volume of 8.66 mm^3.

Material	Density (mg/mm^3)	Mass (mg)	Vf (%)
CNT	1.6	2.74	18.6
Nafion	1.97	2.71	15.9*
PNC	0.63*	5.45	34.5*
BMI-BF4/PC	1.2	6.81*	65.5*
i-EAP	1.42*	12.26*	100.0

5.3.1 Electrical

The cyclic voltammetry is completed using an Autolab PGSTAT30 potentiostat and the included GPES v4.9 software. Two probe testing is typically used in testing energy devices as the total sample voltage is the parameter of interest, and contact resistance is not a large concern. Tungsten probes are chosen as they are typically the probe for electrochemistry of i-EAP devices. The probe used is a 0.5 *mm* diameter pure tungsten welding electrode made by Global Tungsten and Powders that has been sharpened to a ∼0.1 *mm* tip at one end using a Dremel tool. All electrical and electroactive testing is completed using a two i-EAP setup, with both devices fully immersed in the liquids. The devices each have a tungsten electrode connected to them using a physical contact method with the arms cantilevered to have minimal contact force. Special BNC through connections are installed in the front plexiglass of the glove box to allow for the electrical connections, and the glove box internal metal surfaces are grounded to the potentiostat. The probes are positioned using two sets of three axis thorlab microstages to contact the samples and control position for the DIC camera. A view of the samples under test from the DIC camera is shown in Figure 5.19, fully submerged in excess ionic liquid. The positive sample is on the left, and the negative sample is on the right.

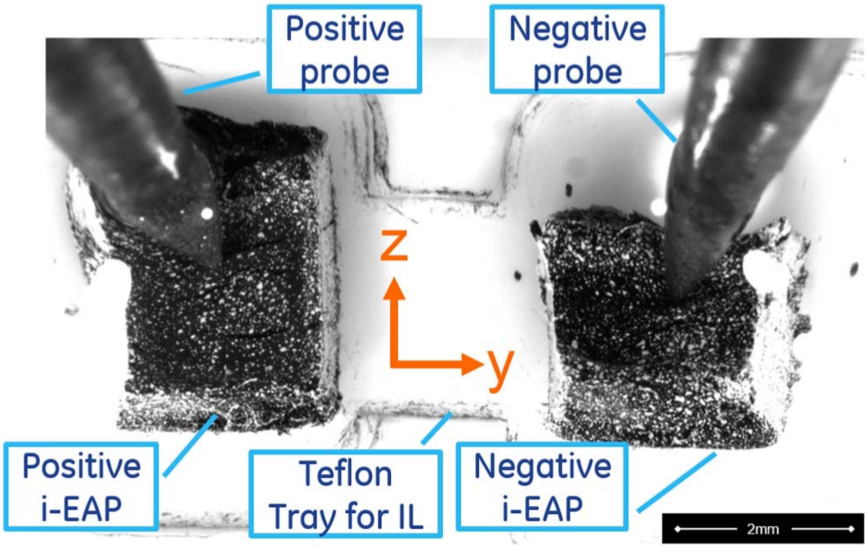

Figure 5.19: Two electrode i-EAP setup with two new devices prior to electrical testing through the DIC camera (discussed subsequently). Camera images of device's y-z plane.

The standard voltage waveform applied is a constant scan rate of 5 $mV/second$ from -3 V to 3 V in a continuous cycles. This sawtooth waveform is shown in Figure 5.20. The voltage level of plus and minus 3 V is chosen based on the electrochemical window shown for the ionic liquid testing, Figure 4.24. Other testing that does not use the IL has worked with up to ±4 V ECWs.

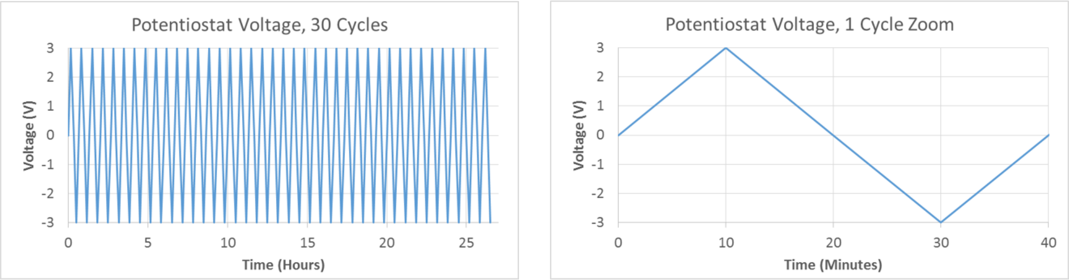

(a) Full applied 30 cycles of voltage.

(b) One cycle of applied voltage.

Figure 5.20: Voltage application waveforms, showing -3 V to 3 V ramped waves at 5 $mV/second$ scan rates.

One item tested early in the development was the contact resistance of the electrodes versus a full area copper tape contact. This is to confirm the assumption that the entire device is being utilized due to the high conductivity across the A-CNT network, and that a full sputtered or glued metal contact is not required for transverse conductivity. If a full width electrode was required, it would have altered the free boundary conditions of the devices used for strain inference. Figure 5.21 shows the difference in capacitance through the current voltage (CV) plot between a full copper tape electrode on each device and the standard tungsten probes. The two traces are almost identical which shows that both methods have a similar capacitance, and thus use a similar conductive surface area with both contact methods.

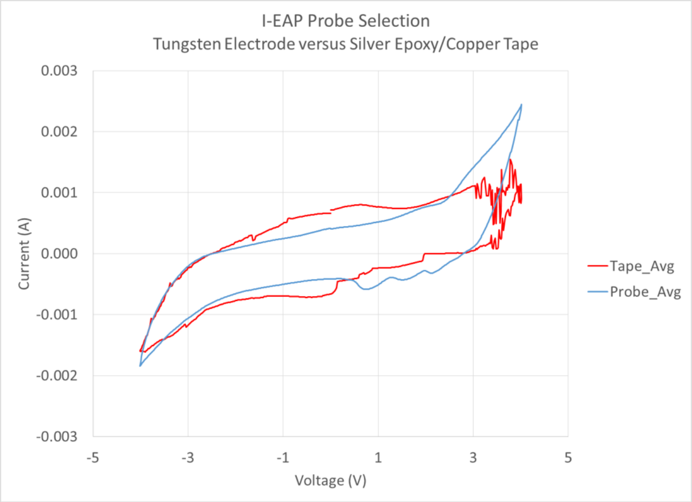

Figure 5.21: Cyclic voltammetry measurement of i-EAP devices using the standard tungsten probe versus devices silver epoxied to copper tape. Samples ID2014082202 (positive) and ID2014082205 (negative) devices tested at 5 mV/s from -4 V to 4 V.

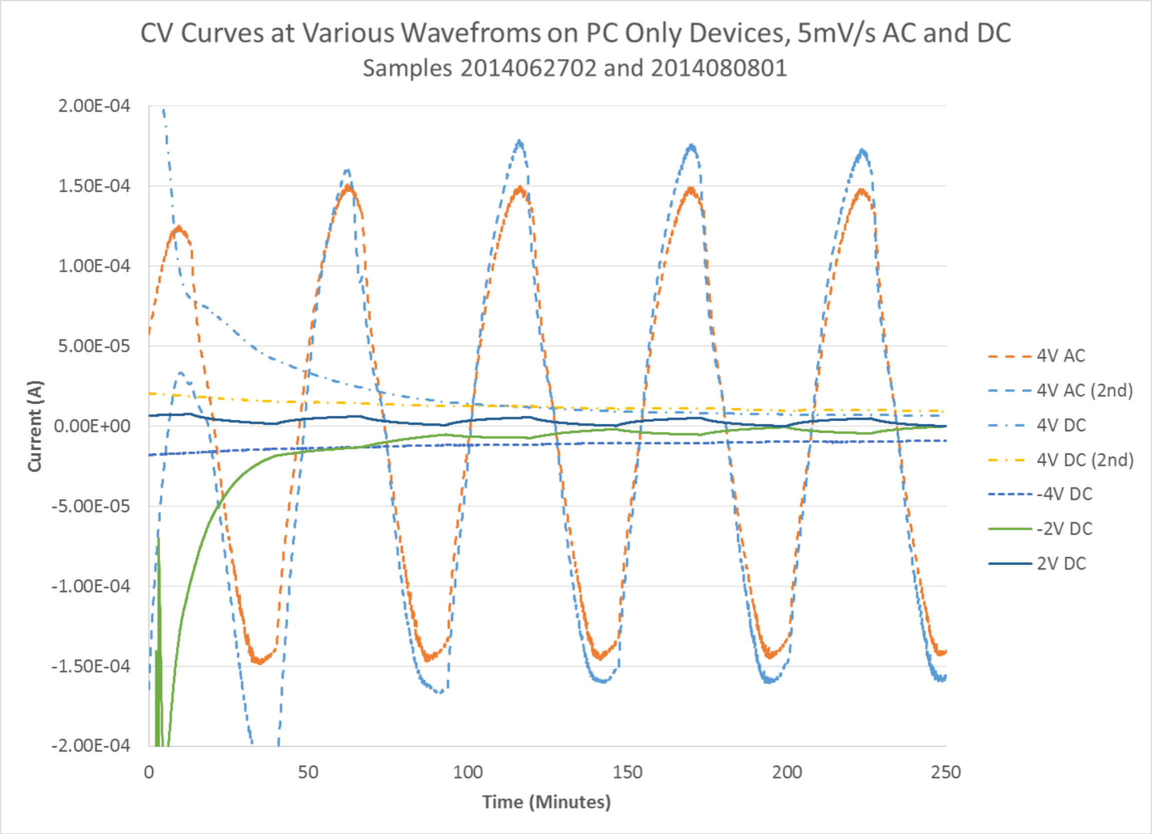

Figure 5.22: Cyclic voltammetry measurement of i-EAP devices using solvent only, with the asymptotic DC response showing it takes ∼100 minutes to fully stabilize. Samples ID2014062702 (positive) and ID2014080801 (nagative) have tested under multiple DC voltages, as well as repeated AC cyclic tests.

The i-EAP devices are first tested using only the solvent propylene carbonate: a polar, aprotic solvent. This test method is dependant on the ionomeric properties of the Nafion material and its ion exchange capability. Multiple voltage waveforms are tested in both AC and DC methods, to show not only the response to voltage scan rates, but the time to fully charge a device. Figure 5.22 shows a long term application of 4 VDC, 2 VDC, -2 VDC, -4 VDC and two sets of 30 cycles of 4 V to -4 V AC. This shows the asymptotic decrease in current with charging the devices over time, and that the device currents reach a steady state with DC voltage within about 200 minutes. These devices are likely responding very slowly due to the large device thickness and high capacitance. The DC voltages are applied in an alternating positive to negative sequence after allowing the devices to fully stabilize at the prior DC voltage, which allows for the maximum current generation that is useful for showing the asymptotic timing of the device, not to demonstrate a consistent magnitude in current. The variation of current based on the initial condition of the device is shown by the 4 VDC (2nd) trace which started with less severe initial conditions, which is less initial current than in the first application. They both however stabilize to a similar final conditions. Figure 5.23 shows the cyclic voltammetry results from these same devices through 30 cycles of AC testing.

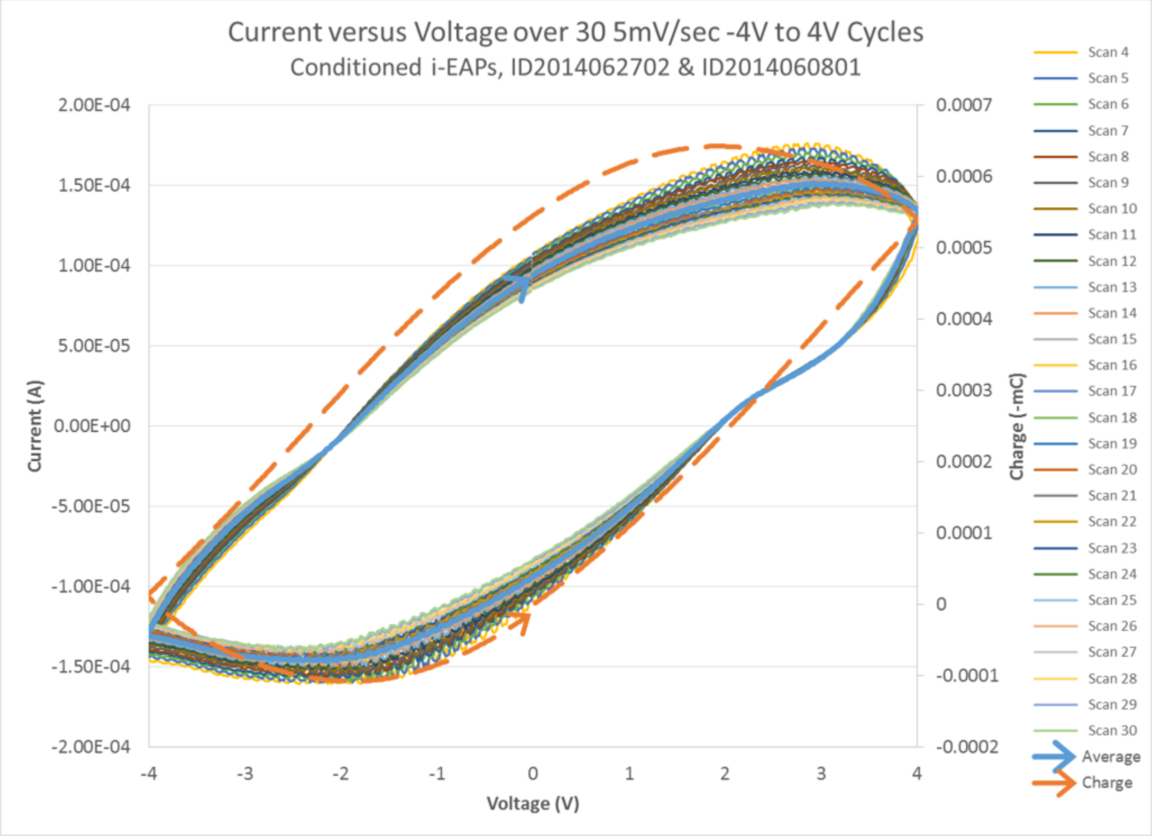

Figure 5.23: Cyclic voltammetry measurement of i-EAP devices using only the PC solvent under 30 cycles of $\pm 4\ V$ AC applied voltage. The average of the middle curves 15-17 is shown in the thicker blue line, with its calculated accumulated charge in the dotted orange line. The ripples seen in the single curves are attributed to the movement of the CNTs and the varying resistance to each other and the probe.

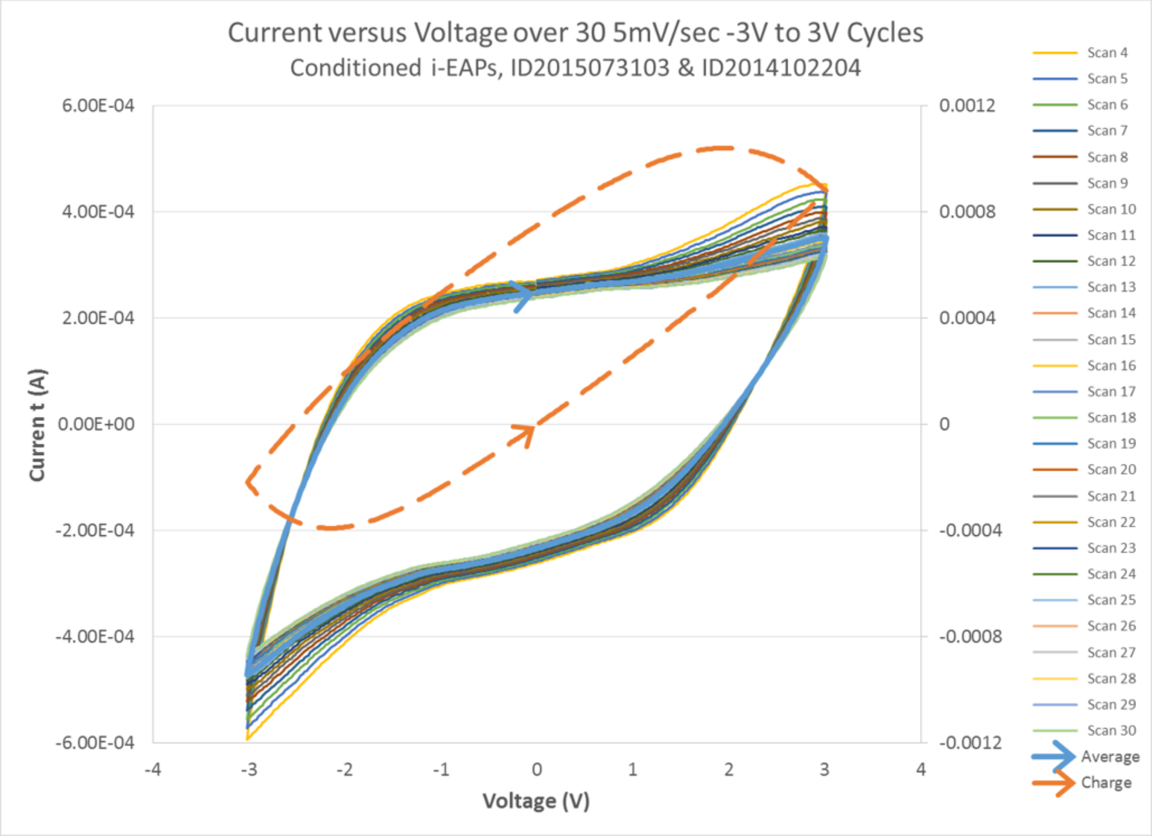

Figure 5.24: Cyclic voltammetry plot of i-EAP devices under a ± 3 V waveform at 5 $mV/second$, including calculated charge accumulation in the devices.

Figure 5.24 shows the cyclic voltammetry testing results from 30 voltage cycles on 12% Vf and 30% Vf i-EAP devices, manufactured in the final batch, six. This CV curve is a much more ideal rectangular capacitive curve compared to a more resistive curve using only the solvent (Figure 5.23), which suggests a better actuation potential. The total capacitance for a single electrode device measured in series is defined by Equation 5.1, based on the integral of the discharge current (I_d, when the current is less than zero), the voltage range (ΔV), and the voltage scan rate ($\frac{dV}{dt}$). The multiplier of 4 is to define the capacitance of a single device, accounting for the measured current being reduced by two capacitors in series at constant scan rates and also that it is measuring the total capacitance for two electrode devices (see Figure 5.19)[48]. Figure 5.25 shows the CV curves for devices with a similar Vf (22% and 24% Vf samples ID2015021303 and ID2015073102) tested at multiple scan rates. Based on Equation 5.1 with the voltage range of 6 V and a 5 $mV/second$ scan rate, these devices give a 0.37 F capacitance each, for a specific capacitance on the positive

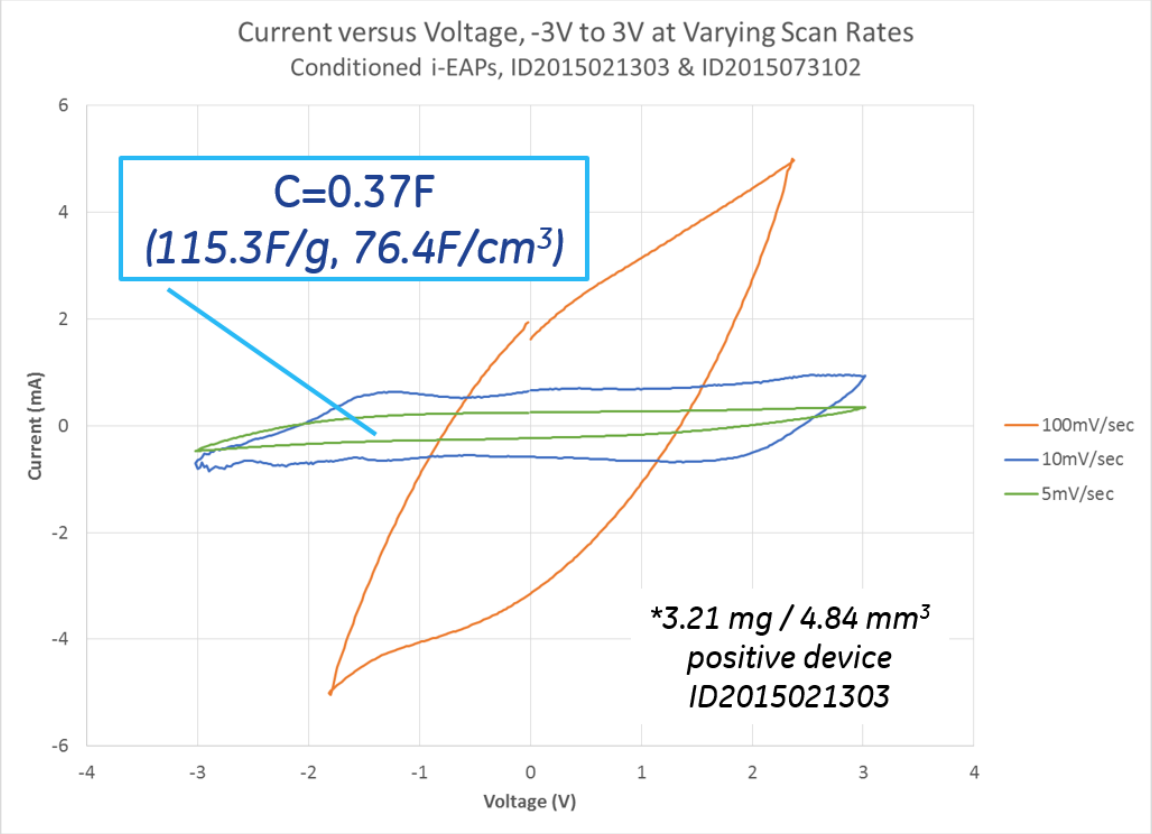

Figure 5.25: Cyclic voltammetry plot of i-EAP device under a ± 3 V waveforms and varying scan rates, showing specific capacitance of 115.3 F/g or 76.4 F/cm^3, similar to prior non-coated CNT based supercapacitors[48].

device (ID2015021303, 22% Vf A-CNTs) of 115.3 F/g based on the dry PNC mass, or 76.4 F/cm^3 by volume. As expected at 10 $mV/second$ the capacitance is slightly lower, at 0.27 F, and again reduces to 0.07 F at a scan rate of 100 $mV/second$. These values match up well with similarly structured A-CNT based supercapacitors[48].

$$C = \frac{4\int \mathrm{I_d}\, \mathrm{dV}}{\Delta \mathrm{V}(\frac{\mathrm{dV}}{\mathrm{dt}})} \tag{5.1}$$

From the capacitance, the dielectric permittivity of a single electrode device (ε_{ik}) is calculated by using Equation 5.2 based on the Debye length of the ions in the IL (κ^{-1}) and the active surface area of the A-PNC, (A). The A-CNT specific surface area has been experimentally measured on 1% to 20% Vf 1 mm A-CNT samples as 776.8 ± 16.3 m^2/g[40]. Since the specific surface area is related to the area of the CNT "cylinder" with a linear relation to radius, the specific surface area of the A-PNC is scaled based on the ratio of the Nafion and CNT radii by 1.65 times (7.4 *nm* to 12.2 *nm*) to 1,280.7 m^2/g. The Debye length of an electrolyte is defined in Equation 5.3 as a function of ionic molarity (I_M) of the electrolyte, the permittivity of free space (ε_o), the relative dielectric permittivity (ε_r), Boltzmann's constant (k_B), the absolute temperature in kelvin (T_K), Avogadro's number (N_A), and the elementary charge (e). Based on a linear mixture of the BMI-BF4 and PC 2 molar solution, the IL relative permittivity is predicted to be ∼45 and is used to calculate the Debye length. For this 2 molar solution of IL, the Debye length is calculated to be 5.15 *nm*. For the 22% and 24% Vf samples ID2015021303 and ID2015073102 with a capacitance of 0.37 F, this means the permittivity is 7 x 10^{-10} F/m, or a relative permittivity of 78.9. In this work, electrodes were only tested in a configuration with the electrodes facing each other in the y direction with contact in the y-z plane. It is assumed the permittivity of the material would be similar in the x direction with contact in an x plane since the conductive Vf is similar and the Debye length and specific surface area should be independent of direction, but this should be confirmed in future tests.

$$\varepsilon_{ik} = \varepsilon_o \varepsilon_r = \frac{\mathrm{Cd}}{\mathrm{A}} \tag{5.2}$$

$$\kappa^{-1} = \sqrt{\frac{\varepsilon_\mathrm{r} \varepsilon_\mathrm{o} \mathrm{k_B T_K}}{2\mathrm{N_A e^2 I_M}}} \tag{5.3}$$

5.3.2 Digital Image Correlation

DIC is used to calculate two dimensional strain fields on the i-EAP devices in a non-invasive and high resolution optical manner. The DIC method is used in both mechanical and electroactive testing, to calculate the strain in mutliple dimensions, with the strain then used to calculate the coupling coefficients, modulus and Poisson ratios. A PointGrey GRAS-50S5M-C camera sensor with a Tamron SP 180 *mm* F3.5 Di 1:1 macro lens is used in this work, connected to a computer using Firewire, with images acquired using the Correlated Solution's Vic-Snap software. Correlated Solutions' Vic-2D 2009 software then calculates displacement and strain in multiple dimensions from these high resolution images, particularly based on correlating the movement of the white speckles described in

Section 4.3. In order to reduce noise in the calculations, a large 75 by 75 correlation block is set with a shift of 9 pixels to smooth the strain field data. In addition, a powerful 3,000 lumen light source (Fiber-Lite Machine Vision MH-100 metal halide fiber optic illuminator) is aimed at the samples under test through a dual branch bifurcated fiber optic light guide. This helps by allowing the shutter speeds of the images to be less than 10 *milliseconds* in order to limit blurring due to building vibrations. The strain resolution with this 9 pixel shift is shown in Figure 5.26, along with the correlation window size for i-EAP device testing.

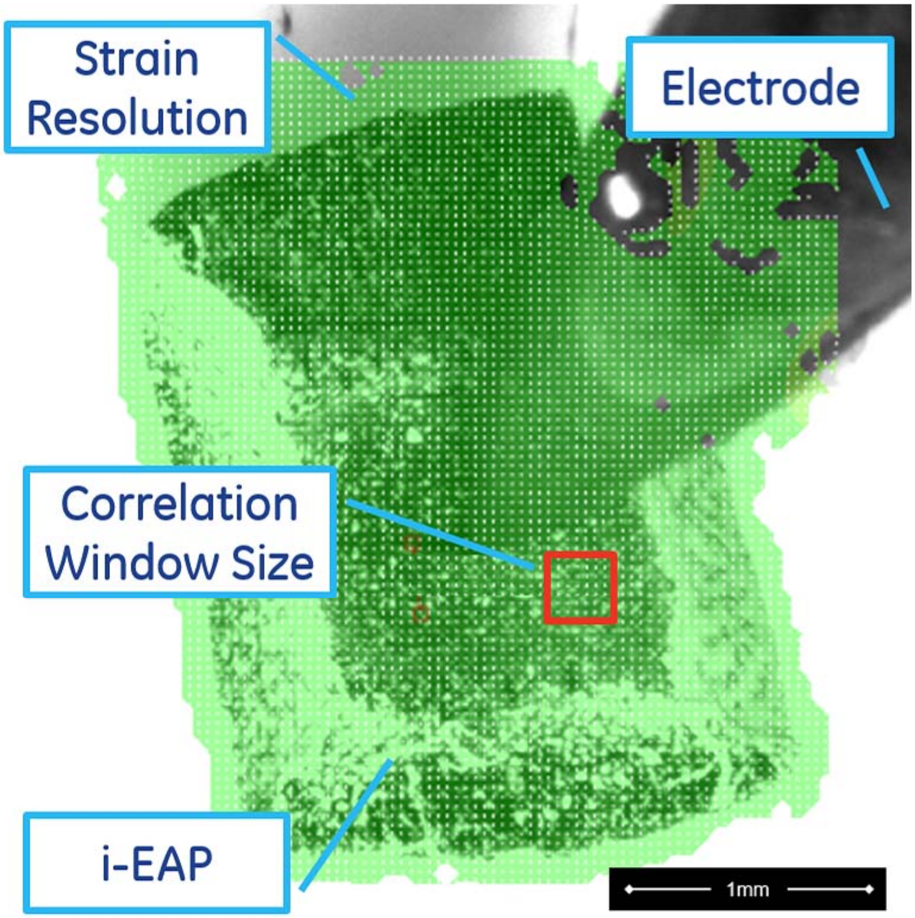

Figure 5.26: Resolution of the digital image correlation (DIC) system, with each calculation point (every 9th from the original image pixels) shown as white dots, overlayed on to the sample under test. The green area is the visualized strain from these calculated points. The 75 by 75 correlation window is shown in red. Strains shown that overlap the electrode are ignored.

5.3.3 Mechanical

The A-CNT, A-PNC and i-EAP samples are all characterized for mechanical constitutive relations using a Zwick / Roell Z010 universal material testing machine and the testXpert II v3.31 testing software. Compression testing is chosen due to the limited size of the test samples, and inability to insert them into dog bone or similar tensile test specimens. A modified ASTM D695 "Standard Test Method for Compressive Properties of Rigid Plastics" is used to measure the material's Young's modulus, and could also be used to measure the yield stress, deformation beyond the yield point, and compressive strength[75]. The standard is modified by utilizing smaller sample dimensions than the suggested 12 by 12 by 25 *mm*, but is still expected to yield reasonable results for Young's modulus. A 10 *kN* load cell measures the force, and the Zwick sets the displacement. For compression testing, flat metal platens are attached to the top and bottom of the Zwick, with the sample placed in the middle on the lower platen. Figure 5.27 shows the compression platens setup for testing, and a sample inside. As suggested in ASTMD695, for compliant plastic materials, a toe-correction method is required to accurately calculate the elastic modulus at a near linear portion of the curve. Figure 5.28 shows the original raw strain to force curve, as well as the corrected curve and tangent line used for calculating the toe-corrected tangent modulus. This method is applied to all data following in this work to account for load take-up in the compression tests. In addition, the same DIC setup described in the previous section is used with the compression testing. The same light sources are aimed at the sample, and the same method is applied to calculate the 2D strain across the sample. A sample DIC image is show in Figure 5.29.

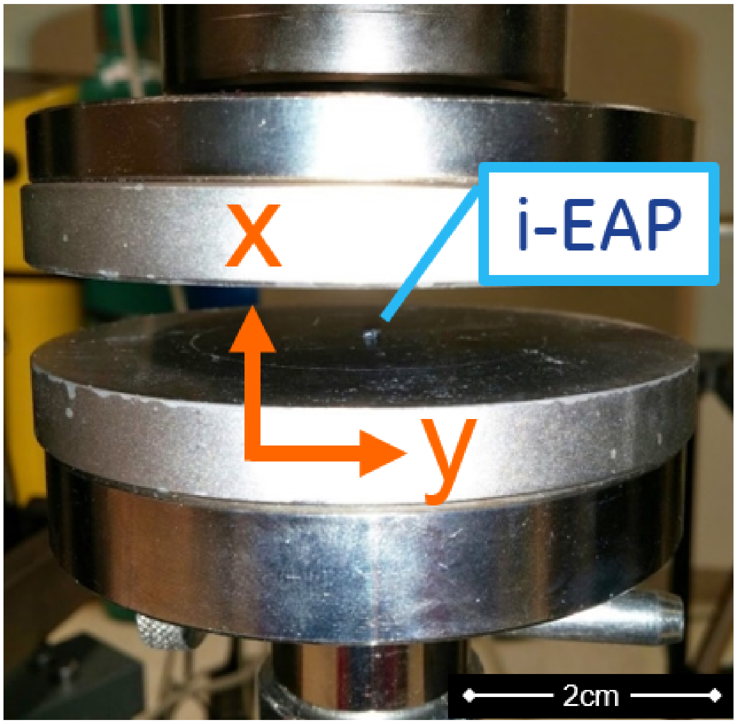

Figure 5.27: Zwick compression platens used for compressive modulus testing with i-EAP device inside. A smaller top platen is sometimes used instead with DIC to allow for additional light on the sample.

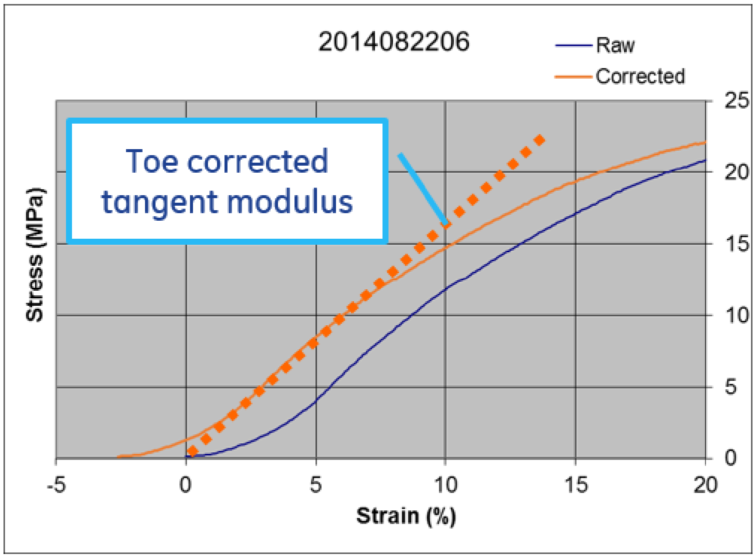

Figure 5.28: Modulus calculation and toe correction method as specified in ASTMD695, applied to linear portion of force versus applied strain curve. Strain in this figure is measured using the displacement measurement of the Zwick, on 19% Vf sample 2014082206 without IL (therefore the sample is an A-PNC with 19% A-CNTs Vf, 12% Nafion, and 69% voids by volume).

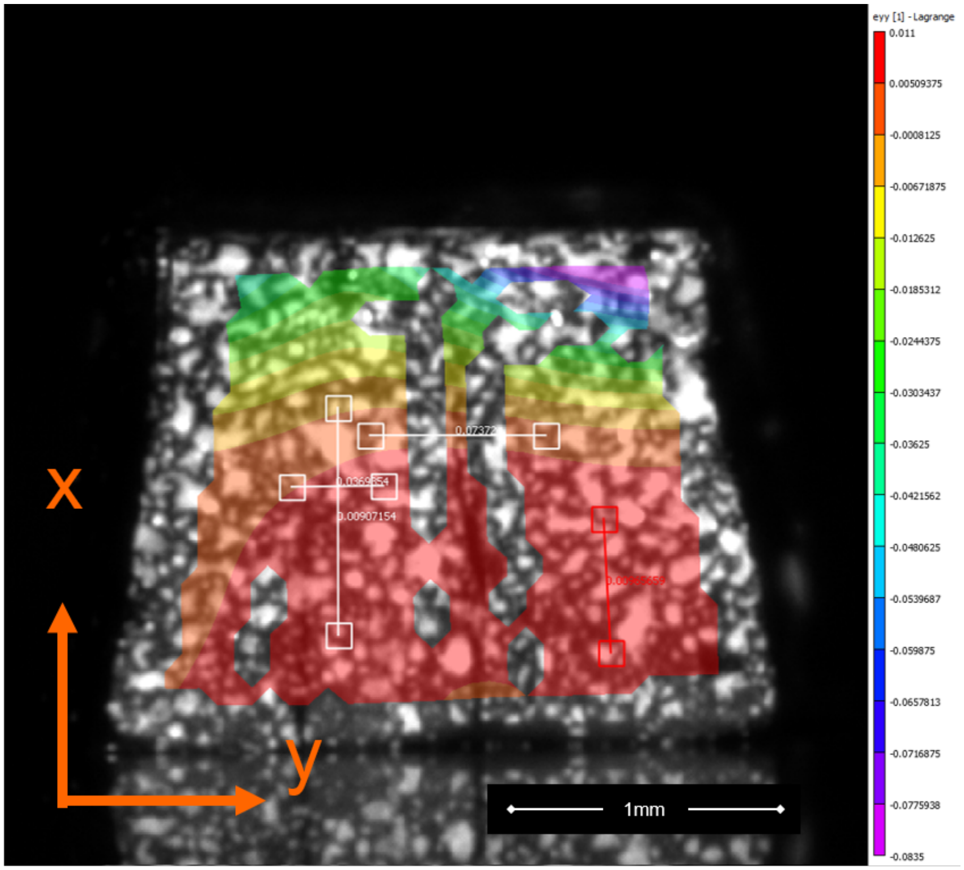

Figure 5.29: Strain measurement image on sample ID2015011701 using 2D DIC system with f11 aperture and 10.5 $\mu second$ acquisition speed during Zwick compression test, near 10% compression. White lines with boxes at each end are virtual strain gauges used in strain calculation. Taper in sample due to non-uniformity in densification and Vf causing uneven Poisson response during compression.

Initially, neat A-CNT samples are tested to compare the A-CNT compression modulus versus prior work based on nano-indentation testing. Chapter 2 discusses the results of this Oliver-Pharr test method and the expected differences versus direct compression testing. Figure 5.30 shows the compression test data from multiple Vf samples of pure A-CNTs in light blue, versus the nano-indentation results in dark blue with the dashed line. As expected, the nano-indentation modulus based on the unloading shows a value about 40 times higher than that of compression testing. Again, this is likely due to both the test method as the unloading curve is steeper than the loading curve, as well as possibly damage done to the CNT surface prior to nano-indentation testing by ablating the surface. To confirm the Zwick test equipment is functioning and reading correctly to confirm this result, a load cell calibration using weights is completed, as well as comparative compression testing to a calibrated Instron system using a known silicone material sample. Both tests completed successfully, showing the Zwick system and load cell are functioning correctly and within reasonable calibration.

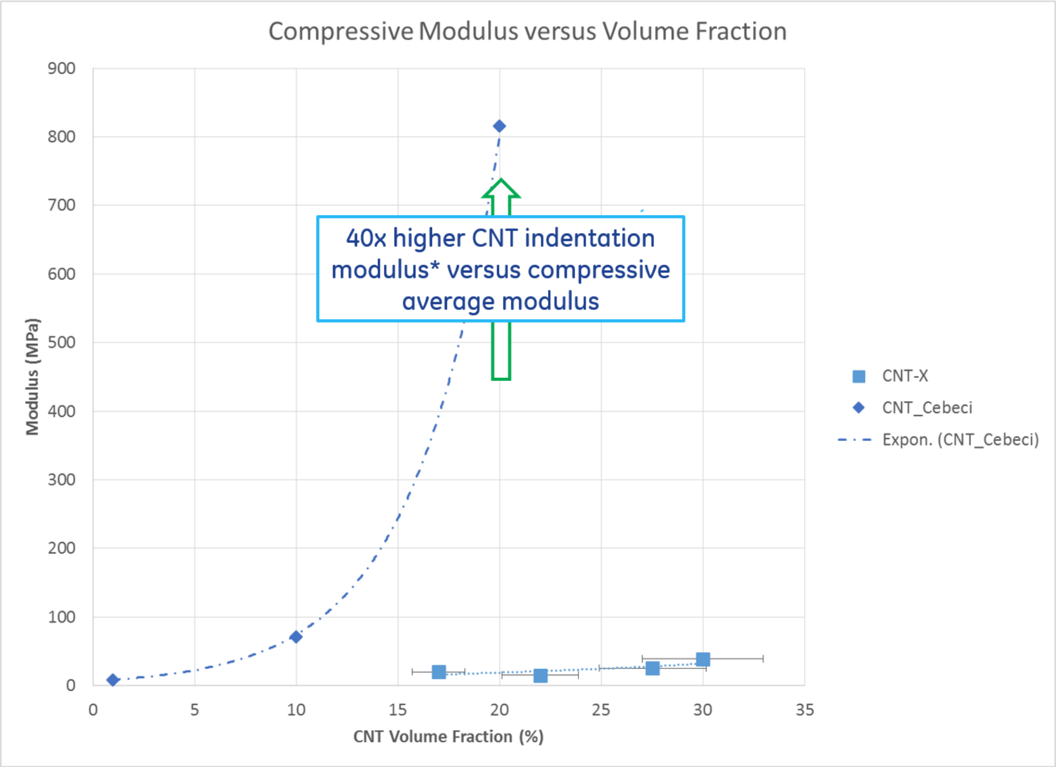

Figure 5.30: Compressive modulus versus volume fraction for various A-CNT samples using both nano-indentation as well as full scale compression testing.

Investigating the dry A-PNC samples in the two non-isotropic directions shows a very axis dependant response as expected. Figure 5.31 shows various A-PNC Vf samples in both directions, as well as one sample that was annealed at a higher temperature during the A-PNC manufacturing process. The sample annealed at 200 $^{\circ}C$ shows about a three times increase in modulus, expected due to higher Nafion crystallinity of the sample. The remainder of the discussion will focus on the 150 degree Celsius annealed samples, for a baseline comparison. The Vf error bars in Figure 5.31 are based on the assumed A-PNC size measurement accuracy of about 0.1 mm using standard calipers, which comes out between 6 and 11% error on Vfs from 10 to 40% respectively. The Young's modulus error bound is based off of the Zwick load cell stated accuracy of 1% of the measured value, a Zwick displacement accuracy of 0.2% of position, and the device area measurement accuracy as above, for up to 12% modulus error. Comparing the A-PNC devices to the pure A-CNT samples shows a clear increase in modulus, showing the stiffening effect of the Nafion on the A-CNT system. Using the rule of mixtures[76] to predict the A-PNC modulus based on the known Nafion modulus (288 MPa[53]) and the measured A-CNT forest modulus (39 MPa), for a 31% Vf device such as ID#2015011703, gives 57 MPa. This prediction does not take into account changes in Nafion crystallinity, which is estimated to be a large impact seen by this data's under prediction. The DuPont PTFE materials handbook predicts up to a five-fold increase in PTFE's modulus with increased crystallinity[77], which if assumed similar to Nafion would then predict 237 MPa for the A-PNC modulus, much closer to the measured value.

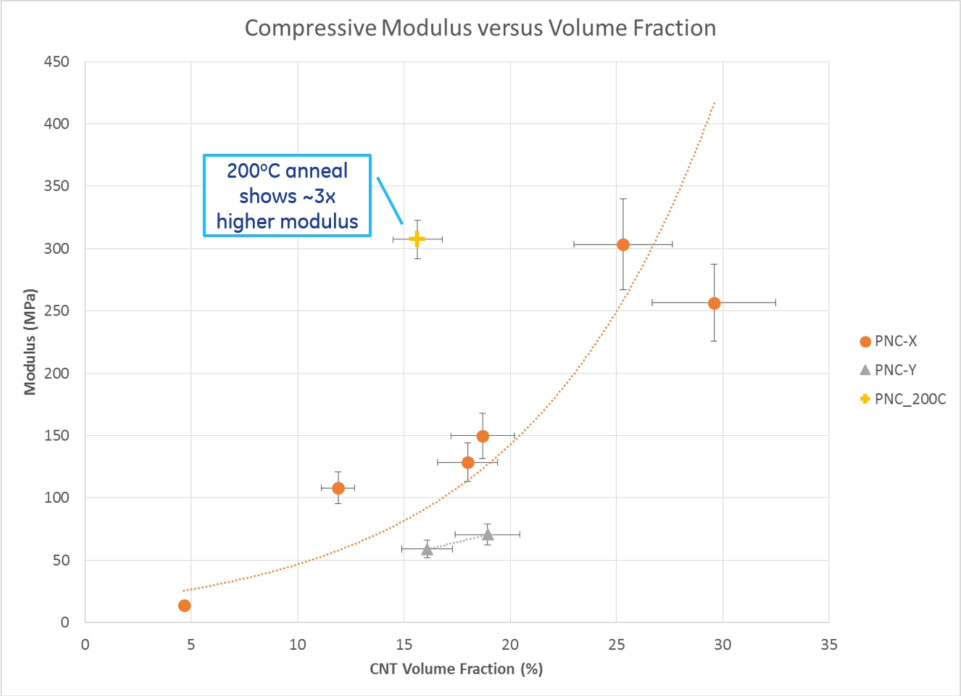

Figure 5.31: Compressive modulus versus volume fraction for A-PNC systems, in multiple non-isotropic dimensions and multiple A-PNC anneal temperatures (tested dry without IL).

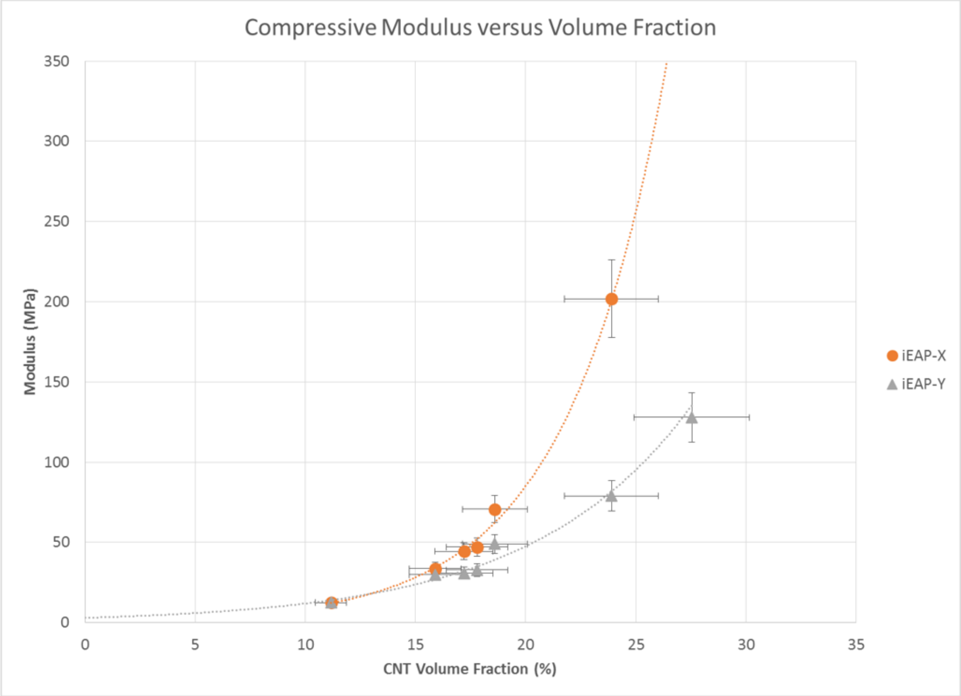

Figure 5.32: Compressive modulus versus volume fraction for EAP samples in both the x and y directions from batches 3-6.

The final i-EAP samples have been characterized on a larger scale from the three latest batches (batches three through six), utilizing both the Zwick and DIC data across varying Vf samples. All samples are infused fully with IL, are testing in ambient conditions, but have not had any voltage applied. The moisture in the air is known to create impurities in the IL showing up electrically as a reduced ECW, but this impact is assumed to have negligible impact to the material's modulus. The compressive modulus both along the CNT axis (x) and in the perpendicular axis (y) are shown in Figure 5.32, as measured from the displacement and load cell of the Zwick. The exponential regression lines for both moduli are shown in Equations 5.4 and 5.5, and define the final estimates for i-EAP electrode material's elastic moduli. These equations are based on the data available and shown in the plots, and are only valid around that range of Vfs (generally within 10-25%).

$$\mathrm{E}_x(V_f) = 1.03 * \mathrm{e}^{0.2206 * \mathrm{V_f}} \tag{5.4}$$

$$\mathrm{E}_y(V_f) = 2.97 * \mathrm{e}^{0.1388 * \mathrm{V_f}} \tag{5.5}$$

As predicted, the x axis is much stiffer than the y axis, with the ratio of the non-isotropic moduli shown in Figure 5.33. This ratio increases with increasing Vf, showing a small non-isotropy at lower Vfs, moving to over a 2.5 times stiffening at higher Vfs in the x axis. The Poisson ratio is derived by dividing the strain perpendicular to the compression direction from that of the strain in the compressed direction, as measured by the DIC imaging software. Due to the sensitive nature of this calculation and the not perfectly square samples, the Poisson ratio calculation has a lot of error when using this method. Much larger population sizes with clean cut samples will be required to complete an accurate estimate of the Poisson ratios. In addition, a method of clean cutting the sides of the samples to square the edges would need to be developed to help with the calculation consistency. Sample data for Poisson's ratio on the xy plane varied, for example, from -0.1 to 0.6 on samples ID2014080608 and ID2015011701 respectively, and on the yz plane varied from -0.05 to 0.8 on samples ID2014081504 and ID2014073002 respectively.

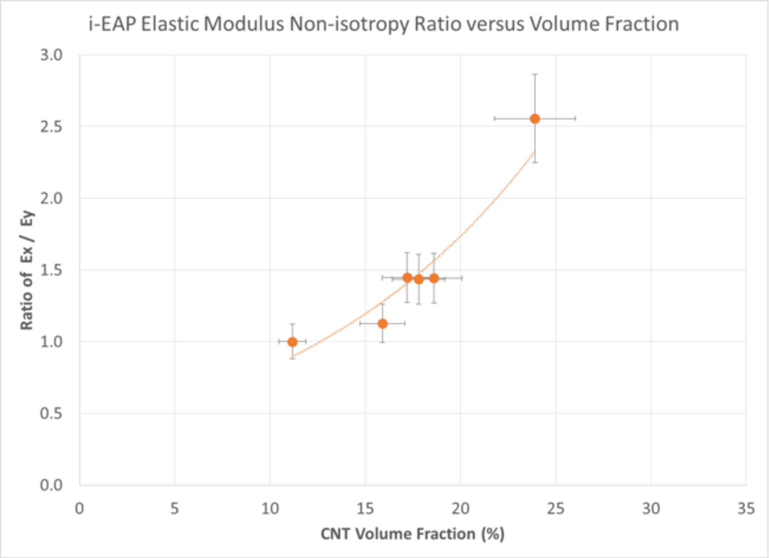

Figure 5.33: Compressive modulus non-isotropy ratio versus volume fraction for the same EAP systems as Figure 5.32, showing an increase in non-isotropy with higher Vfs.

5.3.4 Electroactive

The electroactive coupling, similar to a piezoelectric device, is analyzed by applying voltage and measuring the generated strains via DIC. The ideal test boundary conditions in defining the strain/charge device coupling include having free material boundaries with no mechanical forces applied, and uniform voltages across each electrode, similar to the electrical testing. These tests are set up to measure both AC and DC waveforms of various scan rates and voltages on two devices at a time (defined as the positive and negative electrodes). DIC is utilized as the 2D strain mapping system for a true non-invasive measurement. Again, all of this testing is completed inside the dry environment of a glove box, to ensure consistency and limit any possible device degradation. The full test setup is shown in Figure 5.34, including the VIC2D DIC computer setup on the left, the glove box with light source and microstage probe setup in the middle, and the potentiostat system on the right. Interface feed throughs have been installed into the glove box to be able to use the DIC camera as well as the potentiostat inside in the dry environment. The camera is mounted on a boom microscope stand sitting on rubber pads for vibration isolation. Two adjustable arms hold the tungsten electrodes, and microstages control their position. The same high intensity fiber optic light is aimed at the samples under test. The samples are

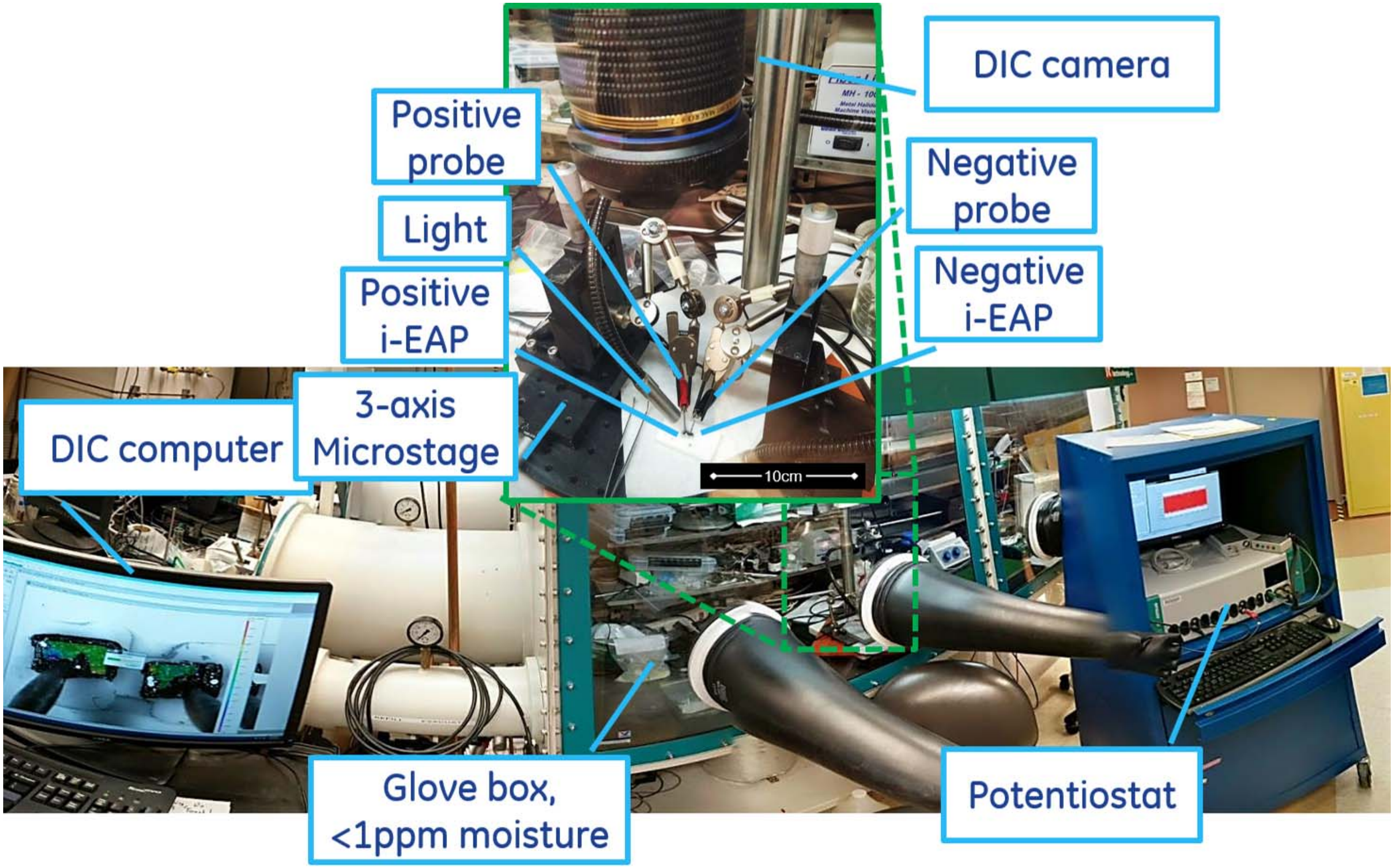

Figure 5.34: Electroactive testing setup inside controlled glove box environment, including DIC system, potentiostat and i-EAP samples. The glove box has special feed throughs for both the DIC camera's Firewire and the electrical connections for the electrodes to the potentiostat.

positioned and electrically connected in a similar manner as the cyclic voltammetry method shown in Figure 5.19. The speckle can be easily seen through the transparent IL, and the samples are in clear focus. The electrodes are positioned in the arms in a cantilevered manner in order to apply minimal force onto the samples, and are placed on the samples with just enough force to keep the samples from floating in the ionic liquid. This gives some mechanical constraint that is discussed later as a non-ideality in the experimental setup.

Initially, testing is completed on i-EAP samples without the ionic liquid, to confirm the setup is fully functional and stable, and to characterize a simpler form of an i-EAP device. A scan rate of 5 $mV/second$ is chosen to allow the actuators to fully stabilize, and the same waveform but beginning from 4 V to -4 V is used. This larger voltage allows for larger strains, but is only possible without the IL, as the IL has a reaction below 4 V and turns black, reducing the capability for DIC imaging. Figure 5.35 shows one cycle of voltage, along with the corresponding current and power as measured by the potentiostat, and the calculated charge. This data is time synced with the DIC strain data to show the strain over this same cycle.

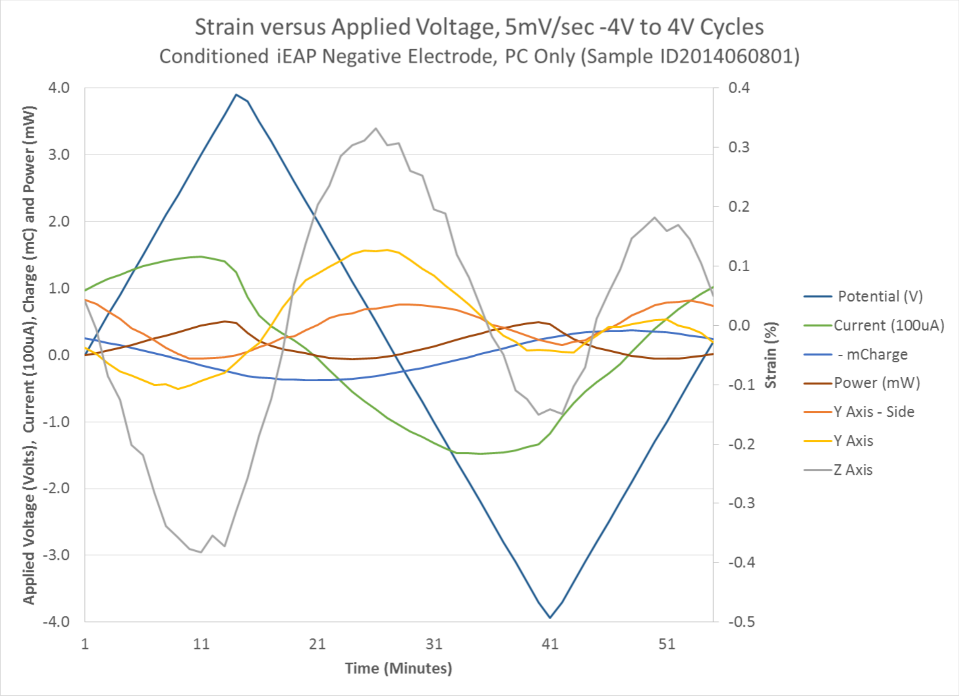

Figure 5.35: 22% Vf i-EAP device (ID2014060801) using PC solvent electroactive strain, current, charge, power and voltage versus time for one average cycle, tested with 21% Vf positive electrode ID2014062702.

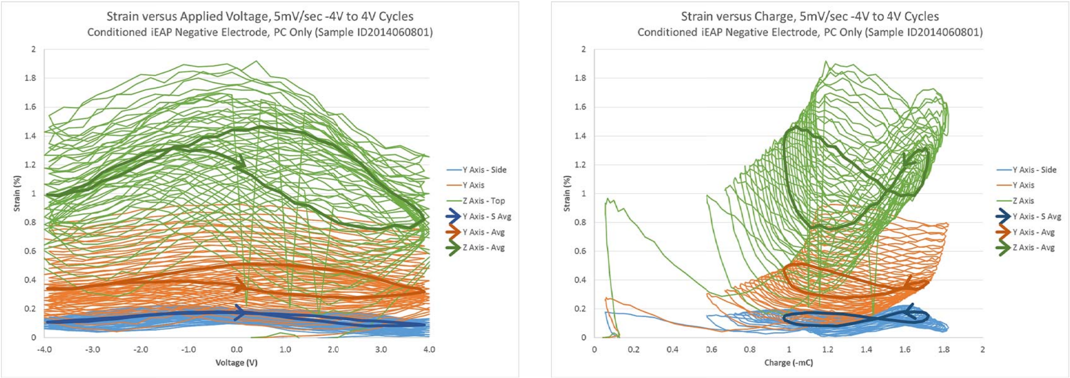

(a) Strain versus voltage for i-EAP devices. (b) Strain versus charge for i-EAP devices.

Figure 5.36: Electroactive strain versus applied voltage and accumulated charge for i-EAP devices using only the solvent propylene carbonate. The dark orange, blue and green lines are a three cycle average from the middle of the cyclic test, and the strain starts the test at zero and increases over time. This negative electrode (ID2014060801) was tested with the positive electrode ID2014062702.

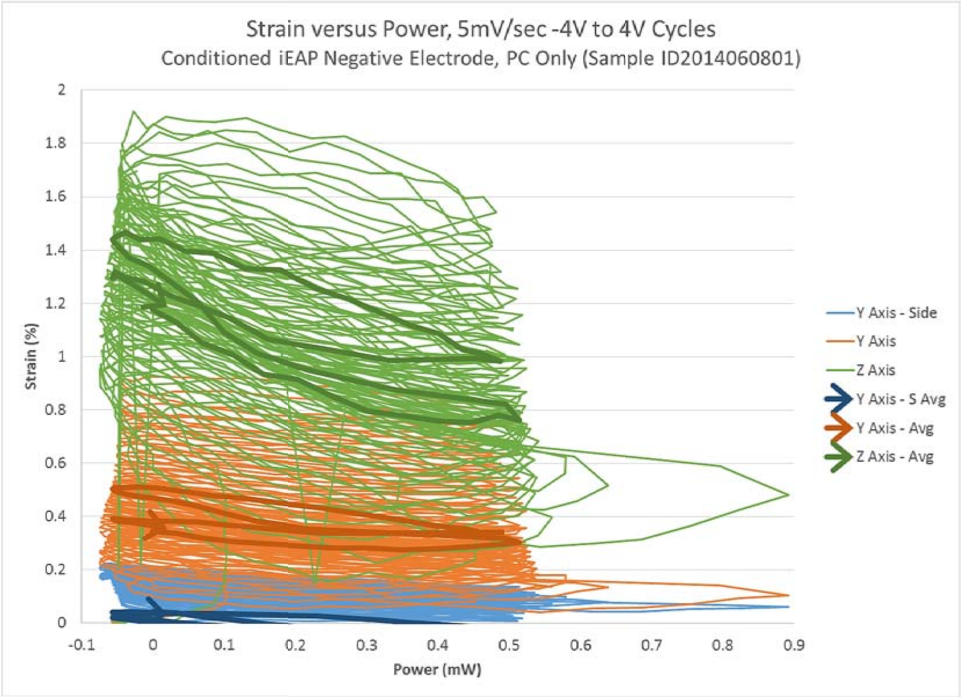

Figure 5.37: Electroactive strain versus power for i-EAP devices using only the solvent propylene carbonate. This negative electrode was tested with the positive electrode ID2014062702.

Looking at the 30 cycles, the strain is plotted versus the voltage and charge, shown in Figure 5.36. The strain cycles are not directly linear versus either voltage or charge, but there does seem to be a correlation between increasing charge and strain. The cycles have more of a figure eight shape, showing an ionic diffusion pattern that requires further investigation. The variable that correlates closest to strain, that matches the double cycle per applied voltage cycle, is power. This relationship however is still not perfect, as shown in Figure 5.37. In the z direction, the strain is seen as moving as much as ± 3,000 $microstrain$ (0.3%) across the 4 V AC waveform, whereas in the y direction it is only about ± 1,000 $microstrain$ (0.1%), even though those are expected to be equivalent. One potential difference noticed between the axes is the order in direction of densification, but this is difficult to confirm due to the lengthy manufacturing process. In general, the i-EAP devices go through a conditioning phase at the beginning of their testing, where there is very large positive strain expansion under applied voltage, but not reversible strain. This also seems to occur much more in the second axis of densification, showing the biaxial densification might not create a fully uniform Vf and spacing, and with additional stored energy in the densified forest. This is another area of recommended further study, potentially via uniaxial densification i-EAP devices or with clamped i-EAP boundary conditions.

The final i-EAP devices are tested, again in a A-PNC top crust facing down setup, with both a positive and negative electrode fully immersed in ionic liquid and spaced about two millimeters apart. Initially tested i-EAP devices from batch six utilizing 19% Vf (ID2015073103) and 27% Vf (ID2014102204) samples have shown up to ± 3,500 $microstrain$ of reversible cyclic strain. The cyclic power application for all 30 cycles is shown in Figure 5.38, with an average of three cycles in Figure 5.39. Figure 5.38 shows the device strain moving in both an alternating and slowly but unidirectionally increasing magnitude, which is a response feature of these i-EAP devices similar to the solvent only devices discussed earlier in this section. This is called the conditioning phase, and starts with each device usually straining over 1,200,000 $microstrain$ (120%), prior to generating the predominantly alternating strains needed for an actuator. The large continuously increasing strain from initiation of a new devices through to after the 30 cycles of applied voltage is visibly noticeable, shown in Figure 5.40. In addition, the strain is not exactly

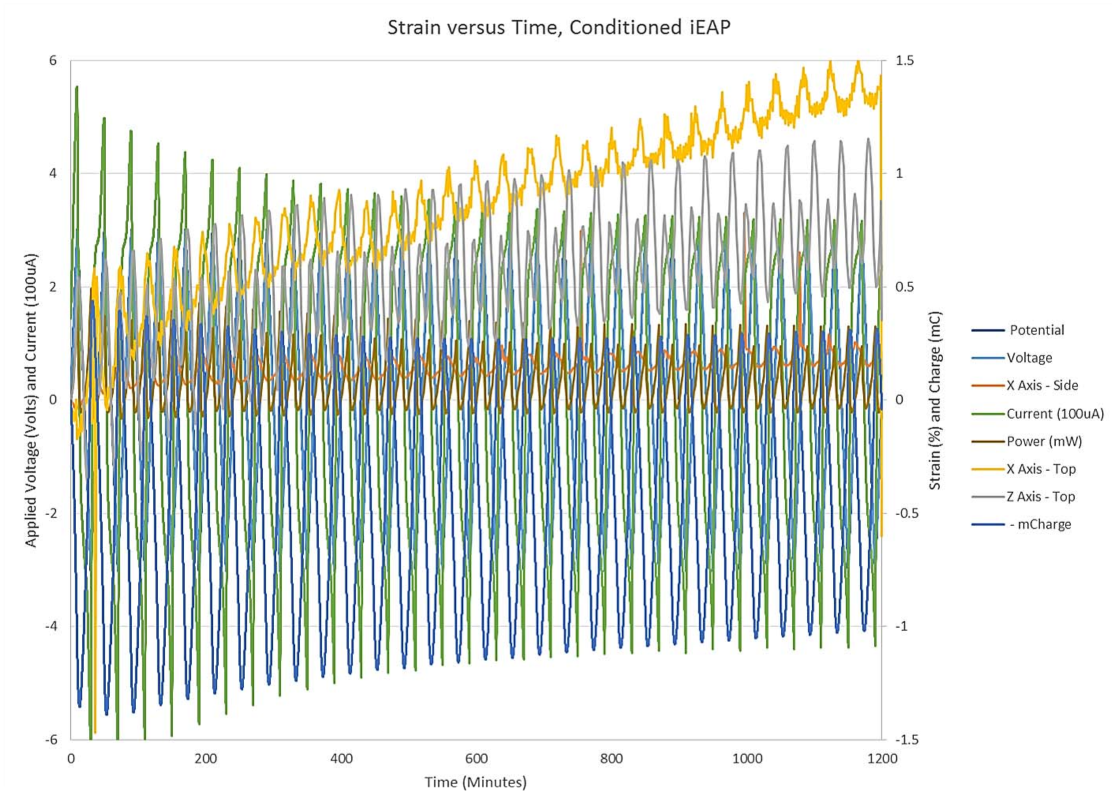

Figure 5.38: i-EAP tested under ± 3 V waveform at 5 $mV/second$, showing 30 cycles of applied voltage, measured current, calculated charge, calculated power and DIC calculated strains over time on samples ID2015073103 (19% Vf positive electrode) and ID2014102204 (27% Vf negative electrode). The stability in charge across the 30 cycles shows that the i-EAP devices are fully stabilized.

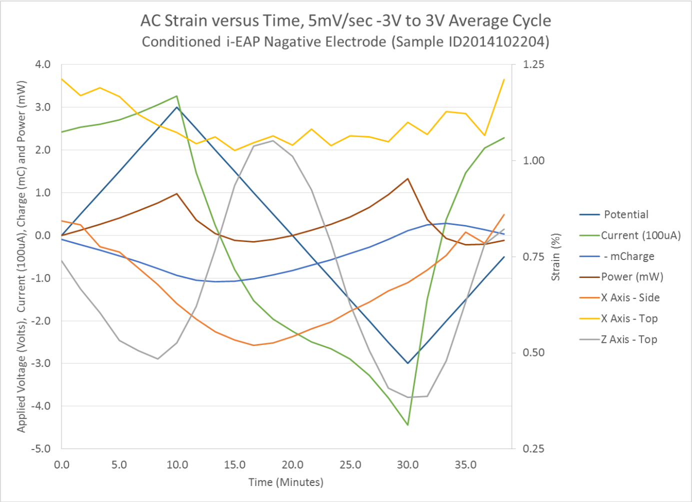

Figure 5.39: Electroactive strain versus applied voltage, current, accumulated charge and power for i-EAP device ID2014102204 (27% Vf) using IL BMI-BF4/PC.

the same in the y and z directions as would be assumed from the device symmetry. This is possibly an artifact of the two part biaxial densification, with a preferential expansion from inter CNT forces in the direction that is densified second.

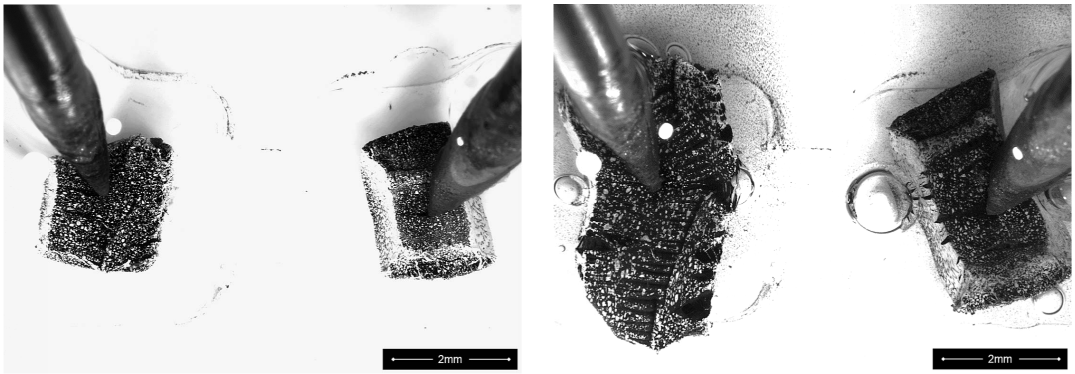

(a) Initial i-EAP devices.

(b) Conditioned i-EAP devices.

Figure 5.40: Electroactive strain conditioning with 30 applied voltage cycles, showing large and non-reversible strain greater than 120% on samples ID2015021303 (left positive electrode) and ID2015073102 (right negative electrode).

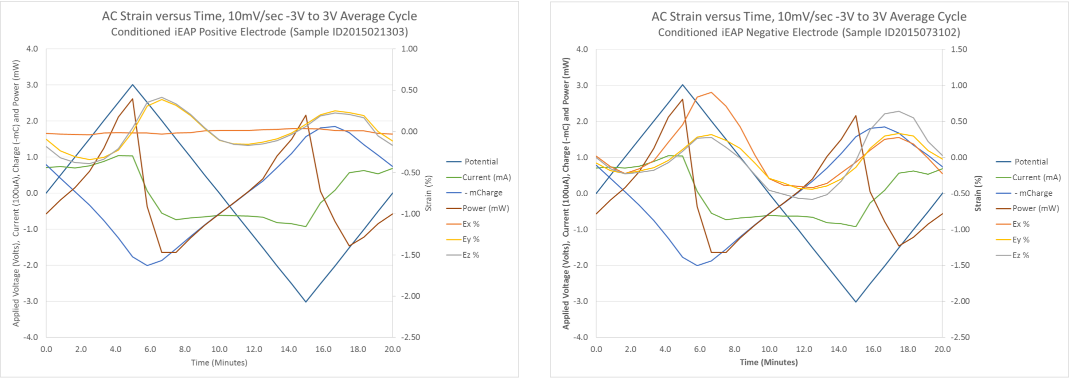

(a) Positive electrode i-EAP device.

(b) Negative electrode i-EAP device.

Figure 5.41: Strain versus applied voltage, current, accumulated charge and power for positive and negative electrode i-EAP devices using IL BMI-BF4/PC. The strain in the y and z axes are identical with a much smaller x axis strain, expected due to device symmetry.

The final i-EAP devices for characterization are from batch six, with sample ID2015021303 for the positive (left) electrode at 22% Vf, and sample ID2015073102 (right) for the negative electrode at 24% Vf. The average strain to voltage cycles in all three axis of both i-EAP electrodes are shown in Figures 5.41a and 5.41b, showing similar strain responses in the y and z directions, but with the maximum strain portions at opposite voltages for

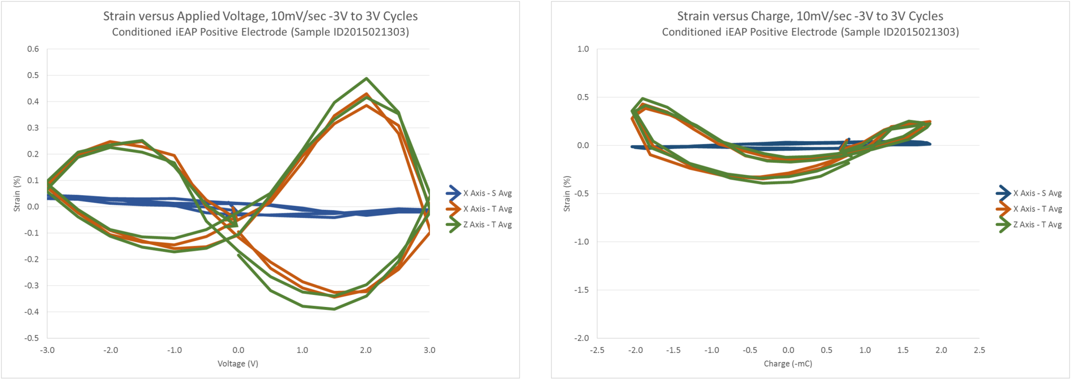

(a) Strain in three axes versus voltage applied.

(b) Strain in three axes versus accumulated charge.

Figure 5.42: Final conditioned positive i-EAP device strain in three axes versus voltage applied. Notice seemingly irregular response to voltage, but expected response to accumulated charge. This suggests the ionic distribution is in fact generating positive strain in both the positive and negative applied voltages.

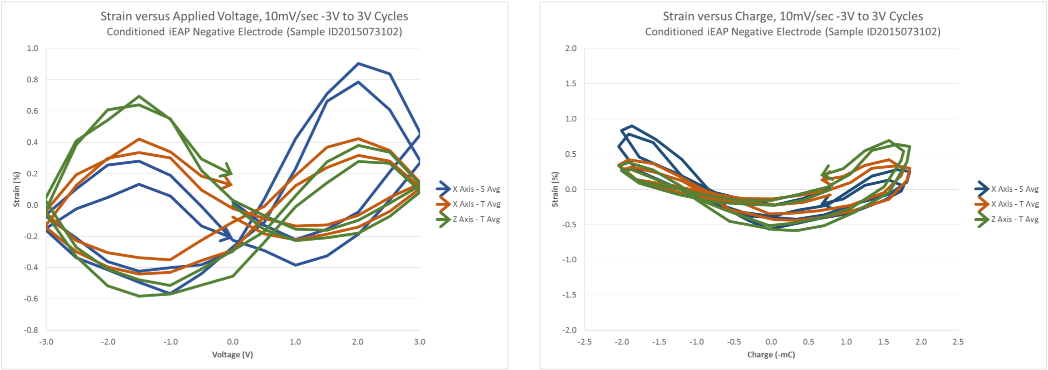

(a) Strain in three axes versus voltage applied.

(b) Strain in three axes versus accumulated charge.

Figure 5.43: Final conditioned negative i-EAP device strain in three axes versus voltage applied. The positive applied voltage creates a larger strain on this negative electrode than with the same negative applied voltage, the opposite effect to that of the positive electrode (Figure 5.42), showing the impact of the larger cation than anion. This also suggests the ionic distribution is in fact generating strain, in both the positive and negative applied voltages.

each. This is shown clearer in the strain to current relationship for the positive electrode in Figure 5.42, that the strain in the positive direction is larger than the strain in the negative direction. Figure 5.43 shows this for the negative electrode, showing the strains are larger at negative voltages. This effect is expected, as the larger positive ions (relative to negative ions in the BMI/BF4) flow to the negative electrode when it has negative voltage applied, and vice versa with the positive electrode (and relatively smaller negative ions). The strain in the opposite voltage direction is due to the movement of the smaller negative ions in the IL. This strain to charge relationship is shown in Figures 5.42b and 5.43b, showing a clear charge to strain relationship. Figure 5.42a also shows a much more similar y and z strain response of conditioned i-EAP devices (±4,130 $microstrain$ or 0.4%), and the order of magnitude smaller strain in the x direction (±420 $microstrain$ or 0.04%).

To define the coupling coefficients, a linear approximation is assumed from the maximum strain over the maximum applied voltage across the Debye length. The electric field applied is assumed to be the 3 Volts of applied voltage over the 5.15 nm Debye length, for a field of 582 MV/m. For the positive electrode sample ID2015021303, the 4,130 $microstrain$ (0.4%) in the y or z direction over this applied field yields a coupling coefficient of 7.1 $microstrain * m/MV$, or 7.1 x 10^{-12} m/V. In the x direction, with only 420 $microstrain$, this would be 7.2 x 10^{-13} m/V.

The i-EAP system has been tested in bulk form rather than as a bending actuator, not to demonstrate speed and maximum strain, but to understand the physics of actuation and the nano-structured bulk material properties and constitutive relationship. The ionic actuation mechanism is demonstrated, with an order of magnitude difference in the non-isotropic strains, and the electroactive coupling coefficients are measured.

5.4 Constitutive Model

No constitutive model exists today for a non-isotropic i-EAP device, so a linear piezoelectric model is selected for a basis of the framework. This model is chosen since it is a well understood convention in the actuator electroactive material field, and that it simply models similar electroactive coupling even though the underlying physics are different. The basic form of this model involves relating mechanical stress (T_{kl}) and strain (S_{ij}) to electric displacement (D_i) and electric fields (E_k)[78], shown in Equations 5.6 and 5.7. The matrices for the electrical (ε_{ik}), electroactive (d_{ikl}) and mechanical (s_{ijkl}) tensors as derived for a Triclinic system are shown in Equations 5.8, 5.9 and 5.10 respectively[78]. The electrical tensor assumes constant stress and the compliance tensor assumes constant electric field. These tensors are based on the least symmetric Triclinic piezoelectric system, with a possible 21, 18, and 6 independent elastic, piezoelectric, and dielectric constants, respectively[78]. Since the coupling methods are different in electroactive polymer materials versus piezoelectric materials, not assuming any symmetry at this point confirms that this model should still be applicable, without generating any errant assumptions.

$$\mathrm{S_{ij}} = \mathrm{s_{ijkl}T_{kl}} + \mathrm{d_{kij}E_k} \tag{5.6}$$

$$\mathrm{D_i} = \mathrm{d_{ikl}T_{kl}} + \varepsilon_{\mathrm{ik}}\mathrm{E_k} \tag{5.7}$$

$$\varepsilon_{ik} = \begin{bmatrix} \varepsilon_{11} & \varepsilon_{12} & \varepsilon_{13} \\ \varepsilon_{12} & \varepsilon_{22} & \varepsilon_{23} \\ \varepsilon_{13} & \varepsilon_{23} & \varepsilon_{33} \end{bmatrix}, \tag{5.8}$$

$$d_{ikl} = \begin{bmatrix} d_{111} & d_{122} & d_{133} & d_{123} & d_{113} & d_{112} \\ d_{211} & d_{222} & d_{233} & d_{223} & d_{213} & d_{212} \\ d_{311} & d_{322} & d_{333} & d_{323} & d_{313} & d_{312} \end{bmatrix}, \tag{5.9}$$

$$s_{ijkl} = \begin{bmatrix} s_{1111} & s_{1122} & s_{1133} & 2s_{1123} & 2s_{1113} & 2s_{1112} \\ s_{1122} & s_{2222} & s_{2233} & 2s_{2223} & 2s_{2213} & 2s_{2212} \\ s_{1133} & s_{2233} & s_{3333} & 2s_{3323} & 2s_{3313} & 2s_{3312} \\ s_{1123} & s_{2223} & s_{3323} & 2s_{2323} & 2s_{1323} & 2s_{1223} \\ s_{1113} & s_{2213} & s_{3313} & 2s_{1323} & 2s_{1313} & 2s_{1213} \\ s_{1112} & s_{2212} & s_{3312} & 2s_{1223} & 2s_{1213} & 2s_{1212} \end{bmatrix}. \tag{5.10}$$

5.4.1 Model Derivation

Due to the tetragonal symmetry of the A-CNT system, the final i-EAP device is assumed to display similar symmetries. With the 1-, 2-, and 3-directions aligned with x-, y-, and z-directions in Figure 5.1, a standard tetragonal system from piezoelectric materials is assumed for both the electrical and mechanical tensors[78]. This tetragonal system however is expected to differ in the electroactive tensor from the known crystal symmetries for piezoelectrics (4, 422, 4mm, etc[78]), since the material is conductive, and strains in all three dimensions with applied voltage in any dimension, without any expected coupled shear strain components. Therefore, $\varepsilon_{12} = \varepsilon_{13} = \varepsilon_{23} = \varepsilon_{21} = \varepsilon_{31} = \varepsilon_{32} = 0$, $d_{123} = d_{113} = d_{112} = d_{223} = d_{213} = d_{212} = d_{323} = d_{313} = d_{312} = 0$, and $s_{2311} = s_{1311} = s_{1211} = s_{2322} = s_{1322} = s_{1222} = s_{2333} = s_{1333} = s_{1233} = s_{1323} = s_{1223} = s_{1213} = 0$. The relevant simplified tensor matrices are shown in Equations 5.11, 5.12 and 5.13.

$$\varepsilon_{ik} = \begin{bmatrix} \varepsilon_{11} & 0 & 0 \\ 0 & \varepsilon_{22} & 0 \\ 0 & 0 & \varepsilon_{33} \end{bmatrix}, \tag{5.11}$$

$$d_{ikl} = \begin{bmatrix} d_{111} & d_{122} & d_{133} & 0 & 0 & 0 \\ d_{211} & d_{222} & d_{233} & 0 & 0 & 0 \\ d_{311} & d_{322} & d_{333} & 0 & 0 & 0 \end{bmatrix}, \tag{5.12}$$

$$s_{ijkl} = \begin{bmatrix} s_{1111} & s_{1122} & s_{1133} & 0 & 0 & 0 \\ s_{1122} & s_{2222} & s_{2233} & 0 & 0 & 0 \\ s_{1133} & s_{2233} & s_{3333} & 0 & 0 & 0 \\ 0 & 0 & 0 & 2s_{2323} & 0 & 0 \\ 0 & 0 & 0 & 0 & 2s_{1313} & 0 \\ 0 & 0 & 0 & 0 & 0 & 2s_{1212} \end{bmatrix}. \tag{5.13}$$

The engineering matrices are shown in Equations 5.14, 5.15 and 5.16, and are based on the i-EAP axis defined with the long axis of the A-CNTs as the x direction (see axis definition in Figure 5.1). This assumes tetragonal A-CNT mechanics, the electroactive response seen from experimentation where the i-EAP strains in all three dimensions with a single applied voltage, and isotropy in the y-z plane. In addition to the simplifications from the constitutive elements that are zero, many additional parameters are assumed equal. In particular, since the y and z dimensions are equivalent, $\varepsilon_{22} = \varepsilon_{33}$ and the standard tetragonal assumptions apply to the compliance tensor ($s_{2222} = s_{3333}, s_{1313} = s_{1212}, s_{1122} = s_{1133}, etc$). Also, due to the conductive nature of the CNT based i-EAP, the electroactive parameters are assumed constant versus the direction of applied voltage, or $d_{1kl} = d_{2kl} = d_{3kl}$.

$$\varepsilon_{ik} = \begin{bmatrix} \varepsilon_x & 0 & 0 \\ 0 & \varepsilon_y & 0 \\ 0 & 0 & \varepsilon_y \end{bmatrix}, \tag{5.14}$$

$$d_{ikl} = \begin{bmatrix} d_x & d_y & d_y & 0 & 0 & 0 \\ d_x & d_y & d_y & 0 & 0 & 0 \\ d_x & d_y & d_y & 0 & 0 & 0 \end{bmatrix}, \tag{5.15}$$

$$s_{ijkl} = \begin{bmatrix} \frac{1}{E_x} & \frac{-\nu_{xy}}{E_x} & \frac{-\nu_{xy}}{E_x} & 0 & 0 & 0 \\ \frac{-\nu_{xy}}{E_x} & \frac{1}{E_y} & \frac{-\nu_{yz}}{E_y} & 0 & 0 & 0 \\ \frac{-\nu_{xy}}{E_x} & \frac{-\nu_{yz}}{E_y} & \frac{1}{E_y} & 0 & 0 & 0 \\ 0 & 0 & 0 & \frac{(1+\nu_{yz})}{E_y} & 0 & 0 \\ 0 & 0 & 0 & 0 & \frac{1}{2G_{xy}} & 0 \\ 0 & 0 & 0 & 0 & 0 & \frac{1}{2G_{xy}} \end{bmatrix}. \tag{5.16}$$

These matrices complete the full linear and time invariant constitutive model of the i-EAP material based on A-CNTs, whose nine independent constants can be partially defined based on the testing completed in the prior sections of chapter 5. This new model is based on standard mechanical and electrical models, but shows a new type of electroactive coupling different than known piezoelectric crystal models, due to the conductive nature of the active material that does not allow for the electrical field to be defined with a global direction.

5.4.2 Ionic Electroactive Polymer Device Constitutive Model

The i-EAP material's constitutive model can be arranged from Equations 5.6 and 5.7, with the tensor parameters described in Equations 5.14 through 5.16, and data as measured in earlier sections. The final nine derived independent coefficients are shown in Table 5.5 for a $\sim$20% Vf i-EAP device material, derived from i-EAP positive electrodes with the ionic liquid BMI-BM4/PC and -3 V to 3 V applied waveforms. The elastic moduli in both directions are calculated from Equations 5.4 and 5.5 at a 20% Vf from a regression of multiple samples, where as the permittivity and electroactive coupling are from the positive electrode device ID2015021303 from the last batch (six) tested at 5 $mV/second$.

Table 5.5: 20% i-EAP device constitutive model coefficients.

Parameter	i-EAP 20%Vf
ε_x	7 x 10^{-10} F/m
ε_y	7 x 10^{-10} F/m
d_x	7.2 x 10^{-13} m/V
d_y	7.1 x 10^{-12} m/V
E_x	84.9 MPa
E_y	47.7 MPa
G_{xy}	$(FutureWork)$
ν_{xy}	$(FutureWork)$
ν_{yz}	$(FutureWork)$

As this is a new constitutive model for a relatively new class of nanocomposite materials, there is no similar prior work that can be used for a full direct comparison. These A-CNT based i-EAP composite materials have a slightly lower modulus than predicted using the rule of mixtures, as discussed in Section 5.3, but show similar relationships as other experimentally measured polymeric PNC devices such as A-CNT and PDMS PNCs, which measure ~8 and ~1 MPa, respectively[43]. This is also in range of the Nafion wetted with IL measured to be 50 MPa[10]. The measured moduli for the i-EAP materials is slightly lower than the dry A-PNC, showing the effect of the IL on the i-EAP's stiffness. The effective relative permittivity measured of ~79 is in range with other electroactive dielectric materials, with quartz at ~40[78] and Rochelle Salt between 1,100 and 9 in two different axes[79]. The electroactive coupling is a little larger than piezoelectric crystals in the y direction (d_{111} of quartz is $\sim$ 2.3 x 10^{-12} m/V or 2.3 pC/N[79]), due to the larger strains achieved in i-EAP materials under much lower voltages. This is not the largest coupling measured, likely due to the lower moduli. Piezoelectric materials such as Rochelle Salt have shown a larger d_{123} piezoelectric coefficient of ~2 x 10^{-9} m/V. This relative performance of electroactive coupling meets expectations for an electroactive device with a much lower modulus (compared to a piezoelectric such as quartz with a modulus ~80 GPa[78]), which in future work could be tailored for energy density using different anneal temperatures on the PNC.

These coefficients constitute the first assembly of mechanical, electrical and electroactive properties into a constitutive relation for an active nano-structured material. This model is the culmination of a large effort to reliably manufacture and tailor CNT growth, A-PNC creation and i-EAP system actuation, for various Nafion and A-CNT based systems. This model is a linear approximation, at a 0.0008 Hz cyclic rate over 3 V, with known limitations. Extension to other volume fractions and combinations are planned, and suggestions for future work are discussed in the next section.

Chapter 6

Conclusions and Recommendations

Not only has the CVD A-CNT growth process been tailored for high quality and enhanced production, but active i-EAP devices have been demonstrated with larger strains, cyclic capability and characterized to provide the first constitutive model of an active nano-structured material. The constitutive model in Section 5.4 constitutes the first assembly of mechanical, electrical and electroactive properties into a constitutive relation for an active nano-structured material, and is the culmination of growing 370 A-CNT samples for creating over 80 manufactured A-PNC or i-EAP samples. This chapter will detail many of the limitations eluded to in previous chapters, and recommend future studies to better understand the A-CNT and i-EAP systems.

6.1 Aligned Carbon Nanotube Contributions

This thesis shows that with certain levels of quality control, analysis and investigation, A-CNT processing can become a stable and repeatable process primed for scaling up quickly into larger production, distributions and usage. With the easy availability of good quality A-CNT materials, this strong and lightweight material can become cheaper and easier to integrate into high strength to weight systems.

With the CVD processing of wafer substrates with iron catalyst at 800 $^{\circ}C$ with 500 ppm water, and the correct amount of helium, hydrogen and ethylene as defined in Chapter 4, over 2 micrometers of A-CNT in length can be produced per second in a theoretically continuous process (such continuous production with an earlier recipe has already been demonstrated[80]. Taking the original process and stabilizing the thermal profiles, adding water control and minimizing changes to the setup of the system have enhanced the CVD growth towards a very high yield process. This tailored processing has also allowed for much taller growth heights, with samples over 6 *mm* tall demonstrated so far. The sample delamination from the silicon wafer substrates and biaxial densification is also improved, for creating various morphologies of A-CNTs that are useful in a variety of materials. These materials have been characterized across varying Vfs for height, CNT quality, morphology, CNT dimensions and modulus, to show this new processing has not modified or harmed the base A-CNT materials in any way. These A-CNTs are also the basis of the remainder of the A-PNC and i-EAP devices in this thesis, along with multiple other A-PNC materials in other parallel necstlab research projects.

6.2 Ionic Electroactive Polymer Device Contributions

Continuing on the prior work in collaboration with PSU, unconstrained thickness actuator devices have shown complexities in processing, usage and characterization, but continue to show promise as a future low cost, light weight, low working voltage and high strain actuator material. The material's high porosity adds to the low density aspect of the material, and is theorized to increase actuation speeds due to the larger continuous ions paths available. With adequate conditioning and constraints, these devices have been shown to exhibit extremely large strains, which have not fully been replicated in this work using unconstrained devices. This shows the criticality of the system's boundary conditions to the effectiveness of the material, and could be a subject for future research and modeling.

Methods of fully characterizing i-EAP devices are described in this work, and devices are characterized for various morphologies. Morphological, material constituents, mechanical, electrical and electroactive properties of A-PNC and i-EAP materials are shown in Chapter 5, and lead to a first ever improved non-isotropic constitutive model of this electrode material. TEM, SEM, TGA, cyclic voltammetry, compressive mechanical testing and DIC imaging show the detailed quality and properties of the materials, and can help lead to a final model of the full constitutive relations. Working with these strained devices also has emphasized some of the densification irregularities in Vf usually seen in SEMs, which shows a preferential expansion in the direction of the second densification direction, as discussed in Section 5.3. This proves the densification is not truly a symmetric biaxial densification even with symmetric final dimensions, and this result could be leveraged by composite A-PNC studies to help improve understanding of the materials by forcing consideration of inhomogeneity. This work is the basis for understanding the bending actuator devices with the electrodes fabricated from the same i-EAP electrode material, and brings a better understanding to the strain and material properties of the electrodes and devices.

6.3 Recommended Further Research

6.3.1 Material and Device Processing Techniques

In addition to the work completed in this thesis on the tailoring and process control of A-CNT CVD growth, there are still many areas of study in the creation of various specific quality CNTs, faster growth rates, and the understanding of important process variables. On the A-CNT CVD system, the water is now controlled through a computer controlled mass flow controller, but its environment is still variable. Keeping the water temperature consistent will further stabilize the moisture saturation into the helium gas flow, and thus further decrease moisture variability inside the furnace. Also, a system to keep the CVD tube pressure constant would potentially lead to more consistent growth conditions. Lastly on the furnace setup, a good routine of calibration on the flow controllers will reduce long term variation. For higher confidence of the measurements and data in this work, replicates of this work using larger sample sizes should be completed.

The A-CNT forests were characterized in this work using many various techniques, but despite the sophistication of these techniques, there was still some uncertainty in the processing and forest morphology. For example, sample size limitations didn't allow for a statistically defined CNT characterization. To resolve the issue, collecting and working with larger data sets is recommended for future work to help reduce this uncertainty. In addition, the CNT waviness and CNT-to-CNT spacings were only compared using microscopy to prior work and were not numerically quantified, a technique which is recommended for follow-on work.

Further studies on enhancing A-CNT heights through varying the gas flow rates and thermal profiles are out of scope in this work, but would be expected to further increase the growth height per minute. Chapter 5 shows that changing the catalyst ripening time has a large effect on the growth height, and in trending this data it seems there might be a maximum peak in between the original thermal profile shown in Figure 5.2a and the new thermal profile shown in Figure 5.2b, at somewhere between 18 and 19.5 minutes. In addition, in some later growths the ethylene flow controller became low out of calibration, and this effected the heights of the samples ($\sim$20% reduction in gas flow reduced A-CNT heights by $\sim$20%). This could mean that additional ethylene might provide the hydrocarbons needed for even faster growth. This could also be modeled along with the gas flows in the CVD furnace using CFD to estimate correct levels for different growth adjectives. In addition, it has been theorized that high quality A-CNT materials might not be desirable for active devices such as these i-EAP actuators, as the additional quantity of defects and amorphous carbon would create higher surface area devices. This would be a very interesting study, possibly by varying the growth properties but keeping the height and morphology similar.

One process change possible for the i-EAP device creation in particular is a multiple infusion in order to created higher Nafion densities. It is not known whether additional infusions will add thicker layers to the CNTs, or if they will just add additional Nafion particles, but a higher level of Nafion is expected to allow increased ions at each electrode and create larger strains across the device. Also, it was found that the solvent, PC, has been slowly evaporating from the IL in the i-EAP test devices. To minimize the impact of changing viscosities during the testing, the IL is replaced between each test. However, the evaporation of the solvent was not an expected effect since the vapor pressure of PC is far below ambient conditions[60]. Future research should investigate the IL mixture to understand its exact properties as compared to literature-based estimates from mixtures.

6.3.2 Recommended Property Studies

In developing enhanced A-CNT growth, as well as during manufacturing and testing i-EAP devices, many additional topics for discussion and study have emerged. The basic constitutive properties are laid out here as a foundation for future work on high strain low voltage actuators, but substantial future work is required before commercial products will be ready. In addition, more detailed data collection and reduction can further the constitutive relation to define both the shear modulus, dielectric properties and non-linear and time based relationships. Many studies on i-EAP devices have looked at varying the conducting materials, thicknesses and ILs, but there are still many unknowns even in those areas. In particular, alternate ILs using alternate solvents could yield higher strains, and allow for longer term working devices without the need for high purity dry liquids and evaporation issues. One example of another solvent for the IL being researched is Dichloromethane[58]. The i-EAP materials also have only been tested over very few cycles, and only at room temperature. A better understanding of the degradation over time and temperature would also provide a better understanding of the long term benefits of these materials. Testing thinner devices would also allow for much faster actuation, from the diffusion based on the square of the ion transport distance.

Another variable for tailoring the i-EAP device properties is the degree of Nafion crystallinity, which was held constant in this work. By modifying the anneal temperature, the Nafion crystallinity can be altered to vary the force to strain relationship of the actuators. This also could have a side effect of modifying the Nafion morphology in the A-PNC, which could further change the constitutive properties. By monitoring these changes over anneal temperatures, optimized devices could be created with larger and faster strains and higher specific energy densities. In addition, the potential Nafion and CNT interaction that has created the hexagonal Nafion formations (see Figure 5.16 and associated discussion) is not well understood. Future investigation using X-ray diffraction would define the crystallinity of the Nafion to show if it is an unexpected form in this temperature and pressure of formation.

Along with the Nafion crystallinity, the underlying method of strain is still not fully understood. Follow-on work in defining the method of electroactive strain and actuation would be beneficial to allow for these control methods, likely including finite element analysis of the CNT and Nafion network structure. This also might help to explain the conditioning requirements on the materials, and even potentially the non-isotropic strains in the two equivalent axes. Looking further into the ion distributions during actuation such as done in Liu et al.[26] might also assist with defining the strain method, using Time-of-Flight Secondary Ion Mass Spectrometry (TOFF-ISMS). This could be applied to these devices during different stages of actuation to assist with understanding of the strain mechanisms.

New devices could also be manufactured using coatings, doping, or inclusion of additional composite constituents to optimize strain and energy densities. Prior work has shown it is possible to use a low temperature oCVD process to coat the A-CNT forests in controllable, thin, conformal polymer layers[47]. Conformal CNT coating with a non-conducting polymer such as divinylbenzene (DVB) has been tested with initiated chemical vapor deposition (iCVD), as it is expected to add an insulating layer to the CNT arrays, and allow for increased working voltages and thus larger actuation forces and displacements. Unfortunately DVB insulating coatings have not been successful in creating larger electrochemical windows in testing so far. Different thickness conformal coatings could be attempted to break through this roadblock.

The studies described here follow from the contributions of this work, and provide a path to understanding and optimizing the A-CNT and i-EAP electrode materials. This understanding could better help to mature devices from actuators to energy harvesters to supercapacitors, in fields as wide as health care, aerospace and consumer goods. This work has shown the detailed manufacturing processes and enhancements for creating i-EAP bulk actuators based on A-CNT systems, and the potential for a high yield and cost effective production. In addition, the A-CNT, A-PNC and i-EAP materials have been characterized in detail for the quality, morphology, constituents, mechanical properties, electrical properties and electroactive properties in true unconstrained and moisture free conditions, which has not been completed to date. The low voltage and high strain properties have been evident through the full derived constitutive relation of the materials, proving the great and long term potential for these devices to be used as effective sensors and actuators.

Appendix A

Final A-CNT Growth Procedure and Recipe

This A-CNT CVD process is defined for the 1 inch furnace setup in the necstlab at MIT, in building 35. The standard setup requirements are listed below:

- Positions: Loaded at -2, 0, 2, and 4 (4 optional, will be 50-80 μm shorter)
- Growth Time: 7.5 min
- Delam Time: 2 min
- Water (from 600 $^\circ C$ until delam): 0.7 bubbles per second, about 0.5 *sccm* He bubbled through 21 $^\circ C$ DI water
- Use ceramic insulator caps, make sure furnace is inside green taped lines, and the quartz growth tube is positioned axially in the furnace all the way to the right until it is close to the fume hood wall
- Open furnace at end of delam immediately
- Includes temperature ramp settling time
- Use seasoned 1 inch quartz tube. Seasoning is completed using multiple sacrificial growths prior to actual growths
- Bake tube when completed for the day, as well as at least after every 3 growths.
- Check calibration of MFC controllers frequently
- Growth Recipe: 2014_BLD35_optimumdoug_7_5mH2O_2EZD.txt, below

This recipe is written in the Ansari natural language code.

Growth Recipe, 2014_BLD35_optimumdoug_7_5mH2O_2EZD.txt

```
’2014_BLD35_optimumdoug_7_5mH2O_2EZD
’based on 2013nw14_pattern50percentHeH_75percentC2H4_12.5growth
’Doug Jacobs 9/11/2015
’From Alex 8/5/2013, stabilize H2 ramp, added delam, added water (MFC), shortened growth
’Renamed for move to building 35-417, 10/8/2014
’Shortened delam, 8/7/2015

’ Cleaning the lines (feel free to skip after first growth of day)
turn log on
set helium to 254 sccm
set hydrogen to 475 sccm
set ethylene to 295 sccm
set water to 30 sccm
turn helium on
turn hydrogen on
turn ethylene on
turn water on
wait for 0.3 min
turn ethylene off
turn hydrogen off
turn water off
wait for 0.1 min
turn helium off

’ Cleaning the tube
set helium to 1000 sccm
turn helium on
wait for 4 min
set hydrogen to 200 sccm
turn hydrogen on
```

```
’ Ramp to temperature, please turn on 0.7 bubble per second of water at ~600C (~0.01scfh)
set helium to 37 sccm
set zone 1 to 200 deg C
set zone 2 to 200 deg C
turn zone 1 on
turn zone 2 on
wait for 4.5 minutes
wait until zone 1 temperature > 199 deg C
set zone 1 to 740 deg C
set zone 2 to 800 deg C
turn zone 1 on
turn zone 2 on
wait until zone 1 temperature > 600 deg C
set water to 5.4 sccm
turn water on
wait until zone 1 temperature > 738 deg C
wait for 5 min

’ Growing CNTs
set ethylene to 150 sccm
turn ethylene on
wait for 7 minutes
turn ethylene off
turn zone 2 off

’Delamination Process, turn off water
set hydrogen to 250 sccm
turn water off
email dougsj@mit.edu with a message saying “time to open lid”
wait 2 minutes

’ Shut down, please immediately open lid
turn hydrogen off
turn zone 1 off
set helium to 1000 sccm
wait 10 minutes
```

set helium to 100 sccm

wait until zone 1 temperature $<$ 180 deg C

turn helium off

email dougsj@mit.edu with a message saying “CNT Growth Completed”

turn log off

Appendix B

Full Summary of Devices Manufactured

Each device manufactured is given an ID number at the CVD growth stage, based on the date of growth and how many samples are grown in a given day. The device is a single i-EAP electrode, based on a single A-CNT growth. Along the way dimensions, weights and other information is captured, until the device is complete as an i-EAP for testing including ionic liquid. Figure B.2 contains the final three batches of devices manufactured, that this work is based on. The columns and units are defined in Table B.1. Blank cells are generally devices that were not fully utilized or not manufactured into i-EAPs.

Table B.1: Definition of sample data list columns.

Name	Description	Units
Batch	Batch PNC manufactured	N/A
ID	Sample ID number based on year, month, day	NA
CNT	As-grown mass of A-CNT	*mg*
CNT Vf	Vf of A-CNT after densification	%
Nafion	Mass of Nafion infused into PNC	*mg*
PNC	Mass of PNC	*mg*
Anneal T	Temperature during Nafion anneal process	$^{\circ}C$
Z Post	Width of PNC sample	*mm*
Y Post	Length of PNC sample	*mm*
X	Height of PNC sample	*mm*
Volume	Volume of PNC sample	mm^3
CNT Vf Post	Vf of A-CNT post Nafion infusion	%
Expansion	Vf expansion during Nafion infusion	%
IL	Mass of IL infused into PNC	*mg*
IL Vf	Vf of PNC filled with IL	*mg*

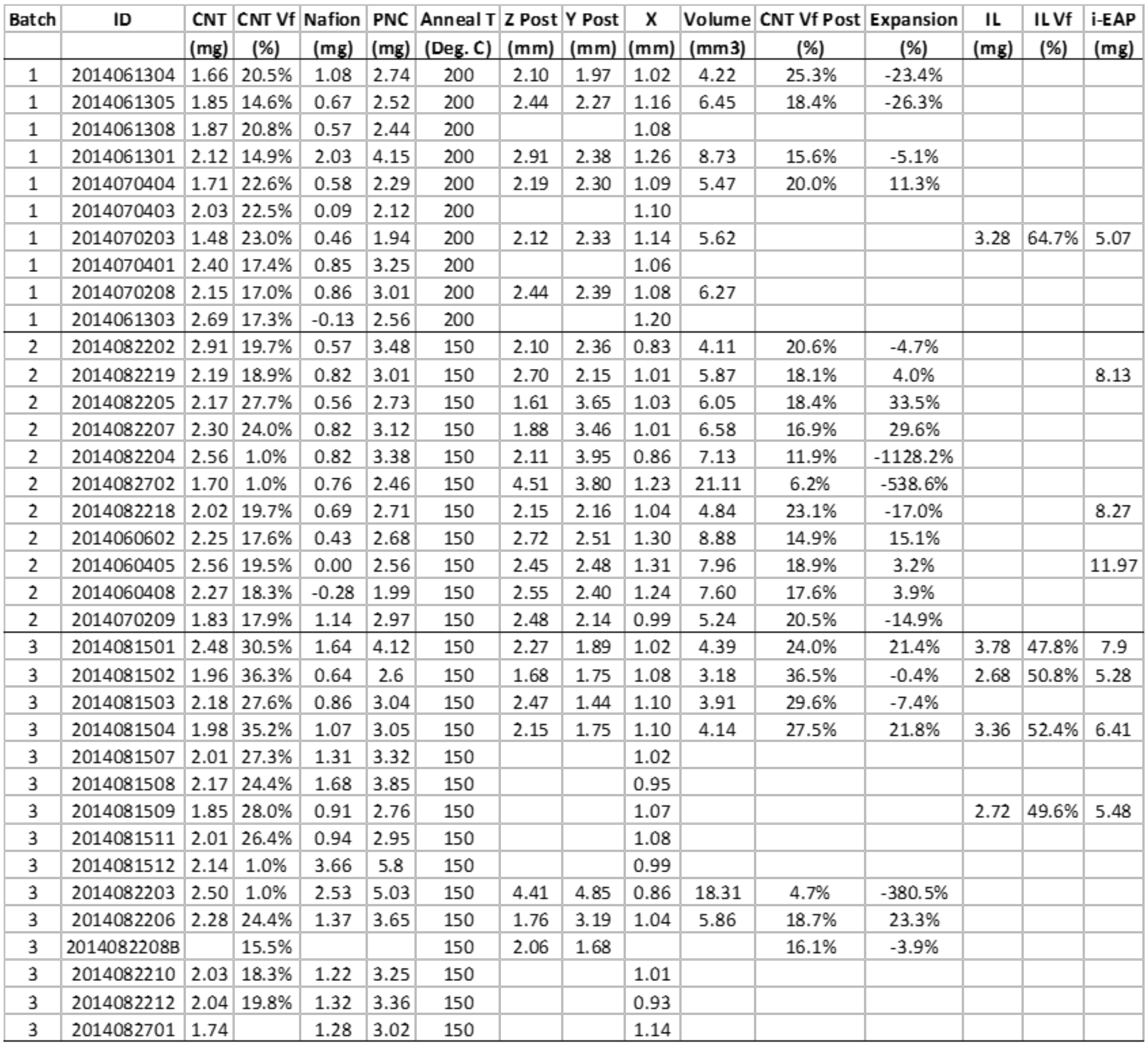

Batch	ID	CNT	CNT Vf	Nafion	PNC	Anneal T	Z Post	Y Post	X	Volume	CNT Vf Post	Expansion	IL	IL Vf	i-EAP
		(mg)	(%)	(mg)	(mg)	(Deg. C)	(mm)	(mm)	(mm)	(mm3)	(%)	(%)	(mg)	(%)	(mg)
1	2014061304	1.66	20.5%	1.08	2.74	200	2.10	1.97	1.02	4.22	25.3%	-23.4%			
1	2014061305	1.85	14.6%	0.67	2.52	200	2.44	2.27	1.16	6.45	18.4%	-26.3%			
1	2014061308	1.87	20.8%	0.57	2.44	200			1.08						
1	2014061301	2.12	14.9%	2.03	4.15	200	2.91	2.38	1.26	8.73	15.6%	-5.1%			
1	2014070404	1.71	22.6%	0.58	2.29	200	2.19	2.30	1.09	5.47	20.0%	11.3%			
1	2014070403	2.03	22.5%	0.09	2.12	200			1.10						
1	2014070203	1.48	23.0%	0.46	1.94	200	2.12	2.33	1.14	5.62			3.28	64.7%	5.07
1	2014070401	2.40	17.4%	0.85	3.25	200			1.06						
1	2014070208	2.15	17.0%	0.86	3.01	200	2.44	2.39	1.08	6.27					
1	2014061303	2.69	17.3%	-0.13	2.56	200			1.20						
2	2014082202	2.91	19.7%	0.57	3.48	150	2.10	2.36	0.83	4.11	20.6%	-4.7%			
2	2014082219	2.19	18.9%	0.82	3.01	150	2.70	2.15	1.01	5.87	18.1%	4.0%			8.13
2	2014082205	2.17	27.7%	0.56	2.73	150	1.61	3.65	1.03	6.05	18.4%	33.5%			
2	2014082207	2.30	24.0%	0.82	3.12	150	1.88	3.46	1.01	6.58	16.9%	29.6%			
2	2014082204	2.56	1.0%	0.82	3.38	150	2.11	3.95	0.86	7.13	11.9%	-1128.2%			
2	2014082702	1.70	1.0%	0.76	2.46	150	4.51	3.80	1.23	21.11	6.2%	-538.6%			
2	2014082218	2.02	19.7%	0.69	2.71	150	2.15	2.16	1.04	4.84	23.1%	-17.0%			8.27
2	2014060602	2.25	17.6%	0.43	2.68	150	2.72	2.51	1.30	8.88	14.9%	15.1%			
2	2014060405	2.56	19.5%	0.00	2.56	150	2.45	2.48	1.31	7.96	18.9%	3.2%			11.97
2	2014060408	2.27	18.3%	-0.28	1.99	150	2.55	2.40	1.24	7.60	17.6%	3.9%			
2	2014070209	1.83	17.9%	1.14	2.97	150	2.48	2.14	0.99	5.24	20.5%	-14.9%			
3	2014081501	2.48	30.5%	1.64	4.12	150	2.27	1.89	1.02	4.39	24.0%	21.4%	3.78	47.8%	7.9
3	2014081502	1.96	36.3%	0.64	2.6	150	1.68	1.75	1.08	3.18	36.5%	-0.4%	2.68	50.8%	5.28
3	2014081503	2.18	27.6%	0.86	3.04	150	2.47	1.44	1.10	3.91	29.6%	-7.4%			
3	2014081504	1.98	35.2%	1.07	3.05	150	2.15	1.75	1.10	4.14	27.5%	21.8%	3.36	52.4%	6.41
3	2014081507	2.01	27.3%	1.31	3.32	150			1.02						
3	2014081508	2.17	24.4%	1.68	3.85	150			0.95						
3	2014081509	1.85	28.0%	0.91	2.76	150			1.07				2.72	49.6%	5.48
3	2014081511	2.01	26.4%	0.94	2.95	150			1.08						
3	2014081512	2.14	1.0%	3.66	5.8	150			0.99						
3	2014082203	2.50	1.0%	2.53	5.03	150	4.41	4.85	0.86	18.31	4.7%	-380.5%			
3	2014082206	2.28	24.4%	1.37	3.65	150	1.76	3.19	1.04	5.86	18.7%	23.3%			
3	2014082208B		15.5%			150	2.06	1.68			16.1%	-3.9%			
3	2014082210	2.03	18.3%	1.22	3.25	150			1.01						
3	2014082212	2.04	19.8%	1.32	3.36	150			0.93						
3	2014082701	1.74		1.28	3.02	150			1.14						

Figure B.1: Full list of devices used in this thesis, first through third batches.

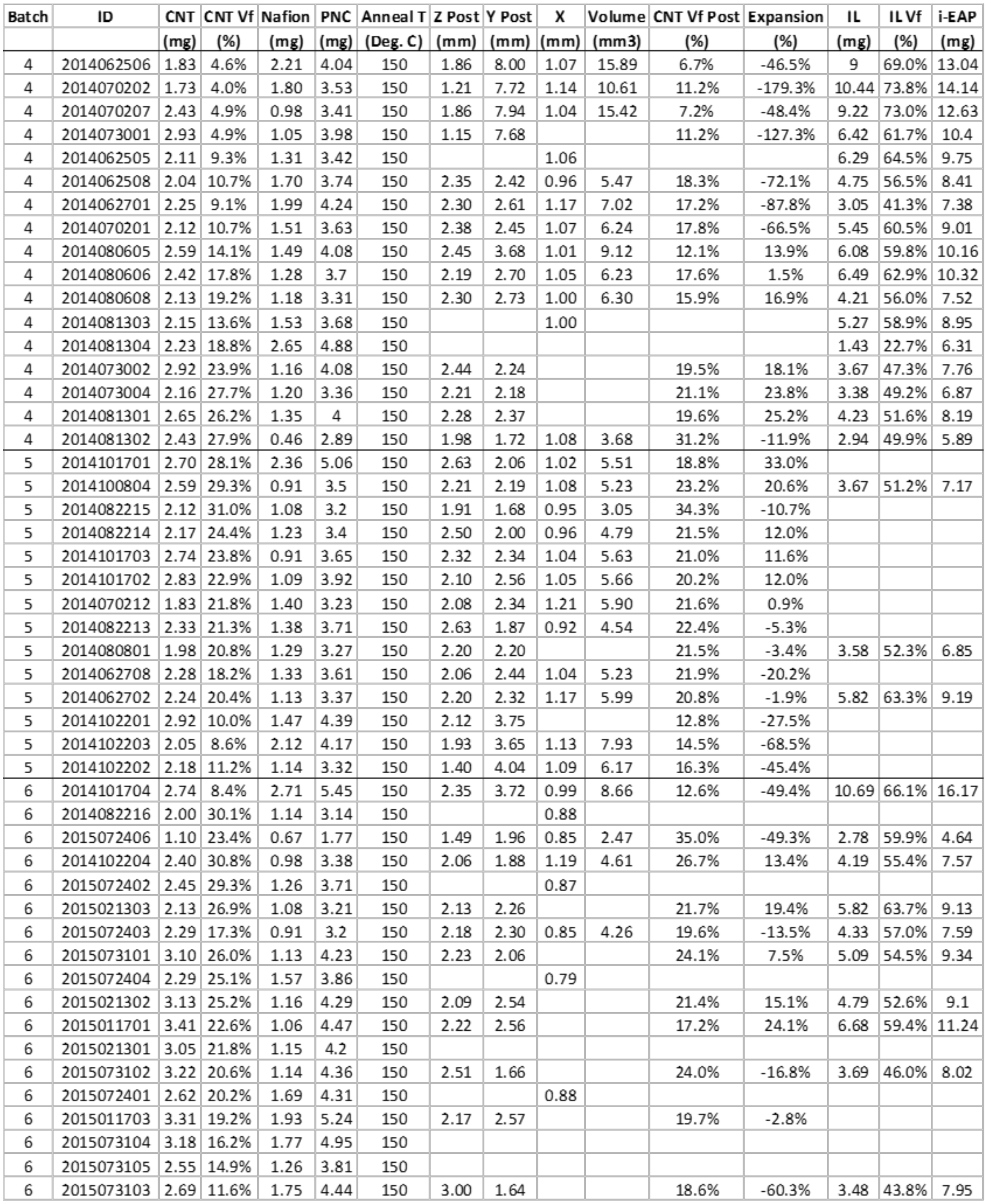

Batch	ID	CNT	CNT Vf	Nafion	PNC	Anneal T	Z Post	Y Post	X	Volume	CNT Vf Post	Expansion	IL	IL Vf	i-EAP
		(mg)	(%)	(mg)	(mg)	(Deg. C)	(mm)	(mm)	(mm)	(mm3)	(%)	(%)	(mg)	(%)	(mg)
4	2014062506	1.83	4.6%	2.21	4.04	150	1.86	8.00	1.07	15.89	6.7%	-46.5%	9	69.0%	13.04
4	2014070202	1.73	4.0%	1.80	3.53	150	1.21	7.72	1.14	10.61	11.2%	-179.3%	10.44	73.8%	14.14
4	2014070207	2.43	4.9%	0.98	3.41	150	1.86	7.94	1.04	15.42	7.2%	-48.4%	9.22	73.0%	12.63
4	2014073001	2.93	4.9%	1.05	3.98	150	1.15	7.68			11.2%	-127.3%	6.42	61.7%	10.4
4	2014062505	2.11	9.3%	1.31	3.42	150			1.06				6.29	64.5%	9.75
4	2014062508	2.04	10.7%	1.70	3.74	150	2.35	2.42	0.96	5.47	18.3%	-72.1%	4.75	56.5%	8.41
4	2014062701	2.25	9.1%	1.99	4.24	150	2.30	2.61	1.17	7.02	17.2%	-87.8%	3.05	41.3%	7.38
4	2014070201	2.12	10.7%	1.51	3.63	150	2.38	2.45	1.07	6.24	17.8%	-66.5%	5.45	60.5%	9.01
4	2014080605	2.59	14.1%	1.49	4.08	150	2.45	3.68	1.01	9.12	12.1%	13.9%	6.08	59.8%	10.16
4	2014080606	2.42	17.8%	1.28	3.7	150	2.19	2.70	1.05	6.23	17.6%	1.5%	6.49	62.9%	10.32
4	2014080608	2.13	19.2%	1.18	3.31	150	2.30	2.73	1.00	6.30	15.9%	16.9%	4.21	56.0%	7.52
4	2014081303	2.15	13.6%	1.53	3.68	150			1.00				5.27	58.9%	8.95
4	2014081304	2.23	18.8%	2.65	4.88	150							1.43	22.7%	6.31
4	2014073002	2.92	23.9%	1.16	4.08	150	2.44	2.24			19.5%	18.1%	3.67	47.3%	7.76
4	2014073004	2.16	27.7%	1.20	3.36	150	2.21	2.18			21.1%	23.8%	3.38	49.2%	6.87
4	2014081301	2.65	26.2%	1.35	4	150	2.28	2.37			19.6%	25.2%	4.23	51.6%	8.19
4	2014081302	2.43	27.9%	0.46	2.89	150	1.98	1.72	1.08	3.68	31.2%	-11.9%	2.94	49.9%	5.89
5	2014101701	2.70	28.1%	2.36	5.06	150	2.63	2.06	1.02	5.51	18.8%	33.0%			
5	2014100804	2.59	29.3%	0.91	3.5	150	2.21	2.19	1.08	5.23	23.2%	20.6%	3.67	51.2%	7.17
5	2014082215	2.12	31.0%	1.08	3.2	150	1.91	1.68	0.95	3.05	34.3%	-10.7%			
5	2014082214	2.17	24.4%	1.23	3.4	150	2.50	2.00	0.96	4.79	21.5%	12.0%			
5	2014101703	2.74	23.8%	0.91	3.65	150	2.32	2.34	1.04	5.63	21.0%	11.6%			
5	2014101702	2.83	22.9%	1.09	3.92	150	2.10	2.56	1.05	5.66	20.2%	12.0%			
5	2014070212	1.83	21.8%	1.40	3.23	150	2.08	2.34	1.21	5.90	21.6%	0.9%			
5	2014082213	2.33	21.3%	1.38	3.71	150	2.63	1.87	0.92	4.54	22.4%	-5.3%			
5	2014080801	1.98	20.8%	1.29	3.27	150	2.20	2.20			21.5%	-3.4%	3.58	52.3%	6.85
5	2014062708	2.28	18.2%	1.33	3.61	150	2.06	2.44	1.04	5.23	21.9%	-20.2%			
5	2014062702	2.24	20.4%	1.13	3.37	150	2.20	2.32	1.17	5.99	20.8%	-1.9%	5.82	63.3%	9.19
5	2014102201	2.92	10.0%	1.47	4.39	150	2.12	3.75			12.8%	-27.5%			
5	2014102203	2.05	8.6%	2.12	4.17	150	1.93	3.65	1.13	7.93	14.5%	-68.5%			
5	2014102202	2.18	11.2%	1.14	3.32	150	1.40	4.04	1.09	6.17	16.3%	-45.4%			
6	2014101704	2.74	8.4%	2.71	5.45	150	2.35	3.72	0.99	8.66	12.6%	-49.4%	10.69	66.1%	16.17
6	2014082216	2.00	30.1%	1.14	3.14	150			0.88						
6	2015072406	1.10	23.4%	0.67	1.77	150	1.49	1.96	0.85	2.47	35.0%	-49.3%	2.78	59.9%	4.64
6	2014102204	2.40	30.8%	0.98	3.38	150	2.06	1.88	1.19	4.61	26.7%	13.4%	4.19	55.4%	7.57
6	2015072402	2.45	29.3%	1.26	3.71	150			0.87						
6	2015021303	2.13	26.9%	1.08	3.21	150	2.13	2.26			21.7%	19.4%	5.82	63.7%	9.13
6	2015072403	2.29	17.3%	0.91	3.2	150	2.18	2.30	0.85	4.26	19.6%	-13.5%	4.33	57.0%	7.59
6	2015073101	3.10	26.0%	1.13	4.23	150	2.23	2.06			24.1%	7.5%	5.09	54.5%	9.34
6	2015072404	2.29	25.1%	1.57	3.86	150			0.79						
6	2015021302	3.13	25.2%	1.16	4.29	150	2.09	2.54			21.4%	15.1%	4.79	52.6%	9.1
6	2015011701	3.41	22.6%	1.06	4.47	150	2.22	2.56			17.2%	24.1%	6.68	59.4%	11.24
6	2015021301	3.05	21.8%	1.15	4.2	150									
6	2015073102	3.22	20.6%	1.14	4.36	150	2.51	1.66			24.0%	-16.8%	3.69	46.0%	8.02
6	2015072401	2.62	20.2%	1.69	4.31	150			0.88						
6	2015011703	3.31	19.2%	1.93	5.24	150	2.17	2.57			19.7%	-2.8%			
6	2015073104	3.18	16.2%	1.77	4.95	150									
6	2015073105	2.55	14.9%	1.26	3.81	150									
6	2015073103	2.69	11.6%	1.75	4.44	150	3.00	1.64			18.6%	-60.3%	3.48	43.8%	7.95

Figure B.2: Full list of devices used in this thesis, fourth through sixth batches.

References

[1] M. Ghaffari, *et al.*, *Advanced Materials* **25**, 6277 (2013).

[2] Y. Bar-Cohen, X. Bao, S. Sherrit, S.-S. Lih, *Proceedings SPIE* **4695**, 286 (2002).

[3] Y. Liu, Ionic electroactive polymer composite actuators, Ph.D. thesis, The Pennsylvania State University (2012).

[4] K. J. Kim, M. Shahinpoor, *Polymer* **43**, 797 (2002). Mattice Special Issue.

[5] B. J. Akle, M. D. Bennett, D. J. Leo, *Sensors and Actuators A: Physical* **126**, 173 (2006).

[6] Y. Bar-Cohen, S. Sherrit, S.-S. Lih, *Proceedings SPIE* **4329**, 319 (2001).

[7] Y. Bar-Cohen, Q. Zhang, *MRS Bulletin* **33**, 173 (2008).

[8] B. Natarajan, *et al.*, *ACS nano* **9**, 6050 (2015).

[9] B. Akle, M. Bennett, D. Leo, K. Wiles, J. McGrath, *Journal of Materials Science* **42**, 7031 (2007).

[10] S. Liu, *et al.*, *Advanced Functional Materials* **20**, 3266 (2010).

[11] J. Michalenko, *NNIN REU Research Accomplishments* pp. 146–47 (2013).

[12] D. Handlin, *et al.*, *Journal of Applied Physics* **114**, 224310 (2013).

[13] L. Jiang, S. Spearing, M. Monclus, N. Jennett, *Composites Science and Technology* **71**, 1301 (2011).

[14] M. Mionić, *et al.*, *Physica Status Solidi B* **247**, 3072 (2010).

[15] C. Rong, *et al.*, *Composites Science and Technology* **70**, 380 (2010).

[16] H. Cebeci, R. Guzman de Villoria, A. J. Hart, B. L. Wardle, *Composites Science and Technology* **69**, 2649 (2009).

[17] B. L. Wardle, *et al.*, *Advanced Materials* **20**, 2707 (2008).

[18] P. M. Ajayan, J. M. Tour, *Nature* **447**, 1066 (2007).

[19] Y. Zhou, *et al.*, *Nano Energy* **9**, 176 (2014).

[20] B. Akle, D. Leo, M. Hickner, J. McGrath, *Journal of Materials Science* **40**, 3715 (2005).

[21] R. H. Baughman, *Science* **308**, 63 (2005).

[22] S. Nemat-Nasser, J. Y. Li, *Journal of Applied Physics* **87**, 3321 (2000).

[23] S. Sewa, K. Onishi, K. Asaka, N. Fujiwara, K. Oguro, *Micro Electro Mechanical Systems, 1998. MEMS 98. Proceedings., The Eleventh Annual International Workshop on* (1998), pp. 148–153.

[24] Environmental Robots Inc. (2015). Http://www.environmental-robots.com/products.html.

[25] Parker Hannifin Corp, Online (2015). Http://promo.parker.com/promotionsite/artificialmuscle/us/en/home.

[26] Y. Liu, *et al.*, *Scientific Reports* **3**, 973 (2013).

[27] S. Liu, *et al.*, *Polymer International* **59**, 321 (2010).

[28] T. E. Chin, U. Rhyner, Y. Koyama, S. R. Hall, Y.-M. Chiang, *Electrochemical and Solid-State Letters* **9**, A134 (2006).

[29] Y. Liu, *et al.*, *Macromolecules* **45**, 5128 (2012).

[30] S. Hara, T. Zama, W. Takashima, K. Kaneto, *Journal of Materials Chemistry* **14**, 1516 (2004).

[31] M. F. L. De Volder, S. H. Tawfick, R. H. Baughman, A. J. Hart, *Science* **339**, 535 (2013).

[32] M.-F. Yu, B. S. Files, S. Arepalli, R. S. Ruoff, *Physical Review Letters* **84**, 5552 (2000).

[33] A. J. Hart, A. H. Slocum, *The Journal of Physical Chemistry B* **110**, 8250 (2006).

[34] A. J. Hart, A. H. Slocum, *Nano Letters* **6**, 1254 (2006).

[35] I. Y. Stein, B. L. Wardle, *Physical Chemistry Chemical Physics* **15**, 4033 (2013).

[36] G. D. Nessim, *et al.*, *Nano Letters* **8**, 3587 (2008).

[37] K. Hata, *et al.*, *Science* **306**, 1362 (2004).

[38] G. D. Nessim, *et al.*, *Carbon* **50**, 4002 (2012).

[39] H. Cebeci, I. Y. Stein, B. L. Wardle, *Applied Physics Letters* **104**, 023117 (2014).

[40] I. Y. Stein, N. Lachman, M. E. Devoe, B. L. Wardle, *ACS Nano* **8**, 4591 (2014). PMID: 24684313.

[41] J. Lee, *et al.*, *Applied Physics Letters* **106**, 053110 (2015).

[42] P. D. Bradford, X. Wang, H. Zhao, Y. Zhu, *Carbon* **49**, 2834 (2011).

[43] A. T. Sepulveda, *et al.*, *Nanoscale* **5**, 4847 (2013).

[44] I. Y. Stein, D. J. Lewis, B. L. Wardle, *Nanoscale* **7**, 19426 (2015).

[45] I. Y. Stein, B. L. Wardle, *Nanotechnology* **27**, 035701 (2016).

[46] L. S. Schadler, S. C. Giannaris, P. M. Ajayan, *Applied Physics Letters* **73**, 3842 (1998).

[47] S. Vaddiraju, H. Cebeci, K. K. Gleason, B. L. Wardle, *ACS Applied Material Interfaces* **1**, 2565 (2009).

[48] M. Ghaffari, *et al.*, *Electrochimica Acta* **112**, 522 (2013).

[49] T. Wang, *et al.*, *Journal of Power Sources* **274**, 709 (2015).

[50] D. Y. Lee, I.-S. Park, M.-H. Lee, K. J. Kim, S. Heo, *Sensors and Actuators A: Physical* **133**, 117 (2007).

[51] J.-H. Jung, J.-H. Jeon, V. Sridhar, I.-K. Oh, *Carbon* **49**, 1279 (2011).

[52] C. Welsh, *et al.*, *Dielectrics and Electrical Insulation, IEEE Transactions on* **22**, 1389 (2015).

[53] www.fuelcellstore.com, Dupont nafion pfsa membranes nr-211 and nr-212, Data sheet.

[54] S. Liu, High electromechanical response electroactive polymers and their applications for solid state actuators, Ph.D. thesis, The Pennsylvania State University (2010).

[55] V. V. Chaban, O. V. Prezhdo, *The Journal of Physical Chemistry Letters* **2**, 2499 (2011).

[56] N. D. Khupse, A. Kumar, *Indian journal of chemistry. Section A, Inorganic, bio-inorganic, physical, theoretical & analytical chemistry* **49**, 635 (2010).

[57] L. E. Barrosse-Antle, *et al.*, *Chemistry An Asian Journal* **5**, 202 (2010).

[58] J. Wang, Y. Tian, Y. Zhao, K. Zhuo, *Green Chemistry* **5**, 618 (2003).

[59] M.-M. Huang, Y. Jiang, P. Sasisanker, G. W. Driver, H. Weingrtner, *Journal of Chemical & Engineering Data* **56**, 1494 (2011).

[60] K. Nasirzadeh, R. Neueder, W. Kunz, *Journal of Chemical & Engineering Data* **50**, 26 (2005).

[61] A. M. O'Mahony, D. S. Silvester, L. Aldous, C. Hardacre, R. G. Compton, *Journal of Chemical & Engineering Data* **53**, 2884 (2008).

[62] J. H. Lee, *et al.*, *Sensors and Actuators A: Physical* (2004).

[63] G. C. Xiaolong Cui, X. Han, *Journal of Chemical & Engineering Data* **51**, 1860 (2006).

[64] J. M. Bernal-Garcia, A. Guzman-Lopez, A. Cabrales-Torres, A. Estrada-Baltazar, G. A. Iglesias-Silva, *Journal of Chemical & Engineering Data* **53**, 1024 (2008).

[65] E. J. Garca, A. J. Hart, B. L. Wardle, A. H. Slocum, *Nanotechnology* **18**, 165602 (2007).

[66] D. A. Handlin, Three-dimensional constitutive relations of aligned carbon nanotube polymer nanocomposites, Master's thesis, Massachusetts Institute of Technology (2013).

[67] Vapor pressure of water, Website (2015). Http://intro.chem.okstate.edu/1515sp01/database/vpwater.html.

[68] K. R. Harris, M. Kanakubo, L. A. Woolf, *Journal of Chemical & Engineering Data* **52**, 2425 (2007).

[69] M. Bedewy, *et al.*, *The Journal of Physical Chemistry C* **113**, 20576 (2009).

[70] R. Mitchell III, Investigation of lithium-air battery discharge product formed on carbon nanotube and nanofiber electrodes, Ph.D. thesis, Massachusetts Institute of Technology (2013).

[71] K. A. Mauritz, R. B. Moore, *Chemical Reviews* **104**, 4535 (2004).

[72] P. Rae, D. Dattelbaum, *Polymer* **45**, 7615 (2004).

[73] O. Ruiz de Ballesteros, F. Auriemma, G. Guerra, P. Corradini, *Macromolecules* **29**, 7141 (1996).

[74] I. Y. Stein, B. L. Wardle, *Carbon* **68**, 807 (2014).

[75] ASTM D695-10, Standard test method for compressive properties of rigid plastics (2010). ASTM International, West Conshohocken, PA, 2015.

[76] J. W. Gooch, *Encyclopedic Dictionary of Polymers* (2011).

[77] DuPont, Teflon ptfe properties handbook. H-37051-3.

[78] IEEE, *ANSI/IEEE Std 176-1987* (1988). IEEE Standard on Piezoelectricity.

[79] J. F. Tressler, S. Alkoy, R. E. Newnham, *Journal of Electroceramics* **2**, 257 (1998).

[80] R. Guzman de Villoria, A. J. Hart, B. L. Wardle, *ACS Nano* **5**, 4850 (2011). PMID: 21591620.